SCUOLA DI DOTTORATO
UNIVERSITA' DEGLI STUDI DI MILANO – BICOCCA

Department of Materials Science
PhD Course in Science and Nanotechnology of Materials, XXX Cycle

Advanced Spectroscopy of Interface Engineered, Doped and "Electronically" Doped Colloidal Semiconductor Nanocrystals

Valerio Pinchetti

Matr. n. 760555

Tutor: Prof. S. Brovelli

Coordinator: Prof. M. Bernasconi

ACADEMIC YEAR 2016/2017

"The idea that are basic to [my work] often bear witness to my amazement and wonder at the laws of the nature which operate in the world around us.

He who wonders discovers that this in itself is wonder."

Marcus C. Escher, The Graphic Work (1978)

Summary

Introduction

Semiconductor colloidal nanocrystals are solution-processable materials that, since their discovery almost 30 years ago, have focused scientific and technological attention thanks to their tunable optical and electrical properties. Colloidal nanocrystals have indeed wide applicative perspectives that span from light-emitting diodes, to lasers, from solar cells to luminescent solar concentrators, from bioimaging to quantum information. Such a large range of potential nanocrystals technologies is warranted by the unique knowledge and control that has been achieved over the years about their electronic properties. Specifically, the optical and electric properties of these nanomaterials have been tuned not only by controlling their size, composition and shape, but also producing a plethora of heterostructures in which two or more semiconductors are grown on top of an initial nanocrystal "seed", or by introducing in the host semiconductor matrix few atoms of a different chemical element, i.e. doping the nanocrystals. Because of the vast gamut of possibilities that colloidal nanocrystals offer to the scientific community, many questions on the elusive charge carrier dynamics underlying the macroscopic experimental observations are still unanswered. In this picture, my work points toward three different sub-classes of nanocrystals: *i*) interface engineered core/shell nanocrystals; *ii*) doped nanocrystals and *iii*) 'electronic' doped nanocrystals.

After a review about the 'state of the art' of colloidal nanocrystal science (Chapter 1), in Chapter 2 I show a detailed investigation on the interaction between the photoexcited charge carriers and the engineered interface of Dot-in-Bulk core/shell nanocrystal, which are featured by radiative recombination from both the core and shell states. I demonstrate that their uncommon dual emission is due to the peculiar interface structure between the compositional domains and that a fine tuning of the optical properties can be also achieved by modifying the interfacial potential profile.

In Chapter 3, I propose a novel synthetic approach to overcome the intrinsic Poisson distribution characteristic of the up-to-date nanocrystal doping strategies that are based on stochastic distribution of impurity ions in the nanocrystal ensemble. To this aim, I use monodispersed metal cluster as seeds for the nanocrystal nucleation in the synthesis reaction flask. By mean of combined optical and elemental analysis, I show that the copper clusters composed of exactly four atoms are indeed embedded in the semiconductor matrix, giving monodispersed doped nanocrystals.

Semiconductor doping can be further distinguished in 'isovalent' doping, in which the impurity has the same oxidation state of the host compound, and 'electronic' doping given by ions which introduce a net charge in the surrounding matrix. The most known 'ordinary' dopant for II-VI semiconductors is Mn^{2+} because of its d^5 configuration which is featured by unique magnetic properties that, in quantum confined nanomaterials lead to the formation of magnetic *polarons*. In Chapter 4, I reveal how polaron formation affects the exciton energy by mean of resonant PL measurements, offering a precise estimation of the intensity of the internal magnetic field generated by the Mn^{2+} spins.

In Chapter 5, I report how the magnetic response typical of Mn^{2+} is reproduced by introducing silver, which is an electronic dopant for II-VI semiconductors, since it can only assume the +1 oxidation state. However, it introduces an electronic level in the forbidden energy gap of the host semiconductor that participates to the radiative recombination and therefore transiently switches to the paramagnetic +2 state. By mean of magnetic circular dichroism experiments I demonstrate that in nanocrystals doped with nonmagnetic silver dopants, the paramagnetic response is completely optically activated.

Finally, in Chapter 6 I focused the attention on a novel class of nanostructures that overcomes the environmental issues of II-VI semiconductor nanocrystal due to the presence of heavy-metals restricted by the law: ternary $CuInS_2$ colloidal nanocrystals. Despite some similarities with the well-known copper-doped II-VI semiconductors, the photophysical processes underlying their emission mechanism are still under debate. To address this gap, I carried out temperature-controlled photoluminescence and spectro-electrochemical experiments to unravel their intrinsic and extrinsic charge carrier dynamics.

Chapter 1
State of the Art

Colloidal semiconductor nanocrystals have been discovered more than 30 years ago and they are continuing to focus attention because of their peculiar and intriguing physics that arises from the strong quantum confinement of the electronic states and because of the wide range of potential technological applications that could be improved by their uniquely tunable electronic properties and their solution-based process capability. In these decades, control over the charge carrier dynamics in colloidal nanocrystals has been boosted beyond the traditional "size manipulation" concept through innovative strategies such as shaping, heterostructuring and doping. This advanced control of their flexible functionalities has opened the way to the first commercial nanocrystal-based technologies such as light-emitting devices and photovoltaics and holds promises in spintronics and bio-labeling. These applicative successes clearly reveal the persisting scientific enthusiasm that physicists, material scientists, chemists and engineers lavish on this research field. Despite the technological achievements, many fundamental aspects in the physical properties of colloidal nanocrystals are still debated. A deeper insight on the elusive physics underlying the promising properties of functionalized nanocrystals is therefore required to further extend the human control over the dynamics in nano-sized, quantum-confined material systems and, in turn, to promote their technological appeal. To this aim, in this thesis I focus on the correlation between the optical and magnetic properties of last-generation colloidal nanocrystals and their structural and compositional features by mean of optical techniques such as photoluminescence, fluorescence line narrowing and magnetic circular dichroism, addressing gaps that might implement their applicative perspectives.

Semiconductors are featured by a range of forbidden energies that divides a fully occupied valence band (VB) and a completely empty conduction band (CB). Excitation of a VB electron to the CB can be obtained by absorption of an electromagnetic wave with energy comparable to or higher than that of the semiconductor energy gap (E_g). Analogously, radiative relaxation of an excited electron to the VB results in emission of a photon with the energy equal to the E_g. Therefore, the optical properties of bulk semiconductors are directly tied to the width of the E_g which is determined by the chemical composition and crystal structure. Excited electrons, however, are not free to move in the direct space of the crystal, since they are coulombically attracted to the positively charged "*holes*" that the electrons themselves leave in the VB, to form the so-call "*exciton*" neutral quasiparticle.[12] Bulk excitons present similarities to the hydrogen atom (which is also composed of a positive and a negative charge), such as the presence of exciton states with analogous binding energies and a characteristic radius, the exciton Bohr radius (a_0), which is given by[13]

$$a_0 = \frac{4\pi\varepsilon_2\hbar^2}{e^2}\left(\frac{1}{m_e^*}+\frac{1}{m_h^*}\right) \quad (1.1)$$

where ε_2 is the background dielectric constant of the semiconductor, $\hbar$ is the reduced Planck's constant, e is the elementary charge and $m^*_{e,h}$ are the reduced mass of electron and hole, respectively. Typically, exciton Bohr radius of II-VI semiconductors (*i.e.* composed of either an alkaline earth metal -group 2- or a group 12 transition metal and a chalcogen -group 6) span from 2.2 nm (ZnS) to 7.5 nm (CdTe),[13] whereas in III-V semiconductors (that, analogously, are composed of a boron group and a nitrogen group element -group 3 and 5 of the periodic table, respectively) they range from 11 nm (InP) to 60 nm (InSb).[13] In semiconductor crystals featured by at least one dimension smaller than the respective Bohr radius, E_g is increased with respect to the bulk value and the additional contribution is dependent on the nano-size because of the tight confinement of electron and hole wave functions. This regime is dubbed as *quantum confinement regime* and it has first discovered almost 50 years ago in 2-dimensional MoS_2 nanocrystals (NCs)[14] and, 20 years later, 0-dimensional, solution-processed, colloidal semiconductor NCs were reported for the first time.[15,16] Because of their great technological perspectives corroborated by scientific advancements in both the synthesis of featured colloidal NCs and the knowledge of physical processes underlying their unique optical and magnetic properties, I focus my attention on yet unanswered questions concerning last-generation colloidal NCs.

1.1 - Electronic Structure of Quantum-Confined Nanocrystals

The electronic state structure of 0-dimensional NCs can be calculated, in the first approximation, using a spherical "quantum box" model in which the charge carriers wave functions are isotropically restricted by an infinite potential barrier. In this picture, the continuous energy bands of bulk semiconductors are replaced with the discrete electronic state structure which is characteristic of 0-dimensional nanostructures and is strongly dependent on the NC radius (R, Figure 1.1). The NC wave function is a product of an envelope and a Bloch wave function that describe the motion of the electrons in the NC spherical potential and in the oscillating potential due to the nuclear vibration, respectively. In principle, the Bloch wave function should comprise multiple wave functions of several bulk semiconductor bands. However, the interaction between different bands are often negligible and, therefore, the so-called "*single-band approximation*" can be assumed. As a consequence, the envelope wave function of the spherical box is the product of the spherical Bessel (j_L) and harmonic ($Y_{L,M}$) functions:

$$\Phi_{n,L,M}(r,\theta,\varphi) = \frac{\sqrt{2}}{R^3}\frac{j_L\left(\phi_{n,L},\frac{r}{R}\right)}{j_{L+1}\left(\phi_{n,L}\right)}Y_{L,M}(\theta,\varphi) \quad (1.2)$$

where r, θ and φ are the set of 3-dimensional polar coordinates and $\phi_{n,L}$ is the n-th root of the L-th order spherical Bessel function. Furthermore, n, L and M represent the quantum numbers of the corresponding quantum mechanical problem. However, the energies are degenerate with regard to M and therefore it is usually not reported in the notation of the quantized states. Contrarily, the principal quantum number n is usually denoted by progressive numbers at

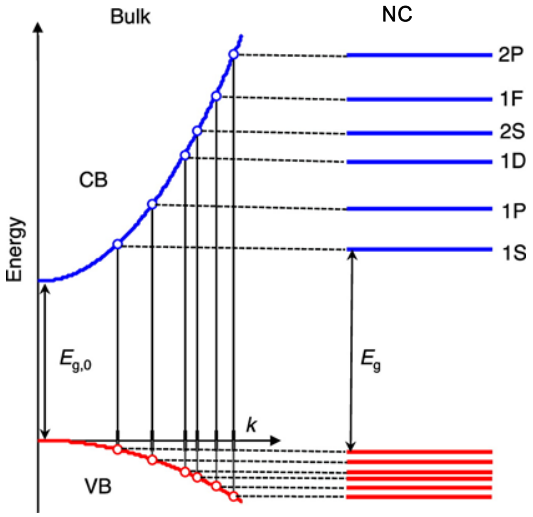

Figure 1.1 Idealized model of electronic states in a bulk semiconductor (left) and a spherical NC made of the same material (right). Continuous bands of a bulk semiconductor with parabolic dispersion of carrier kinetic energies ($E_k \propto k^2$; k is the wave vector) in the valence and conduction bands (denoted VB and CB, respectively) transform into discrete atomic-like levels in the case of the NC. The energies of the NC electronic states can be derived from those of the bulk semiconductor assuming discrete values of k. [Reprinted with permission from Ref. [277]. Copyright (2016) American Chemical Society.]

increasing energies and the orbital angular momentum quantum number L by capital letters (S, P and D for L = 1, 2 and 3, respectively). The corresponding energies of the electronic states are:

$$E_{n,L} = \frac{\hbar^2 \phi_{n,L}^2}{2m_e^* R^2} \tag{1.3}$$

Therefore, upon decreasing the radius of the spherical box, i.e. of the NC, the energy of the quantized states increases as the inverse of R^2. The exciton states energies are also effective-mass dependent, though. In II-VI semiconductors, the p-type character of the top of the valence band makes the effective mass of the excited holes usually consistently larger than the effective mass of the electrons in the s-type conduction band, leading to CB quantized states which are both sparser and less sensitive to the quantum confinement than the VB levels. Consequently, the larger NCs' E_g with respect to the bulk E_g mostly arises by shifting of the VB electronic states rather than CB levels and, for a non-interacting electron-hole couple, can be written as:

$$E_g^{NC} = E_g^{bulk} + \frac{\hbar^2 \phi_{n,L}^2}{2m_e^* R^2} + \frac{\hbar^2 \phi_{n,L}^2}{2m_h^* R^2} \tag{1.4}$$

The energy of interacting electron-hole couples (i.e. excitons) considers the Coulombic interaction that bounds the two charge carriers (V_{eh}) and is given by

$$V_{eh}(\boldsymbol{r}_e, \boldsymbol{r}_h) = -\frac{e^2}{\varepsilon_2 |\boldsymbol{r}_e - \boldsymbol{r}_h|} \tag{1.5}$$

where $\boldsymbol{r}_e$ and $\boldsymbol{r}_h$ are the electron and hole vector coordinates, respectively. The electrostatic interaction between the two charge carriers, however, is small with respect to the quantum confinement energies and, for NCs, can be therefore treated as a perturbation to the system. Applying the first-order perturbation theory to the electron and hole band-edge states ($1S_e$ and $1S_h$, respectively), I obtain

$$\Delta_{eh} = \left\langle \Phi_{1,0,0}(\boldsymbol{r}_e)\Phi_{1,0,0}(\boldsymbol{r}_h)\middle|V_{eh}(\boldsymbol{r}_e,\boldsymbol{r}_h)\middle|\Phi_{1,0,0}(\boldsymbol{r}_e)\Phi_{1,0,0}(\boldsymbol{r}_h)\right\rangle \tag{1.6}$$

where, from Eq. (1.2)

$$\Phi_{1,0,0}(r) = \frac{1}{\sqrt{2\pi R}}\frac{\sin(\pi r/R)}{r} \tag{1.7}$$

yielding to

$$\Delta_{eh} = -\frac{1.765e^2}{\varepsilon_2 r} \tag{1.8}$$

Finally, since $\phi_{1,0} = \pi$, and defining the exciton effective mass as $m^*_{exc} = m^*_e m^*_h/(m^*_e+m^*_h)$, the size-dependent NC E_g can be written as

$$E_g^{NC} = E_g^{bulk} + \frac{\hbar^2\pi^2}{2m^*_{exc}R^2} - \frac{1.765e^2}{\varepsilon_2 R} \tag{1.9}$$

The single-band approximation, however, provides a good description only of the *s*-type conduction band in II-VI semiconductors whereas the valence band typically shows a multi-sub-band character that makes not negligible the inter-band mixing due to the strong

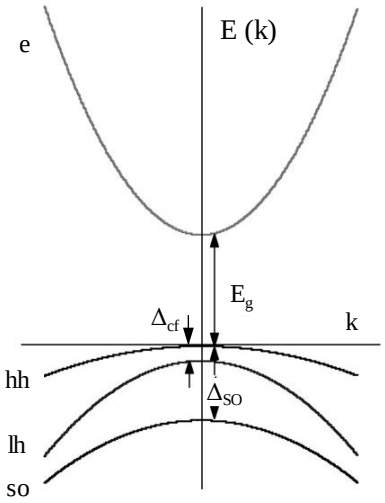

Figure 1.2 Band structure of wurtzite CdSe near the Γ point of the Brillouin zone. In contrast to the simple single-valence-band model considered in Figure 1.1, the valence band of CdSe comprises three subbands. Two correspond to the light (lh) and heavy (hh) hole bands split by energy Δ_{cf} due to a crystal field of a hexagonal lattice. The third, spin−orbit split-off band is separated from the heavy-hole band by Δ_{so} [Reprinted with permission from Ref. [277]. Copyright (2016) American Chemical Society.]

confinement regime, thus making the single-band approximation not applicable.[17-19] I will now focus on the description of CdSe NCs' VB electronic structure since they are the model system for both theoretical[9,18-34] and experimental studies[1,9,11,18-20,23,26-28,35-46] of II-VI quantum-confined colloidal nanostructures.

In CdSe, the top of the VB arises from Se 4*p* atomic orbitals and, therefore, it is formed by 6-fold degenerate wave functions split by spin-orbit interaction into a 4-fold degenerate band with Bloch-function angular momentum $J = 3/2$ and a 2-fold degenerate band featured by $J = 1/2$ (where J is the total angular momentum that sum the orbital, l, and spin, s, atomic contributions, Figure 1.2). The energy splitting of these two sub-bands is fairly large in CdSe ($\Delta_{SO} \sim 0.42$ eV),[47-49] leading to negligible band mixing. Therefore, I focus on mixing between the 4-fold states with $J = 3/2$, which consist of the heavy- and light-hole 2-fold spin-degenerate states, characterized by angular momentum projections $J_m = \pm 3/2$ and $J_m = \pm 1/2$, respectively (Figure 1.2). The crystal-field interaction further splits these two sub-bands at the Γ point of the Brillouin zone, which are therefore degenerate only in the case of cubic crystal structures (i.e. zincblende) whereas they are not for hexagonal lattices (i.e. wurtzite). However, since the crystal-field splitting is more than one order of magnitude smaller than the spin-orbit splitting ($\Delta_{cf} \sim 25$ meV for bulk wurtzite CdSe),[48,49] the quantum-confinement induced mixing should be considered.[17,18,50,51] In this case, the total angular momentum J is no more a good quantum number, which is thus replaced by the angular momentum F that sums the "unit cell" contribution (J) that arises from the underlying atomic structure and form the bulk bands and the envelope-function contribution (L) due to the spherical "quantum box" electronic state. In this picture, each NC hole state is a superposition of 2 envelope wave functions with orbital momenta L and L+2 and they are labeled with the L momentum and the projection of the angular momentum F as a subscript. In this notation, the three lowest excited hole states are $1S_{3/2}$, $1P_{3/2}$ and $2S_{3/2}$ (Figure 1.3). The crystal-field band mixing does not only alter the

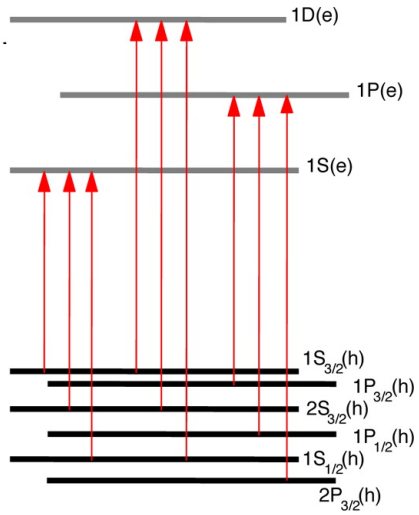

Figure 1.3 The multi-sub-band character of the valence band leads to a more complex structure of hole states in CdSe NCs compared to the single-band model, which translates into a more complex structure of interband optical transitions (shown by arrows). [Reprinted with permission from Ref. [277]. Copyright (2016) American Chemical Society.]

description and the nature of the hole states, but also modifies the selection rules for the optical transitions with the simple *s*-type CB states and the energy levels of the Coulombically bound excitons.

The lowest-energy exciton state is therefore formed by a 1S electron and a $1S_{3/2}$ hole (Figure 1.3), featured by 2 and 4 spin projections, respectively. The resulting exciton state has, hence, an 8-fold spin degeneracy that is lift by the crystal-field perturbation, by deviation from the exact spherical shape and the electron-hole exchange interaction that lead to the band-edge exciton fine structure. As discussed above, the crystal-field splits the hole states with different J_m and it is independent on R but only on the ratio of the light to heavy hole effective masses (m^*_{lh}/m^*_{hh}).[21,24] The NC non-sphericity can further separate the exciton states and, specifically, in oblate NC the light-heavy hole splitting is increased whilst in prolate NC it is reduced.[24] In small, prolate NCs the effect of the shape anisotropy can lead to the switching of the top of the VB from heavy-hole-like to light-hole-like state. Finally, the electron-hole exchange interaction, which is negligible in bulk, introduces an additional splitting in NCs because of their enhanced electron and hole wave functions overlap[52-54] and arises from the difference in the energy of excitons with different total spins, N. Therefore, it is useful to introduce the excitonic terminology: the spin-1/2 hole combined with the spin-1/2 electron can produce two excitonic states with the projection of the total angular momentum $N_m = 0$ (labelled as 0^L and 0^U where L and U stand for upper and lower, respectively) and one state with $N_m = 1$ (1^U). Differently, the spin-3/2 hole combined with the spin-1/2 electron generates one excitonic state with $|N_m| = 2$ (2^L and 2^U) and one with $|N_m| = 1$ (1^L). Each of these states with $|N_m| > 0$ is 2-fold spin-degenerate.

Including these effects into the spherical quantum box model as perturbations, it is possible to calculate the exciton fine structure[19] and, at a first sight, it may appear as a detailed theoretical investigation of the electronic levels without realistic experimental implications. Contrarily, the theoretical calculations played a crucial role in the understanding of the CdSe NCs' photophysics. Importantly, radiative exciton recombination in bulk II-VI semiconductors take place with ~1ns lifetime[55] whereas, despite the larger electron-hole wave functions overlap,

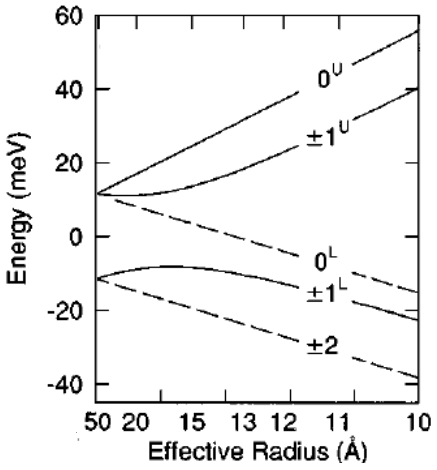

Figure 1.4 Size dependence of the exciton band-edge structure in spherical hexagonal CdSe NCs [Reprinted with permission from Ref. [24]. Copyright (1996) American Physical Society.]

CdSe NCs can show radiative decay lifetimes up to one order of magnitude longer at cryogenic temperatures.[20,23,56] As first proposed by Brumhead and coworkers,[52] the lowest-energy state of the exciton fine structure is featured by $|N_m| = 2$ and its recombination to the ground state is optically forbidden since a photon cannot carry an angular momentum higher than unity and it is therefore named "*dark*" exciton. On the contrary, the second excited exciton state is optically active, since it is the 1^L state and, analogously, it is dubbed "*bright*" exciton. Relaxation of the excited electron-hole pair into the lowest-energy non-emissive excited state thus explains the long photoluminescence (PL) decay times: the dark exciton must absorb a longitudinal-optical (LO) phonon to be promoted to the bright exciton state to radiatively recombine to the ground state. Since exciton-phonon interactions are less efficient, the radiative decay requires longer times to occur in quantum-confined NCs than in bulk. The energy separation between these two states defines the dark-bright exciton splitting (Δ_{db}). The fine structure can be experimentally detected by measuring the resonant Stokes shift with optical techniques such as size-selective fluorescence-line-narrowing (FLN) spectroscopy[19,57] or PL excitation (PLE).[58]

The previous discussion is based on the fundamental assumption that the whole set of NC's Cd and Se atoms are fully coordinated. However, the surface-to-volume ratio scales inversely with *R* and, hence, the role of the undercoordinated surface sites increases and eventually becomes dominant for nanometer-sized materials. These states always exist because of the incomplete passivation of the dangling bonds of surface ions by ligands.[59] In II-VI semiconductor NCs, the energy of these unsaturated surface states usually lies in the semiconductor forbidden energy gap (Figure 1.5, dashed lines) offering an alternative relaxation mechanism to the photoexcited charge carriers. Specifically, Galland *et al*. showed that the surface dangling bonds most likely capture hot electrons rather than band-edge electrons and the rate of this trapping process is higher than the ultrafast intraband relaxation rate.[60] Since the shrunk quantum confined wave functions spill out of the NC's volume providing a high carrier density at the NC's surface,[61] the interaction with these surface traps is the dominant and most effective process, leaving an unpaired carrier at the band edge and a "trapped" carrier at the surface (Figure 1.5). In 2017, Bayer and coworkers showed that, in CdS NCs, trapping initially happens with the hole localizing at the surface and then, during ~100 ns, hole detrapping and electron trapping invert the situation, which can finally last for hundreds of microseconds at room temperature (Figure 1.5).[62] Localization at the surface states therefore leaves unpaired carriers at the band-edge which cannot radiatively recombine with the carrier trapped at the dangling bond, resulting in a drastic quench of the PL efficiency. It is worth noting that, since trapping at the surface mostly affects hot electrons, the exciton PL decay lifetime is not affected.[60] This is in stark contrast with a further quenching mechanism that affect the PL efficiency in colloidal NCs: Auger recombination (AR).[63,64]

As mentioned before, surface trapping leaves unpaired charge carriers in the NC quantized states up to hundreds of microseconds. This long-living picture makes not negligible the chance to photogenerate an exciton in the presence of a "*resident carrier*", thus forming a quasi-particle composed of three charge carriers dubbed "*trion*".[65] This is an electrically charged quasi-particle and its sign is determined by the resident carrier: *negative* trions form are made of two electrons and one single hole whereas *positive* trions derive from a resident hole and are therefore composed of one electron and two holes.[62,66] The extra carrier triggers a process

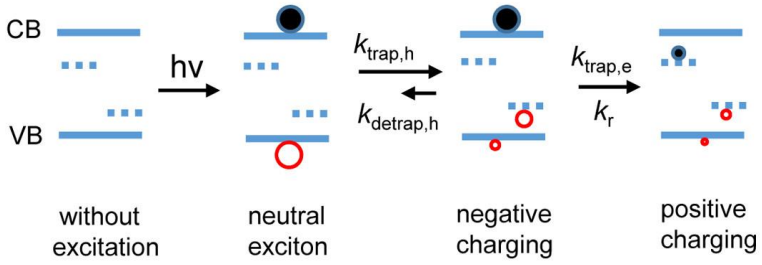

Figure 1.5 Scheme of the photocharging evolution from negative to positive after formation of a neutral exciton by absorption of a photon (hν). Dashed lines show surface electron (hole) trap states close to the conduction (valence) band, CB (VB). [Reprinted with permission from Ref. [62]. Copyright (2017) American Chemical Society.]

known as nonradiative Auger recombination during which the energy released by the annihilation of an electron-hole pair is acquired by the extra charging electron or hole. Because the rate of AR is orders of magnitude faster than the rate of radiative recombination,[67] PL is completely suppressed or quenched in charged NCs. The rate of AR, $k_A = 1/\tau_A$, can be calculated using Fermi's Golden Rule

$$k_A = \frac{1}{\tau_A} = \frac{2\pi}{\hbar}\int |M_{if}|^2 \, \delta(E_i - E_f) d\mathcal{R} \qquad (1.10)$$

Where M_{if} is the electronic transition matrix element of the interparticle Coulomb interaction, $E_{i(f)}$ is the initial (final) energy of the system and $\mathcal{R}$ is the complete set of variables quantifying the final state of the system. In Eq. 1.10, a major problem is to obtain an accurate estimation of M_{if}. After the Auger process, the extra carrier acquires a large momentum, $\hbar k_f$, as a result of the transfer of photoexcitation energy and the corresponding wave function becomes rapidly oscillating,[67] resulting in a matrix element that is much smaller than the average Coulomb interaction energy, $e^2/\kappa a$, where e is the electronic charge, κ, is the dielectric constant and a is the confinement size. Integration of a smooth ground state with the rapidly oscillating final state causes the relative diminution of M_{if}. By expanding the ground state in its special frequency components (Fourier expansion), the leading contribution to M_{if} is given by the frequency, k_F, that matches the large momentum of the extra carrier in the excited final state, i.e. $k_F \approx k_f$. In colloidal NCs, the large k_F is usually introduced by abrupt interfaces or surfaces. To test this idea quantitatively, Cragg and Efros calculated k_A for two holes plus one electron ("positive trion" picture)[31] described by a two-band Kane model where both the electron and the holes are confined by an identical 1D potential

$$U_e(x) = U_h(x) = U_0 \frac{x^\nu}{x^\nu + a^\nu} \qquad (1.11)$$

where $2a$ is the effective width of the confinement potential and U_0 is its height, whereas ν controls the smoothness, i.e. the higher is ν, the more the potential resembles a discontinuous step potential. Conversely, the lower extreme corresponds to the smoothest possible potential at ν=2, which has a parabolic shape at the band edges. In the case of strong confinement potential ($a_B >> a$), the confinement energies are larger than the Coulombic interaction energies and therefore, in a first approximation, the trion energy can be seen as a spectrum of

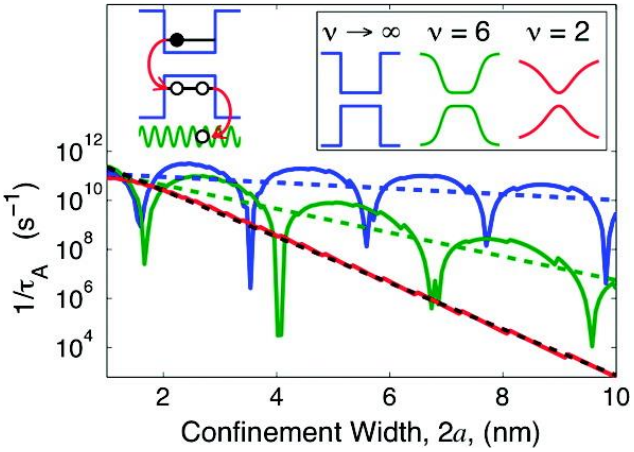

Figure 1.6 Semilog plot of the Auger recombination rate as a function of the confinement potential width, *2a*, for the case where the hole is ejected into the continuum (upper left). As shown in the inset, the three traces correspond to the confinement profiles given by Eq. (1.11) for ν→∞ (blue), 6 (green), and 2 (red), each with a fixed height of U_0 = 300 meV. Accompanying dashed lines are best fits to the dependencies in the least-squares sense. [Reprinted with permission from Ref. [31]. Copyright (2017) American Chemical Society.]

independent quantized particles where the Coulomb correlation can be calculated perturbatively. Therefore, the matrix element, M_{if}, responsible for Auger recombination in the confined, one-dimensional model is

$$M_{if} = \left\langle \Psi^i \middle| V(x_1 - x_2) \middle| \Psi^f \right\rangle \tag{1.12}$$

where $\Psi^{i(f)}$ is the initial (final) state wave function that, in the strongly confined regime, can be written as an antisymmetrized product of the single-hole wave functions, and $V(x_1\text{-}x_2)$ is the Coulomb repulsion between the two holes. It should also be noted that, depending on whether U_0 is smaller than or larger than the annihilation energy, the remnant hole in the final state will either reside in a continuum or in a discrete state. Considering first the case where AR leads to ejection of the hole from the confinement potential, energy conservation simplifies Eq. (1.10) to a product involving the density of final states, $\rho(E_f)$

$$k_A = \frac{1}{\tau_A} = \frac{2\pi}{\hbar} \left| M_{if} \right|^2 \rho(E_f) \tag{1.13}$$

showing that k_A is proportional to the square of the Fourier transform of the ground wave function. Suppression of k_A is therefore accomplished by softening the confining potential, causing an attenuation of the high frequency components in the ground state hole wave function. For example, an effective width of the confinement potential $2a$ = 5 nm with the potential profile described by Eq. (1.11) with ν = 2 is featured by a k_A that is 3 orders of magnitude lower than that for the abrupt step of $\nu\to\infty$ (Figure 1.6).

Furthermore, calculations showed orders-of-magnitude oscillations superimposed to the linear trend of k_A as a function of $2a$ (Figure 1.6) due to an intrinsic symmetry of the problem.[31] Since the Auger process does not change the initial symmetry of the multiparticle system, this symmetry must be maintained in the final state to obtain a non-vanishing matrix element.

Therefore, the k_A reaches a maximum when energy conservation allows the excited charge carrier to reach a quasi-resonant level of the continuum with matching symmetry. Conversely, the absence of such quasi-resonant states leads to destructive quantum mechanical interference of the electron or hole wave functions[67] and consequently to the deep minima shown in the k_A.

Analysis of k_A becomes more complicated if U_0 is larger than the recombination energy acquired by the hole during the AR. Because of the resulting discreteness of the hole energy spectrum, energy conservation cannot always be satisfied. Additionally, transitions to some of these levels are forbidden by the selection rules dictated by the confinement potential symmetry.[67] Hence, confinement potentials of certain sizes could have suppressed AR rates due to constraints imposed by these selection rules. However, complete suppression of Auger processes does not occur, as the remnant hole can access highly excited levels that are strongly broadened by fast decay and dephasing. Defining the total dephasing rate of the final hole state by Γ_f, Eq. (1.10) assumes the form

$$k_A = \frac{1}{\tau_A} = \frac{2\pi}{\hbar}\left|M_{if}\right|^2 \frac{1}{\Gamma_f} \tag{1.14}$$

where, similarly to the previous case, $|M_{if}|^2$ controls the dependence of k_A. However, although softening the confining potential profile suppresses $|M_{if}|^2$, the reduction in the AR rate is much less pronounced than it is when the extra carrier is ejected from the confinement potential.

Smoothening the confinement potential is therefore a powerful tool to lower the AR rate and to make it comparable or even lower than the respective radiative recombination rate. Hence, the latter becomes progressively more efficient and PL of charged excitons can be recorded. Since in negative (positive) trions, two electrons (holes) compete to recombine with one single hole (electron), the increase in the number of recombination pathways with respect to the neutral exciton leads to a higher radiative rate. The spectroscopic signature of charged excitons is therefore their higher emission intensity at short delays, together with a slightly higher emission energy with respect to the neutral excitons because of the Coulomb repulsion between the two carriers with the same charge.

Colloidal NCs are therefore affected by two different nonradiative recombination processes that compete with the exciton decay. This three-states picture has been demonstrated in 2011 by Galland *et al.* who observed the PL originating from a single NC while excited with a continuous wave laser.[60] The authors showed that the PL randomly flickers between three different states with different optical properties: the *exciton state*, which is featured by its decay rate (k_X) and intensity (I_X), a *dark state* which has the same decay rate of the exciton ($k_{dark} = k_X$) but strikingly lower emission intensity ($I_{dark} << I_X$), and, finally, a *grey state* with higher recombination rate ($k_{grey} >> k_X$) and lower intensity ($I_{grey} < I_X$). These states correspond to the photophysical processes described above: the exciton state is the highly efficient emission from the lowest, fine-structured excited state; the dark state is due to trapping of charge carriers at the surface dangling bonds; the grey state is observed when the NC is charged.[60]

The surface states therefore play a fundamental role in the photophysical properties of colloidal nanomaterials, offering a further parameter that can be used to improve and adjust their optical

properties. To this aim, the detrimental dangling bonds at the NC surface have been saturated both organically and inorganically, as described in the next Section.

1.2 – Colloidal Heterostructures

Preservation of single-component NCs' PL quantum yield (QY) strictly requires passivation of the intrinsic midgap states introduced by the unsaturated surface dangling bonds. This can be achieved by covalently bonding organic molecules (ligands) at the NC surface to both saturate the surface states and confer to the colloidal nanomaterial a hybrid nature. This strategy opens up the possibility of surface chemistry manipulation by replacement of ligands with application-targeted species such as targeting, therapy and sensing.[68-70] However, ligands are labile and can become either detached from the NC surface or damaged by exposure to light sources, resulting in uncontrolled changes in QYs and permanent photoinduced quenching of emission, known as photobleaching. Organic ligand dependencies of the optical properties can be overcome by coating the NC with an inorganic shell of a wider band-gap semiconductor to form core/shell NCs. Since the inorganic capping spatially decouples the electron and hole wave functions from the surface states and the chemical environment, these heterostructures are indeed generally brighter and more photostable compared to their organic-capped core-only counterparts. The optical properties of this class of nanostructures are therefore less sensitive to both the ligand-exchange reactions and the solution-processing into solid state. Moreover, inorganic heterostructuring further extend the ability to synthesize nanostructures with novel optoelectronic properties upon combining couples (or sets) of semiconductors with designed valence and conduction band alignment. Looking first at two-components core/shell heterostructures, the energy offsets between the electronic states of the adjoining materials can lead to different charge carrier localization regimes after photoexcitation that can be grouped in three limiting cases: type-I, type-II NCs and quasi-type-II (Figure 1.7). In the type-I regime, the band-gap of the core semiconductor lies entirely within the gap of the shell material, in a "nested" arrangement. As a result, both excited carriers are localized in the core resulting in a direct exciton with similar fine structure and optical properties to that described in Section 1.1. This band alignment is usually defined as "inorganic passivation" as the shell mostly serves as a barrier suppressing the interaction of the excited charge carriers with surface traps, effectively taking on the former role of the passivating organic ligands. Decoupling from the surface states of the excited charge carrier wave functions is not provided in "inverted" type-I arrangement, in which the core E_g is larger than the shell E_g. However, the chemical synthesis of inverted type-I NCs is easy to follow since the optical absorption and PL spectra strongly shift to lower energies as the shell forms and thickens and, for this reason, this geometry has been extensively studied in the early development of colloidal core/shell NCs.[71-75]

Combining two semiconductors featuring moderately wide band-gaps (~1.5 eV), the resulting heterostructured NCs are most likely characterized by a staggered band alignment in which both the conduction and valence band of one of the two materials lie at higher energy with respect to those of the other. This is the so-called type-II band structure and its most relevant consequence is that the electron and hole wave functions are pulled into separate material domains within the same NC, strongly reducing their overlap and, in turn, the oscillation strength of this spatially indirect transition (Figure 1.7b). The optical absorption will therefore

be still dominated by the semiconductor with narrower band-gap, whereas the radiative recombination results in an apparently Stokes shifted PL with longer PL decay lifetimes and lower QY, since slow nonradiative recombination processes can then compete with radiative decay.[76] It is worth noting that type-II heterostructures can be synthesized out of many of the materials pairs in either order, i.e. starting with a core of either semiconductor. However, there are often reasons for preferring one configuration over the other that can be dictated both by the ease of synthesis and the properties required by a given technological use (see, for example, CdS/ZnSe[77] *vs*. ZnSe/Cd[78]).

An intermediate picture between complete carrier co-localization (type-I) and separation (type-II) is the situation in which one carrier is localized in within a single compositional domain of the heterostructure and the other is delocalized across the whole material volume (quasi-type-II heterostructures, Figure 1.7c). This condition necessarily requires that the semiconductor pair has either the conduction or valence band energies similar, condition that is met only for a few NC sample compositions: CdSe/CdS,[79] PbSe/CdSe,[80] and InP/CdS.[81] Similarly to the type-I NCs, this class of heterostructures shows high emission QY but the absorption and emission spectral features progressively shift to lower energies during shell growth because of gradual delocalization of the charge carrier wave function with aligned core and shell band energies.[82]

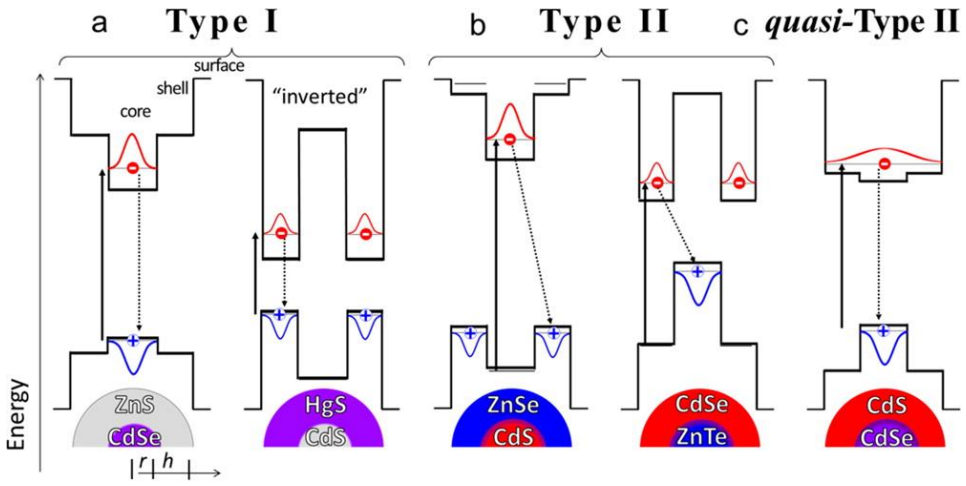

Figure 1.7 Band alignments between in core/shell NCs result in three major carrier localization regimes, depicted using the qualitative alignments for known examples of each (at bottom) based on the bulk band alignments (heavy horizontal lines) modified by quantum confinement (thin horizontal lines) for arbitrary combinations of core/shell size. The localizations of the wave function for band-edge electrons and holes are depicted in red and blue, respectively. The principal absorbing (solid arrows) and emitting (dotted arrows) transitions are also shown for each example. (a) Type-I NCs feature a nested alignment, causing both the electron and hole to reside principally in either the core (left) or the shell (right). (b) In Type-II NCs, a staggered alignment of conduction and valence bands pulls band-edge electrons and holes into separate parts of the core/shell QD. (c) In quasi-type-II NCs, one carrier remains localized in a single component of the heterostructure (here, the hole), while the other is largely delocalized throughout the entire QD. [Reprinted with permission from Ref. [244]. Copyright (2017) American Chemical Society.]

Finally, the core/shell paradigm has been further extended with the synthesis of core/multi-shell NCs, in which shells of various compositions and thicknesses are sequentially grown around a central core.[83-88] This "onion-like" structures can be produced with elaborated potential profiles such as direct[89,90] and inverted[91] quantum-dot-quantum-well colloidal NCs which show extremely high PL QYs and high stability *vs*. photo-oxidation, making them interesting for many application such as light emitting devices and bio-labeling. Most importantly, however, the quantum-dot-quantum-well NCs are of fundamental interest for understanding the charge carrier dynamics and their interactions across extremely thin semiconductor layers. Importantly, the multiple shells have been also used to overcome the problem of the lattice mismatch that affects many of the semiconductor couples used in binary core/shell systems. The strain induced by mismatching crystal lattices may lead to interface defects that, similarly to the surface states, act as traps for the photogenerated charge carriers, quenching the PL. Therefore, introduction of thin buffer layers of semiconductor with intermediate lattice constant greatly enhances the optical quality of the colloidal materials by removing the core/shell defects.

Among the large family of heterostructured colloidal NCs, CdSe/CdS NCs have been intensively experimentally investigated[92-102] and good theoretical description have been provided.[101-104] Therefore, they have been used as model system to investigate the role of further structural parameters that can be changed to tailor the optical properties of colloidal nanostructures. Specifically, CdSe/CdS 1-dimensional dot-in-rod[102,105-110] and rod-in-rod[111-114] structures, 2-dimensional dot-in-plate,[115] core/shell[116-119] and core/crown[119-122] nanoplatelets and 3-dimensional tetrapods[112,123-126] and octapods[127,128] have been synthesized. Therefore, in these quasi-type-II nanomaterials, as well as in 0-dimensional core/shell CdSe/CdS NCs, the interface between the two compositional domains introduces a potential barrier that strongly confines the photogenerated holes into the CdSe core. As mentioned for bare-core CdSe NCs, a sharp quantum-confinement potentials is a strict requirement for high AR rates[31,129] and, indeed, also the core/shell interface can boost the efficiency of the nonradiative AR. In 2013, Bae *et al.* reported a systematic work on AR in CdSe/CdS NCs with various confinement potential shapes[92] and they demonstrated that a progressive smoothening of the potential by intentionally introducing a $CdSe_{1-x}S_x$ alloy layer plays a significant role in the multi-exciton decay and, specifically, in the suppression of AR whereas it leaves unaltered the single exciton dynamics. This has been primarily ascribed to a reduced steepness of the hole core/shell confinement potential due to intermediate potential step introduced by the alloy layer. This work thus clearly demonstrates that the interface between compositional domains is an additional parameter to control the multi-exciton dynamics opening the way for the "*interface engineering*" of colloidal NCs. In this framework, Klimov and coworkers reported the so-called Dot-in-Bulk NCs (DiB-NCs),[130] that consist of a quantum confined CdSe core in zincblende structure overcoated by a thick, bulk-like CdS shell (thickness, *H*, is 8.5 nm, which is larger than CdS $a_0 \sim 3$ nm[131,132]). The peculiarity of these NCs is their unique polymorphic structure of the CdS shell, which is featured by a thin zincblende layer that covers the core and a bulky CdS volume in wurtzite structure.[130,133] Most importantly, DiB-NCs have been demonstrated to be the first colloidal nanostructures capable to emit from both the core and the shell states under low optical excitation[130] and electrical injection.[133] In DiB-NCs two types of excitons have been shown to co-exist: "*core excitons*", which are featured by a quantum confined hole and e

Coulombically bound electron, and "*shell excitons*", which have a bulk-like nature. This outstanding dual optical property has been ascribed to the peculiar shell lattice rearrangement that keeps the two compositional domains energetically separated. Since the zincblende CdS VB has a lower energy with respect to that of the wurtzite CdS,[2,4,5,8] it introduces a small potential barrier for localization of shell holes into the core (the large shell-to-core volume ratio -V_{shell}:V_{core} ~ 300:1- makes direct absorption at the CdSe core negligible), activating a Coulomb blockade mechanism for the core occupancy that, in turn, activates the shell PL. However, no detailed investigation has been provided to prove this hypothesis and the role of the shell polymorphism and this new type of engineered core/shell interface has not been explored. Hence, in Chapter, 2 I report a thorough investigation of the optical properties of both interface-engineered DiB-NCs and ordinary, sharp-interfaced NCs to shed light on the fundamental interaction between the thin zincblende layer and the exciton recombination dynamics. I'll show that radiative recombination from the shell states can be promoted by synthesizing colloidal NCs with a bulk-like CdS shell and a sharp core/shell interface, but the the peculiar interface structure of DiB-NCs is strictly required to activate the Coulomb blockade mechanism. Hence, AR is suppressed not via modification of the confinement potential profile but limiting the core occupancy to one exciton per time. Consequently, in CdSe/CdS NCs with ordinary interface, localization of shell excitons in the core is always a competing process to radiative recombination from the shell states, while the engineered interface makes the core "invisible" to the shell excitons when it is already occupied. This leads longer shell excitons lifetimes, that enables amplified spontaneous emission from the shell under nanosecond-long laser pulses. As a consequence, engineering the interface potential profile between compositional domains in colloidal NCs can be a promising strategy to further extend the control over the photophysical properties of colloidal nanostructures and their targeted synthesis for future technological applications.

1.3 – Doped Nanocrystals

At the nanoscale, confinement of the charge carrier wave functions leads to variations in the electronic state density, in lattice surface and strain distortions, in the charge distribution that evolve with NCs' size and affect their structural stability and chemical reactivity. As discussed in Sections 1.1 and 1.2, unprecedented physical properties have been achieved via control of size, composition, shape and compositional-domains interface. A further option to tune the properties of colloidal NCs is offered by the introduction of a small number of atoms of different elements in the semiconductor matrix. To date, the three prevalent synthesis strategies of colloidal doped NCs, which are called nucleation doping, growth doping and cation exchange reaction, mostly differ by the stage of the reaction at which the precursors of the impurity ions are added, i.e. at the beginning of the synthesis, while the NCs synthesis is proceeding and after the NCs have been produced, respectively. Outstanding improvements in these synthesis routes and the knowledge of cation exchange reactions allow to produce samples with almost atomic precision of the number of impurity ions.[134] Despite such advancements over the control of the doping level, the mentioned synthetic approaches are featured by an intrinsic drawback originating from the stochastic interaction of the doping ions with the NCs at the ensemble level, leading to a Poisson distribution of dopants across the NC population. Since the optical properties can be drastically changed by addition or removal of a few impurities, such as in the

case of silver-doped CdSe NCs, which have been reported to switch from *n*- to *p*-type doped NCs upon increasing the concentration of Ag atoms,[135] a non-uniform doping level in the ensemble can lead to misleading and complex results. To this aim, in Chapter 3, I focus on a novel synthesis strategy that overcomes this limitation by using metal cluster as nucleation seeds of colloidal NCs. Metal clusters are unique in that they can be represented with definite formulas, resembling well-defined organic molecules, and are particularly stable only for certain cluster sizes (i.e. number of metal atoms) which are known as "*magic clusters*". Their marked solidity most likely arises from the intrinsic stability of the metal cores arising from closing of geometrical structures and/or electronic shells, in which the interactions with the organic ligands play a crucial role. Using monodisperse, magic-sized copper clusters composed of four atoms and combining the results of elemental analyses and optical experiments, I demonstrate that indeed each NCs embeds four copper ions, i.e. one single cluster.

One of the major purposes of doping semiconductors since the beginning of the studies of doping bulk materials is the combination of magnetic and semiconductor properties in a single material. This was first realized in the late 1970s with the introduction of manganese ions into bulk CdTe,[136,137] constituting the class of multifunctional materials called diluted magnetic semiconductors (DMSs).[138] Namely, DMSs are alloys made up of a semiconductor whose lattice is made in part up of substitutional isovalent magnetic atoms. The most thoroughly investigated DMS materials are $A^{II}_{1-x}Mn_xB^{VI}$ alloys in which a fraction of group-II cations is randomly substituted by Mn ions. The $A^{II}_{1-x}Mn_xB^{VI}$ systems differ from the pure II-VI compounds in that the 3*d* shell of the Mn^{2+} ion is in d^5 configurations, meaning that it is only half-filled. This peculiar electronic structure leads to new intra-dopant electronic transition that dominates the optical properties of alloyed semiconductor. In its ground state, the manganese ion has five electrons in the five 3*d* orbitals, conferring to the dopant a total spin quantum number $S = 5/2$ and total angular momentum $L = 0$, since it is the sum of the five angular momenta $L = -2, -1, 0, +1$ and $+2$.[139] Considering the crystal-field perturbation introduced by the surrounding host matrix, this state is spherically symmetric and non-degenerate and it is labelled $^6A_1$. The lowest excited state of a Mn impurity thus requires flipping of one of the five aligned *d* electron spins, leading to a $S = 3/2$ configuration featured by $L \neq 0$. The crystal-field perturbation of both the zincblende and wurtzite lattice structures breaks the degeneracy of the five 3*d* states, making the $^4T_1$ configuration the lowest energy excited state.[139] Therefore, since the transition from the $^6A_1$ to the $^4T_1$ configurations correspond to flipping one manganese electron spin, its energy is mostly independent on the host matrix and it is approximately 2.2 eV. In bulk $A^{II}_{1-x}Mn_xB^{VI}$ systems, the optical absorption edge is determined by either the semiconductor E_g or the $^6A_1 \rightarrow {}^4T_1$ transition, depending on which is smaller. This aspect is of great relevance in colloidal semiconductor NCs, which are featured by a size-dependent E_g (Section 1.1), therefore allowing to include the manganese transition in the forbidden gap also for semiconductor with $E_{g,bulk} < 2.2$ eV. In this case, the Mn ions behave only as radiative recombination centres, hiding their peculiar magnetic properties, which rely on the boosted exchange interaction between the compressed *s*-like electron and *p*-like hole wave functions and the impurity 3*d* levels. This *sp-d* exchange interaction modifies the band structure of the host semiconductor NC and can be described by an additional Kondo-like term in the Hamiltonian, $\hat{H}$, of the material system

$$\widehat{H} = \widehat{H_0} + \sum_{R_i} J^{sp-d}(\boldsymbol{r} - \boldsymbol{R}_i)\boldsymbol{S}_i \cdot \boldsymbol{\sigma} \tag{1.15}$$

where $\hat{H}_0$ is the Hamiltonian of the bare semiconductor, $\boldsymbol{S}_i$ and $\boldsymbol{\sigma}$ are the spin operator for the Mn^{2+} and the band charge carrier, respectively, J^{sp-d} is the *sp-d* exchange coupling constant and $\boldsymbol{r}$ and $\boldsymbol{R}_i$ are the coordinates of the charge carrier and the dopant ion, respectively. Finally, the summation is over the NC impurities. From Eq. (1.15) can be clearly seen that the weight of the *sp-d* exchange interaction depends on the physical distance between the magnetic impurity and the band charge, which is strongly reduced in quantum confined systems. One major effect of enhanced *sp-d* exchange interaction is the non-linear dependence of the Zeeman splitting (ΔE_Z), since from Eq. (1.15) derives

$$\Delta E_Z(B,T) = g_{exc}\mu_B B + E_{sp-d}\mathcal{B}_{5/2}\left(\frac{5g_{Mn^{2+}}\mu_B B}{2k_B T}\right) \tag{1.16}$$

where the first term is the linear Zeeman splitting of undoped semiconductors featured by the intrinsic exciton g-factor, g_{exc}, whereas the second term accounts for the additional sub-linear splitting due to the interaction with the magnetic impurities, which depends on the Mn^{2+} g-factor. The factor E_{sp-d} of the second term is strongly sample-dependent, and it is due to the net overlap of the carrier envelope wave function and the magnetic impurity and thus indicates the saturation energy of the *sp-d* exchange interaction that is described by the Brillouin function

$$\mathcal{B}_J(x) = \frac{2J+1}{2J}\coth\left(\frac{2J+1}{2J}x\right) - \frac{1}{2J}\coth\left(\frac{1}{2J}x\right) \tag{1.17}$$

where J is, in general, a positive integer or half-integer, and, in this case, correspond to the Mn^{2+} total spin quantum number.

If the above manganese-induced effect occurs in the presence of external magnetic field and, hence, is easily experimentally accessible thanks to its magnetic-field dependence, introduction of magnetic impurities has also important consequences at zero magnetic field. Namely, quantum-confined excitons are characterized by a non-null spin (Section 1.1) that can interact through the *sp-d* exchange with the Mn^{2+} ions. This interaction leads to photoinduced alignment of the unpaired dopant spins and thus to a finite magnetization inside the single colloidal NC. As a result, the exciton perceives a finite concordant magnetization further lowering the energy of the exciton state, resulting in a bound state known as *exciton magnetic polaron* (EMP). Moreover, EMP only forms if the photoexcited charge carriers reside in the semiconductor bands and do not localize in the impurity centres. As mentioned above, this situation can be realized only hosts having a E_g narrower than the Mn-related transition, i.e. E_g < 2.2 eV. Experimental techniques commonly used to prove EMP formation in Mn-doped nanostructures mostly include continuous wave and time-resolved PL. In Chapter 4, I show the first investigation of magnetically-doped colloidal NCs by mean of *resonant* PL, which is found to be an especially powerful and incisive method for directly revealing EMP. In undoped NCs, tuning the optical excitation to the low-energy side of the 1S exciton absorption peak, resonantly excites band-edge excitons of the largest NCs, thus eliminating the intrinsic inhomogeneous broadening that affects non-resonant PL experiments of colloidal NCs. Therefore, the resonant PL spectra give direct experimental access to the longitudinal optical phonon structure of the

semiconductor matrix, since they are typically constituted of sharp peaks corresponding to thermalization of the photoexcited system to the lowest vibrational state. In Mn-doped CdSe NCs, the lowest excited state of the photogenerated exciton is the EMP, which is not featured by a vibrational fine structure. Contrarily, its energy is dictated by the strength of the *sp-d* interaction (Eq. (1.11)), and therefore it is strongly dependent on the position of the Mn^{2+} ions within each NC (Eq. (1.10)). Monte Carlo simulations well resembles the experimental results, confirming that the modification in the resonant PL spectra I report are due to formation of EMPs and that, hence, this technique is a useful tool for studies of collective magnetic phenomena in colloidal nanostructures.

The incorporation of Mn^{2+} dopants in II-VI semiconductors can be considered as "isovalent doping" where no additional charge is introduced by the impurity, which may ultimately either behave as radiative recombination centre or interact with the exciton spin to form EMPs. Contrarily, controlled doping with elements capable of affecting the electrical and optical properties of the host lattice by insertion of permanent charges into the NCs can be realized with ions featured by a different oxidation state with respect to the semiconductor. In this case, which is also known as "*electronic doping*", the impurities introduce atomic-like states within the forbidden gap that lie close to either the valence or conduction band (*p*- or *n*-type doping, respectively). Therefore, in bulk systems, the dopant-related extra charges can be thermally-activated from the shallow impurity states to the host bands, conferring conducting properties to otherwise poorly conducting materials. The free-carrier density in the semiconductor bands, N_{fc}, can be therefore suppressed at low temperatures, i.e. by freezing the charge carriers in their localized states, or tuning of the Fermi energy, E_F, via an electrochemical potential. Hence, electronic doping can be concisely described by the equation:

$$\frac{\partial N_{fc}}{\partial E_F} \neq 0 \qquad (1.18)$$

As shown in Section 1.1, quantum confinement easily distorts the position of the semiconductor bands, thus increasing the energy depth of the impurity states and lowering the probability to thermally excite extrinsic carriers to the host bands. The introduction of electronic dopants, however, is important not only for its consequences on the charge transport properties, but also because it broadens the range of optical and magnetic properties achievable beyond what is possible in pure materials. Generally, doping with transition metal or lanthanide ions provide large real Stokes shift between the absorption and emission spectra since, on one hand, the former takes place at the host semiconductor band-edge, analogously to undoped systems, whilst, on the other hand, the latter is a dopant-mediated process. Namely, one of the two photogenerated charge carriers localize from the semiconductor band to the impurity mid

gap state and then radiatively recombine: the optical Stokes shift can therefore reveal the depth of the optically active dopant state. In this picture, the electron-hole wave function overlap is strongly reduced, leading to the characteristic hundreds-of-nanoseconds long emission lifetime of radiative recombinations mediated by localized intragap states. Electronic doping of II-VI colloidal NCs has been most successfully achieved via insertion of copper *p*-type impurities in Cd^{2+} substitutional position. The amphoteric character of copper, which can be assume either the +1 and +2 oxidation states depending on the position of the Fermi level, makes this

transition metal interesting as a dopant for both its optical and magnetic properties. The Cu^+ state is optically passive, i.e. has a completely full *d* shell, but can be activated through capture of a hole from the semiconductor valence band, which then can participate in radiative transitions involving conduction band electrons. Contrarily, the Cu^{2+} state has an unpaired electron in its $3d^9$ shell and can be thus treated as a state with an intrinsic, permanent hole that can participate in emission without the injection of the photogenerated valence band hole. Most importantly, the latter state has non-zero orbital angular momentum (L = 2) and is strongly affected by crystal-field perturbations, Jahn-Teller effects and spin-orbit coupling, conferring to Cu-doped II-VI semiconductor NCs a DMS behavior. Moreover, upon capture of a photogenerated valence band hole, the subpopulation of nonmagnetic Cu^+ ions transiently switches to paramagnetic Cu^{2+}, leading to photoinduced boosted magnetization which is not possible with simple isovalent Mn^{2+} dopants. This brought into focus the idea that optically-switchable magnetism can be obtained in colloidal NCs doped with nominally nonmagnetic +1 impurities. Since silver has larger atomic radius than copper, despite belonging to the same group of the periodic table, they are featured by different electronic properties resulting in the almost complete absence of the +2 oxidation state. However, the optical and magnetic properties of silver-doped nanostructures have been much less investigated. To fill this gap, in Chapter 5 I report a thorough photophysical investigation of silver-doped CdSe NCs that combines optical spectroscopy, spectro-electrochemistry and magnetic circular dichroism experiments, leading to a comprehensive discussion of the carrier dynamics and the resulting photo-activated paramagnetic behavior. I demonstrate that the Ag^+ ions introduce an electronic level ~400 meV above the CdSe valence band which can be optically activated by ultrafast capture of a photogenerated valence band hole that then recombine with a conduction band electron. This excitonic recombination process is intrinsically tied to transient oxidation of silver dopants from Ag^+ to Ag^{2+} and has been indeed confirmed by mean of magnetic circular dichroism experiment. The DMS-like behavior of the magnetic response (Eq. (1.16)) also confirms that, in analogy to copper, the intragap state has a *d* character. I also prove that, in dark conditions, colloidal Ag-doped CdSe NCs are completely nonmagnetic, i.e. silver is embedded in the semiconductor matrix only as Ag^+. The absence of native Ag^{2+} ions thus makes silver-doped II-VI semiconductor NCs the first colloidal nanomaterial featured by paramagnetic properties totally activated by optical excitation, therefore opening new technological perspectives.

1.4 – Heavy-Metal-Free Ternary Nanocrystals

One major limitation to the introduction of II-VI semiconductor NCs in every-day technologies is dictated by toxicity concerns, since they mostly contain heavy-metals such as cadmium, lead and mercury. To minimize the risk, the growth of non-toxic ZnS or SiO_2 shells have been proposed to minimize the leakage of dangerous elements in the environment. However, the shell cannot eliminate the risk and therefore alternative NCs with less toxic compositions have been proposed such as Si, Ge, InP and $CuInS_2$ (CIS) NCs. These NCs share many advantages of conventional Cd-based NCs with respect to their optical properties, colloidal stability, PL stability and surface chemistry. The research community has begun to use these class of NCs for biological applications and evaluate their potential in numerous biophotonics applications such as medical diagnostics,[140] bioimaging,[141] biosensing,[142] laser tissue engineering[143] and

light activated therapy.[144] Specifically, CIS NCs have attracted major attention because of their optimal optical properties for other technological fields such as light-emitting devices,[145] solar cells sensitized with colloidal CIS NCs[146] and luminescent solar concentrators.[147] Despite copper might have toxic effects,[148] its use is not restricted by the law as cadmium[149], lead[150] and mercury[151] are, thus making CIS NCs a viable candidate to replace II-VI semiconductor NCs.

CIS is a direct band-gap semiconductor with a bulk band-gap of ~1.5 eV and Bohr radius of ~4.1 nm. In general, CIS NCs exhibit broad, featureless absorption spectra that contrast with the highly structured absorption spectra of II-VI semiconductor NCs. The PL spectra of CIS NCs are also broad (full width at half-maximum ~300-400 meV) and large Stokes shifts that range (~250-500 meV). Similarly to copper-doped II-VI semiconductor NCs, the broad PL emission and Large Stokes shift are retained throughout the quantum-confinement size regime. Since attempts to narrow the absorption and PL peaks of CIS NCs through size-selective methods have been unsuccessful, the origin of the broad optical features is most likely not due to inhomogeneities in size distribution. The energy of the PL peak in CIS NCs is also somewhat tunable with composition: for copper-deficient (sub-stoichiometric) CIS NCs, the absorption and PL both shift slightly to higher energy, retaining similar band-shapes, whereas for copper-rich CIS NCs, a red-shift is observed. However, it is unclear whether the NC size remain constant, so the observed shift may not be purely due to changes in composition.

Analogously to copper-doped NC systems, the oxidation state of the copper ions is still debated. Most synthetic procedures use Cu^{2+} precursors for copper doping and several groups have suggested that Cu^{2+} is reduced to Cu^{+} during NC synthesis, whereas electron paramagnetic resonance experiments and magnetic circular dichroism measurements points to the presence of unpaired spins characteristic of paramagnetic states such as Cu^{2+}. Both oxidation states can participate to radiative recombination of photogenerated excitons, but with different dynamics. Therefore, in Chapter 6 I report a detailed side-by-side investigation of both uncapped CIS NCs and core/shell CIS/ZnS NCs to provide an accurate description of the charge carrier dynamics in this novel class of ternary NCs. I combine temperature-controlled PL measurements and spectro-electrochemistry experiments and, through direct comparison of the two samples, I decoupled the intrinsic photophysics of CIS NCs from surface-related dynamics. Upon lowering the temperature, PL decay lifetimes of both samples show progressive lengthening, suggesting that CIS is intrinsically affected by temperature-activated nonradiative recombination pathway. However, the lower optical efficiency of bare-core CIS NCs with respect to core/shell CIS/ZnS NCs clearly reveals the presence of a surface-assisted, extrinsic recombination process that has been examined by tuning the Fermi level to gradually either suppress or assist it.

Chapter 2

Effect of Core/Shell Interface on Two-Color Emitting CdSe/CdS Nanocrystals

Two-color emitting colloidal semiconductor nanocrystals are of interest for applications in multimodal imaging, sensing, lighting, and integrated photonics. Dual color emission from core- and shell-related optical transitions has been recently obtained using so-called dot-in-bulk CdSe/CdS nanocrystals comprising a quantum-confined CdSe core embedded into an ultrathick (~7–9 nm) CdS shell. The physical mechanism underlying this behavior is still under debate. While a large shell volume appears to be a necessary condition for dual emission, comparison between various types of thick-shell CdSe/CdS nanocrystals indicates a critical role of the interface "sharpness" and the presence of potential barriers. To elucidate the effect of the interface morphology on the dual emission, I perform side-by-side studies of CdSe/CdS dot-in-bulk nanocrystals with nominally identical core and shell dimensions but different structural properties of the core/shell interface arising from the crystal structure of the starting CdSe cores (zincblende vs. wurtzite). While both structures exhibit dual emission under comparable pump intensities, nanocrystals with a zincblende core show a faster growth of shell luminescence with excitation fluence and a more readily realized regime of amplified spontaneous emission even under "slow" nanosecond excitation. These distinctions can be linked to the structure of the core/shell interface: nanocrystals grown from the zincblende cores contain a ~3.5 nm thick zincblende CdS interlayer, which separates the core from the wurtzite CdS shell and creates a potential barrier for photoexcited shell holes inhibiting their relaxation into the core. This helps maintain a higher population of shell states and simplifies the realization of dual emission and amplified spontaneous emission involving shell-based optical transitions.

Recently, the heterostructuring motif has been adopted by various groups to realize nanocrystals (NCs) capable of emitting multicolor light as a result of radiative recombination of excitons localized in different compositional domains, such as the core and the rod in elongated dot-in-rod structures, the core and the arms in tetrapods,[126,152-154] and the core and the shell regions in spherical core/shell systems.[91,155-160] This situation is realized in so-called dot-in-bulk (DiB) CdSe/CdS NCs, featuring a quantum confined CdSe core embedded into an ultra-thick (*ca*. 7−9 nm) CdS shell. The DiB-NCs are capable of emitting dual-color (red and green) light under both continuous wave optical[130] and electrical excitation.[133] In the original demonstration,[130] the development of dual-color emission in DiB-NCs was explained in terms of the polymorphic structure of the CdS shell comprising a ~3.5 nm thick zincblende (ZB) CdS layer grown epitaxially on top of the ZB CdSe core, followed by a much thicker, bulk-like layer of wurtzite (WZ) CdS. The ZB CdS layer at the core/shell interface introduces a ~30 meV potential barrier[5,8] between the valence-bands states of the ZB core and

the bulk-like WZ shell, which impedes relaxation of shell-localized holes into the core; otherwise it is an extremely fast sub-picosecond process.[107] Together with electrostatic repulsion between core and shell holes, the existence of the interfacial barrier leads to the development of a dynamic Coulomb blockade, which limits the core occupancy to approximately one hole per NC.[130] An important implication of this effect is the considerable suppression of nonradiative Auger recombination, which in thick-shell structures is dominated by a so-called positive-trion pathway, involving two strongly confined core-localized holes and a weakly confined electron.[25]

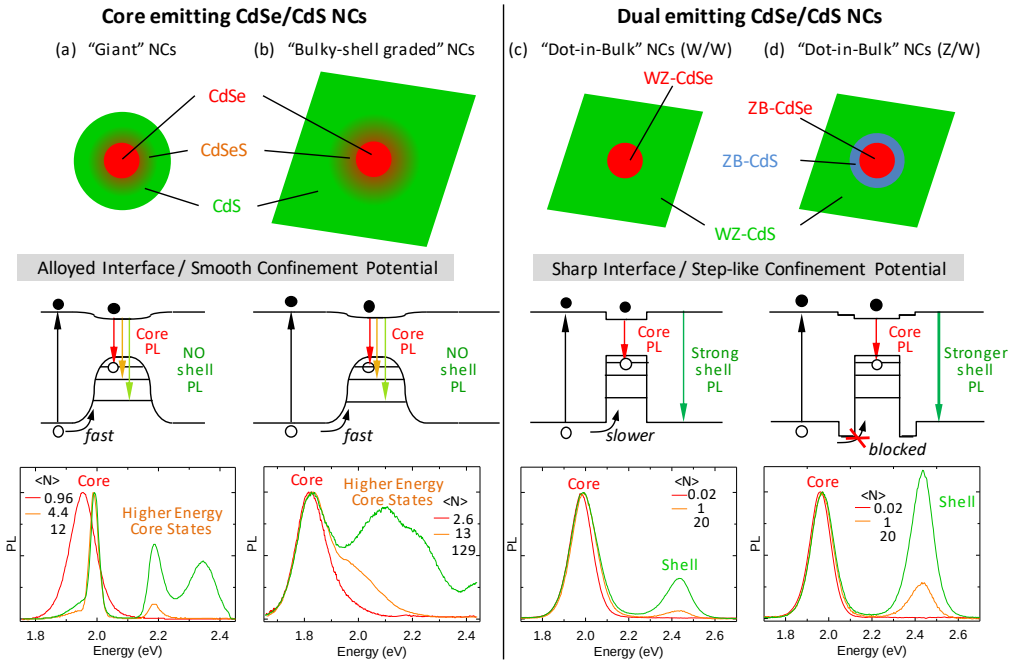

Figure 2.1 Various types of thick-shell CdSe/CdS NCs. (a) So-called "giant" NCs grown by SILAR (core radius R = 1.5 nm, shell thickness H = 5 nm). (b) Bulky shell graded NCs (R = 1.6 nm, H = 18 nm). (c) DiB-NCs comprising a WZ CdSe core (R = 1.5 nm) overcoated with a homogeneous WZ-CdS shell (H = 8.5 nm). (d) DiB-NCs comprising a ZB CdSe core (R = 1.5 nm) overcoated with a polymorphic shell featuring a ZB CdS layer (H_{ZB} = 3.5 nm) followed by a thick outer shell of WZ-CdS (H_{WZ} = 5 nm). Top row is a schematic depiction of various NCs; the alloyed $CdSe_xS_{1-x}$ interface existing in giant NCs and bulky-shell graded NCs is shown by a shaded area. The middle row shows their approximate band diagrams. The two structures at left have a graded composition of the interface, which leads to a smooth potential profile. The two structures at right are characterized by a sharp core/shell interface, which results in the abrupt, step-like potential profile. The lower row shows a series of normalized photoluminescence (PL) spectra for increasing pump fluences (indicated in terms of the average NC occupancy, ⟨N⟩). At the lowest excitation fluences, all structures show PL only due to core-based band-edge states. At higher fluences, CdSe/CdS NCs with alloyed interfaces exhibit emission from higher-energy core states (adapted from Refs. [164] and [99]), while DiB-NCs under similar excitation conditions show shell-based PL, which coexists with emission from the core.

As discussed in ref. [161], DiB-NCs support two types of excitons. One can be described in terms of a donor-like state in which the electron orbits within the Coulomb potential of the core-localized hole. This state is referred here to as the "*core exciton*". The electron–hole pairs introduced into the NC can also form "*shell excitons*". Since the overall size of these NCs is considerably larger than in the diameter of the Bohr exciton in CdS (~6 nm), shell-based excitons are Coulombically bound states that have a bulk-like character. Due to their charge neutrality, these excitons only weakly interact with each other but can readily sample surface defects that are often charged. As a result, shell excitons are sensitive to both the properties of the NC interface and the environment outside the NC, while the core excitons, that are isolated from the outer surface of the NC, are not. This property was explored in ratiometric sensing where the core emission acted as the internal reference for the surface sensitive shell luminescence.[161-163]

Despite various indications that the ability of DiB-NCs to emit two-color light is linked to some core-blocking mechanism, its exact nature and its connection to the internal structure of the CdS shell are still debated. Specifically, while the large shell volume seems to be a necessary condition for dual emission, taken alone it cannot explain highly efficient radiative recombination of shell-localized excitons. In fact, dual emission is observed neither in thick-shell CdSe/CdS NCs (so-called "*giant NCs*" or "*g-NCs*") grown by successive ionic layer adsorption and reaction (SILAR) method (Figure 2.1a)[164] nor in recently reported bulky-shell graded CdSe/CdS NCs[99] with shell volume over seven times larger than in DiB-NCs (shell thickness up to ~18 nm, Figure 2.1b). Even at extremely high NC occupancies, g-NCs and bulky-shell graded NCs do not exhibit shell luminescence, but instead show emission peaks arising from various higher-energy core-localized states that become progressively filled with increasing pump level (Figure 2.1a,b). This behavior is consistent with significant interfacial alloying occurring in both systems during the shelling reaction[94,99] that smoothens the potential profile at the core/shell interface and thus facilitates trapping of multiple holes into the core. The fact that DiB-NCs show efficient shell-based luminescence even at very low excitation

Shifts of CB and VB levels in quantum-confined CdSe NCs with respect to the band-edges of bulk CdSe

Cryst. Phase	R [nm]	ΔE_{CB} [eV]	ΔE_{VB} [eV]	Method	Ref.
WZ	1.5	0.65	--	XAS	Lee *et al.* [1]
WZ	1.4	0.50	-0.25	CV	Markus *et al.* [6]
WZ	1.4	0.55	0	PES	Markus *et al.* [6]
ZB	1.5	0.5	--	TB Theory	Lippens *et al.* [9]
ZB	1.5	0.7	-0.4	FPC Theory	Wang *et al.* [10]
ZB	1.5	0.65	--	XAS	Meulenberg *et al.* [11]
ZB	1.5	--	-0.25	CV	Meulenberg *et al.* [11]

Table 2.1 Confinement-induced shift of the conduction- (ΔE_{CB}) and valence-band (ΔE_{VB}) levels of CdSe NCs with radius R = 1.4-1.5 nm in either wurtzite (WZ) or zincblende (ZB) crystal phases with respect to the band-edges of bulk CdSe.

CB and VB energy offsets between the zincblende (ZB) and wurtzite (WZ) phases of CdS

Type of structure	$\Delta E_{CB,\,ZB/WZ}$ [meV]	$\Delta E_{VB,\,ZB/WZ}$ [meV]	Method	Ref.
Bulk	131	44	DF Theory	Li *et al.*[2]
Bulk	115	46	FPC Theory	Wei *et al.*[4]
Superlattice	70	30	PP Theory	Bandić *et al.*[5]
Bulk	73	31	LDA Theory	Murayama *et al.*[8]

Table 2.2 Conduction (ΔE_{CB}) and valence-band (ΔE_{VB}) energy offsets between the wurtzite (WZ) and zincblende (ZB) crystal phases of CdS.

fluence (average NC excitonic occupancy ⟨N⟩ of ~1) raises the question whether this behavior is a direct consequence of the structural barrier associated with the ZB-CdS interlayer or is a result of a "sharp" step-like interfacial potential profile which is characteristic of the DiB structures grown by a "fast-shelling" method which does not produce interfacial alloying.[165]

To elucidate the role of the exact interface morphology in the development of dual emission from CdSe/CdS NCs, I performed detailed side-by-side spectroscopic studies of two DiB-NC systems: one grown starting from the ZB CdSe cores and the other from the WZ CdSe cores. Both types of NCs have nominally identical core and shell dimensions but different morphologies of the core/shell interface. In the ZB-core-based structures, the ZB-CdS interlayer creates a potential barrier for shell localized holes, while this barrier is absent in the WZ-core-based NCs. Interestingly, while both DiB-NC systems exhibit shell luminescence at low pump fluences (Figure 2.1c,d), the dynamic Coulomb blockade is active only in the structures with the interfacial barrier. This effect limits the hole occupancy of core states to one, which is manifested in a virtually complete suppression of Auger recombination and a considerable extension of the shell-hole lifetime (to more than 600 ps) in the presence of a core-localized hole. The long shell-hole lifetime simplifies the achievement of population inversion of shell-based states and allows for demonstrating amplified spontaneous emission (ASE) using nanosecond-pulsed laser excitation, while much "faster" femtosecond excitation is required to obtain ASE in DiB-NCs without a structural interlayer.

2.1 - Synthesis and Microstructural Characterization

CdSe/CdS NCs with an ultrathick shell with identical sizes and compositions were synthesized following two variations of the "fast" synthesis route.[93,130] The DiB NCs with heterogeneous shell (Z/W-NCs), have been synthesized starting from the CdSe core and successively overcoated with the bulk-like shell.[130] Specifically, zincblende CdSe NCs were synthesized by previously reported methods.[166] For the synthesis of CdSe(R = 1.5 nm)/CdS NCs, 2×10^{-7} mol of CdSe NCs (purified twice) dispersed in 10 mL of 1-octadecene were loaded into a 100 mL flask and degassed at 110 °C for 1 h. The flask was filled with Ar and heated up to 300 °C for CdS shell growth. A 0.2 mmol sample of Cd-oleate and 0.2 mmol of 1-dodecanethiol was added slowly (0.1 mmol/min), and the reaction mixture was maintained at the elevated temperature for 30 min to form a thin CdS buffer layer (~3 monolayers) on top of CdSe cores. For further CdS shell growth, a mixed solution of Cd-oleate and trioctylphospine-sulfur (0.5 M/0.5M) in

1-octadecene was continuously added at a rate of 1 mmol/h at 300 °C. After the injection of precursors was completed, the reaction products were cooled to room temperature and purified repeatedly by a precipitation and redispersion method. The final products were dispersed in hexane for further characterization. The homogeneous shell DiB NCs (W/W-NCs), on the contrary, first synthesized CdSe seeds at 380 °C,[93] according to the method described by Carbone *et al.*[105] After synthesis, the NCs suspensions were purified by precipitating them with methanol, followed by centrifugation and resuspension in toluene (procedure repeated 3 times). For the shell growth, Cd and S precursors were prepared separately as a 0.5 M solution of trioctylphosphine sulfide and Cd-oleate dissolved in 1-octadecene, respectively. Next, 2×10^{-7} mol of CdSe NCs were added to 10 mL of 1-octadecene and heated up to 300 °C. Depending on the desired shell thickness, an appropriate amount of the precursor solutions was mixed, loaded in a syringe, and added dropwise over the course of 0.5–4 h. After synthesis, the samples were purified by precipitation with isopropanol, followed by centrifugation and resuspension in toluene. A second purification step was performed with methanol as a nonsolvent, and samples were finally suspended in toluene.

The band diagrams of the two CdSe/CdS heterostructures based on bulk energies are depicted in Figure 2.2a,b. In Table 2.1 I report the literature experimental and theoretical values of the conduction band (ΔE_{CB}) and valence band (ΔE_{VB}) shifts in CdSe NCs in both ZB and WZ crystal structures with respect the bulk energy gap due to quantum confinement effects. The confinement-induced energy shifts are much larger for the conduction band than for the valence band because of a much smaller effective mass of an electron with respect to a hole mass in II-VI semiconductors. In Table 2.2, literature data for the CB and VB energy offsets

Band-edge energies (*vs.* vacuum) in CdSe(ZB)/CdS(ZB)/CdS(WZ) heterojunctions reconstructed from literature data for CdSe NCs, thin CdS layers and bulk CdS

	CdSe NC	CdS layer	CdS bulk
Conduction Band	-4.3[3]	-4.15[5]	-4.11[7]
Valence Band	-6.0[3]	-6.65[5]	-6.31[7]

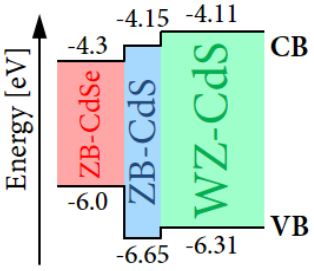

Table 2.3 Band-edge energies (*vs.* vacuum) in heterojunctions of CdSe(ZB), CdS(ZB), CdS(WZ) resembling the structure of Z/W DiB-NCs studied in the present work.

between the ZB and WZ phases of CdS are also reported. Finally, in Table 2.3, I report CB and VB energies of nanostructured and bulk materials that resemble the three different elements of Z/W-NCs; these include ZB CdSe NCs, ZB CdS quantum well structures, and WZ bulk CdS. In all cases, the CB energies are essentially aligned, which explains why the electron wave function is delocalized over the entire DiB-NCs. This is also in agreement with theoretical calculations by Viswanatha and Sarma indicating a CB offset of ≤100 meV.[167] The electrostatic attraction by the core-localized hole gives rise to of a donor-like core exciton, in agreement with theoretical calculations by Shabaev and Efros.[104] The WZ-CdS interlayer separating the CdSe core and the CdS shell, introduces a potential barrier in the VB that exceeds the kinetic energy of bulk-like shell holes, thereby dramatically slowing down the rate of hole capture by core states, as I will show in the next Section.

The only distinction between the Z/W- and W/W-NCs is in the internal crystal structure of the core and the shell. Specifically, one type of CdSe/CdS DiB-NCs is similar to those reported in refs. [153], [109] and [168] and is prepared using pre-synthesized CdSe cores (radius R = 1.5 nm) with the ZB crystal structure (Figure 2.2a). In these systems, during the initial shell growth (up to the shell thickness H = 3.5 nm), the CdS layer grows epitaxially assuming the ZB structure of the core. If the growth of the shell continues further, its structure switches to a more thermodynamically stable WZ phase,[130] as illustrated by the X-ray diffraction patterns in Figure 2.2c. The powder X-Ray Diffraction patterns shown were obtained with a Rigaku SmartLab 9W diffractometer in Bragg-Brentano geometry operating the X-ray source at 40 kV and 150 mA. As a result, the CdS shell becomes polymorphic with an intermediate ZB layer immediately adjacent to the CdSe core, followed by a thick layer of WZ CdS, which occupies most of the shell volume. Hereafter, these structures are referred to as Z/W-NCs. The other type of samples is synthesized using WZ CdSe cores, so that the whole CdS shell grows homogeneously in the WZ phase (hence referred to as W/W-NCs, Figure 2.2b and 2.2d). I note that in the case of the W/W-NCs, the ⟨002⟩ diffraction peak at 2θ = 26° is slightly more intense than the adjacent ⟨001⟩ and ⟨101⟩ peaks (2θ = 25° and 28°, respectively), which might suggest the presence of small ZB domains. These domains, however, are likely distributed across the entire NC volume but not localized at the core/shell interface as in the Z/W-NCs.[169] As a result, these structures are not expected to contain an interfacial potential barrier which would impede the relaxation of shell-localized holes into the core states (Figure 2.2b).[93]

Importantly, in both W/W- and Z/W-NCs, the core/shell interface is significantly sharper than the smooth compositionally graded interface in thick-shell CdSe/CdS NCs fabricated via the SILAR method. This procedure requires long reaction times and fairly high temperatures (~300 °C), conditions that favor the formation of an alloyed region between the CdSe core and the CdS shell.[94] This structural difference between the NCs grown by the fast and the slow shelling methods is evident in Figure 2.3, where I compare the fluorescence line narrowing (FLN) spectra of both DiB systems from the present study to the FLN spectrum of the SILAR-grown giant CdSe/CdS NCs with the same core size (R = 1.5 nm) and the shell thickness of approximately 7.5 nm. In the FLN experiments, the samples are excited with a spectrally narrow photoexcitation continuous wave light source (<0.2nm full width at half-maximum) on the red edge of the band-edge 1S absorption feature, which allows one to selectively excite only

a small fraction of the larger NCs from the ensemble and thereby to effectively narrow down the inhomogeneous broadening of the emission profile. The spectral narrowing was produced by filtering the output of a 150 W xenon lamp with a 1/3 m double grating monochromator. The photons emitted by the samples at cryogenic temperature (3.5 K) were collected, fiber-coupled into a 1/2 m spectrograph and detected with a liquid nitrogen cooled charge coupled device. As a result of this spectroscopic size selection, using FLN it is possible to resolve spectral features due to phonon-assisted transitions involving various longitudinal optical (LO) modes and thereby to probe the composition within the NC volume sampled by the photogenerated carriers.

To compare the FLN spectra of the different NC systems, I normalized them in such a way as to match the intensity of the first CdSe LO-phonon replica (LO_{CdSe}; the corresponding phonon energy $h\nu_{CdSe}$= 25 meV). Inspecting the spectra in Figure 2.3, I noticed two significant differences between the DiB-NC samples obtained via a fast shelling technique (red lines) and giant core/shell NCs synthesized via SILAR method (gray shading). First, in both Z/W- and W/W-NCs, the FLN peak at 35 meV arising from radiative recombination of the core exciton

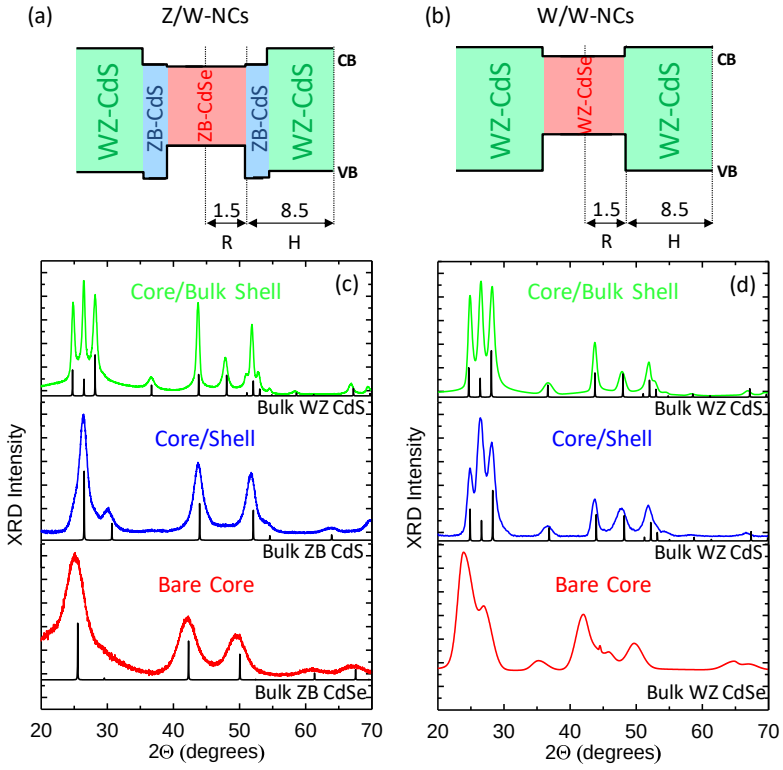

Figure 2.2 Band alignment diagrams of CdSe/CdS DiB-NCs with the 1.5 nm core radius (R) and the 8.5 nm shell thickness (H). (a) The CdSe/CdS DiB-NCs featuring a CdSe core with the zincblende (ZB) structure overcoated with an epitaxial layer of CdS in the ZB phase, followed by a thick shell of CdS with the wurtzite structure (WZ). (b) The CdSe/CdS DiB-NCs consisting of a CdSe core with the WZ structure overcoated with a thick shell of CdS also with the WZ structure. (c,d) X-ray diffraction patterns (XRD) of the two systems at various stages of shell growth (H = 0, 3.5, and 8.5 nm are shown with red, blue, and green lines, respectively), together with the patterns of bulk CdSe and CdS (black lines) in the WZ and ZB structures. Due to its large volume, the final WZ CdS shell dominates the XRD spectrum of both DiB-NC systems.

coupled to the CdS LO mode (LO_{CdS}; $h\nu_{CdS}$ = 35 meV) is much weaker than in SILAR-synthesized giant CdSe/CdS NCs. This suggests that the core localized exciton in DiB-NCs extends over a significantly smaller portion of the CdS shell with respect to g-NCs. Another difference is in the relative intensity of the FLN feature associated with the $CdSe_xS_{1-x}$ interfacial alloy mode ($LO_{S-Cd-Se}$) with energy $h\nu_{CdSeS} = h\nu_{CdSe} + h\nu_{CdS}$ = 60 meV. In both types of the DiB-NCs it is weaker than the second overtone of the LO_{CdSe} vibronic feature at $2h\nu_{CdSe}$ = 50 meV. On the other hand, in giant NCs the intensity ratio reverses indicating a significant enhancement in the alloy-related feature. I would like to point out that the FLN spectrum of SILAR CdSe/CdS giant NCs (ref. [94]) reported in Figure 2.3 for a direct comparison with the DiB-NCs indicates that the graded region in SILAR NCs is ~0.5 nm thick, which corresponds to ~1.3 monolayers of CdSeS alloy. The intensity of the FLN signal, which corresponds to the alloy mode ($LO_{S-Cd-Se}$ vibration) in DiB-NCs, is less than half of that in SILAR NCs. This indicates that the alloyed region is much thinner and thus the interface is very "sharp". These observations confirm that the fast shelling routes used to grow DiB-NCs are not accompanied by a significant inter-diffusion of anions at the core/shell interface and hence lead to a more abrupt interface between the two parts of the heterostructure than in giant NCs grown by SILAR. The absence of the gradual compositional gradient between the core and the shell, which results in a sharp potential step at the interface, is a general feature of both types of DiB nanostructures studied here, and it is most likely responsible for markedly different hole localization dynamics between the DiB-NCs[130] and more traditional giant CdSe/CdS NCs with unintentionally or intentionally alloyed interfaces.[92,164]

The effect of the sharp versus smooth, graded interface on electronic properties of heterostructured NCs was recently analyzed experimentally and theoretically for dual-emitting thick-shell PbSe/CdSe NCs.[170] In these nanostructures, that can be viewed as infrared analogs of giant CdSe/CdS NCs, the hole is also strongly confined to the core, while the electron is delocalized over the entire volume of the NC. The modeling of PbSe/CdSe NCs in refs. [152] and [170] indicated that in the sharp interface case, hole states exhibited two distinct types of spatial distributions: preferentially core versus preferentially shell localization. These core- and shell-type states were virtually electronically decoupled from each other and further separated by a sizable energetic gap right below a quasi-continuum of shell localized levels. These factors, that were inhibiting relaxation of shell-localized holes into the core states, were invoked to explain the development of the shell-related PL band detected in experimental studies.

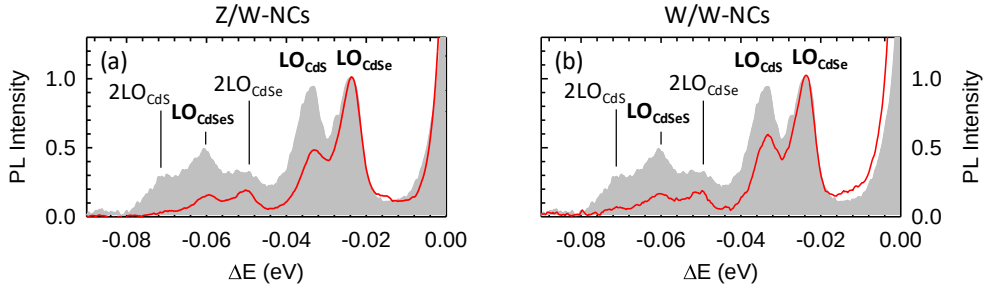

Figure 2.3 FLN spectra of (a) Z/W- and (b) W/W-NCs (red lines) at T = 3.5 K and E_{exc} = 1.96 eV compared to that of a CdSe/CdS core/shell sample with R = 1.5 nm and H = 7.5 nm produced via a SILAR method (gray shading from Ref. [94]).

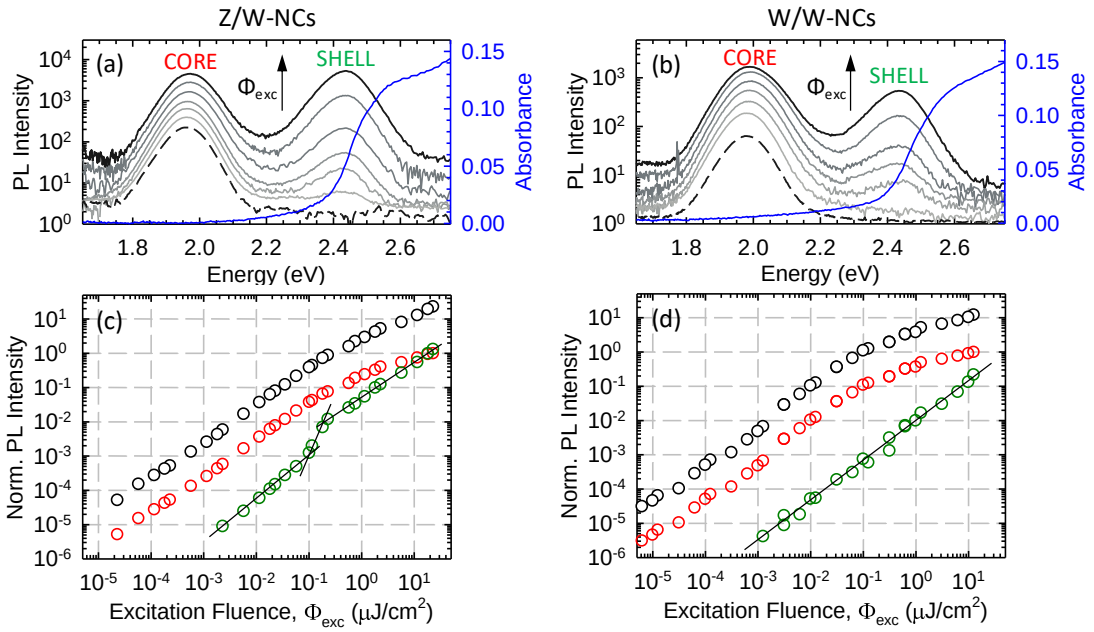

Figure 2.4 PL spectra of CdSe/CdS (a) Z/W- and (b) W/W-DiB-NCs (R = 1.5 nm, H = 8.5 nm at progressively higher excitation fluence (Φ_{exc}). Both samples show simultaneous emission from the core (1.9 eV) and the shell states (2.4 eV). At the highest excitation fluence, the shell/core emission ratio is 1.05 for the Z/W-NCs, while for the W/W-NCs it is only 0.25. The absorption spectra (blue lines) demonstrate that in both samples, excitons are mainly generated in the thick CdS shell. Spectrally integrated intensity of core (open red circles) and shell (open green circles) PL as a function of Φexc for the (c) Z/W-NCs and (d) W/W-NCs. The total PL intensity (open black circles) of both samples has been multiplied by a factor 10 for clarity.

According to the modeling, the situation was different in the case of the graded interface. Specifically, incorporation of even a single additional step into the interfacial potential immediately produced "intra-gap" states with the gap separating the core-and shell-localized hole levels. These intermediate states can facilitate hole relaxation into the core by removing the "phonon bottleneck" which otherwise exists in the sharp interface case. The difference in the interfacial properties between nominally identical samples was likely responsible for a large variation in the shell-emission quantum yields observed in refs. [152] and [170].

A similar difference likely exists between the CdSe/CdS DiB samples grown by the fast shelling method, which results in a sharp core/shell interface, and the giant and bulky-shell NCs with a smooth alloyed interface. This interpretation is corroborated by recent results showing that photoannealing of Z/W-NCs by prolonged exposure to pulsed laser radiation at 3.05 eV leads to progressive transition from the dual-emission regime to the conventional core-only emission due to gradual acceleration of the hole relaxation from the NC shell to the core.[171] As a result, annealed Z/W-DiB-NCs exhibit photophysics which is largely similar to that of giant CdSe/CdS NCs with alloyed (intentionally or unintentionally) ultra-thick shells that were reported to consistently exhibit luminescence exclusively due to core-localized holes at excitation levels as high as several hundreds of excitons per NC.[92,94,99,164]

2.2 - Pump Intensity Dependence of Dual Emission

While the two DiB samples share similar distinctions when compared to thick-shell NCs with alloyed-interfaces, in many aspects they are also different from each other. Some of these differences are highlighted in Figure 2.4. Figure 2.4a,b shows the typical optical absorption and photoluminescence (PL) spectra of Z/W-NCs (a) and W/W-NCs (b) under pulsed excitation with spectral energy E_{exc} = 3.05 eV, which corresponds to excitation of primarily the shell region due to its much larger absorption cross section compared to the core[164] (shell volume is *ca*. 300 times larger than the volume of the core). Optical absorption spectra were measured with a Varian Cary 50 spectrophotometer, whereas steady-state PL spectra were excited by a frequency-doubled Ti:sapphire laser (excitation energy 3.05 eV, pulse duration 150 fs, repetition rate 76 MHz) and collected with a liquid nitrogen cooled Intrument SA Spectrum One CCD coupled to a Horiba Scientific Triax 180 monochromator. At low excitation fluences (Φ_{exc}), corresponding to average per-dot excitonic occupancy $\langle N \rangle \ll 1$, both systems exhibit exclusively core-related PL at ~1.9 eV. Upon increasing Φ_{exc}, for both samples, I observe the emergence of shell emission at ~2.4 eV which is close to the band-edge energy of bulk CdS. Interestingly, the shell emission in both systems becomes detectable at excitation fluence of $\langle N \rangle < 0.1$ that are well below the onset of the biexciton regime. While dual emission was previously observed in Z/W-NCs,[130,133] its observation for the W/W-NCs, especially at such low pump fluencies, at first might seem to be unexpected, since the W/W-NCs do not contain any

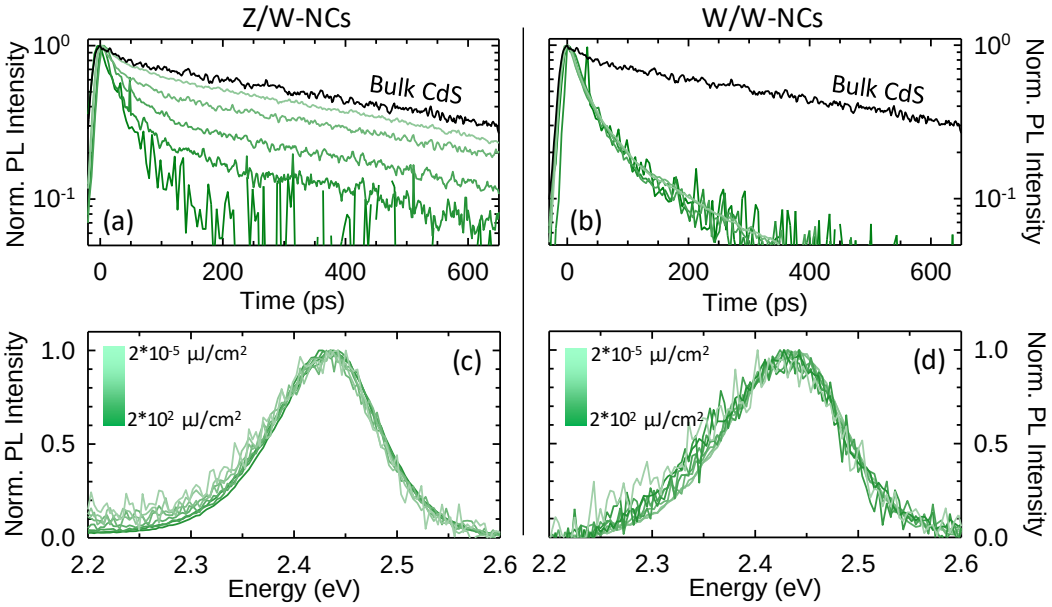

Figure 2.5 Shell PL decay traces for (a) Z/W-NCs and (b) W/W-NCs at increasing excitation fluence (0.05 μJ/cm^2 < Φ_{exc} < 20 μJ/cm^2, excitation energy 3.05 eV). Completely different behaviors are observed for the two DiB-NC systems: upon increasing Φ_{exc}, the shell PL decay of Z/W-NCs slows down from ~45 to ~625 ps, approaching the PL dynamics of bulk CdS (black line). In contrast, for W/W-NCs the PL lifetime is ~45 ps independent of the excitation fluence. Normalized shell PL of (c) Z/W- and (d) W/W-NCs upon increasing excitation fluence (0.02 μJ/cm^2 < Φ_{exc} < 20 μJ/cm^2, excitation energy 3.05 eV).

interfacial barrier which would inhibit hole relaxation from the core to the shell. However, it can be rationalized in light of the previous discussion on the effects of the sharp versus smooth interface as well as previous literature studies of various core/shell systems.[172,173] The observation of efficient shell PL from the W/W-DiB-NCs, therefore, provides another piece of evidence that the sharp interfacial potential helps slow down hole shell-to-core relaxation to a degree which is sufficient for realizing efficient shell emission even without an interfacial barrier.

The slowing of hole relaxation is evident from time-resolved measurements of shell PL dynamics (Figure 2.5a,b). The PL decay traces of shell emission in the sub-nanosecond regime were measured by exciting the samples with the same Ti:sapph laser as in steady-state experiments and collecting the emitted photons with a Hamamatsu streak camera. Figure 2.5a,b reveals that at low Φ_{exc}, when the dominant relaxation process is hole transfer to the core, the PL decay time is approximately 45 ps in both DiB-NC systems, which is over 2 orders of magnitude slower than in CdSe/CdS heterostructures synthesized via seeded growth[110] or SILAR methods.[164] However, despite this similarity, the two systems show very different pump-intensity dependent behaviors. Specifically, the Z/W-NCs show systematically more intense shell PL than the W/W-NCs, which eventually overtakes the core emission at sufficiently high excitation fluencies. Furthermore, the data in Figure 2.5a,b reveal markedly different dependence of the shell PL dynamics in the two types of the NCs on Φ_{exc}. As Φ_{exc} is increased, Z/W-NCs show progressive growth of a slow decay component with the time constant of ~625 ps (Figure 2.5a), which is similar to that of bulk CdS (black trace in Figure 2.5a,b), and therefore, can be ascribed to radiative recombination of bulk-like shell-

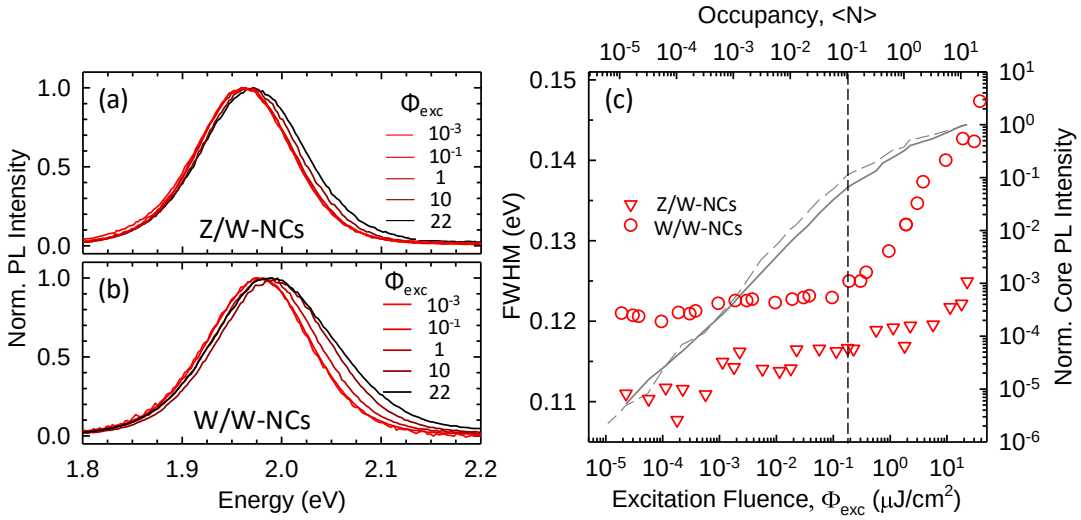

Figure 2.6 Normalized core PL spectra of CdSe/CdS core/shell NCs (R = 1.5 nm, H = 8.5 nm) with (a) heterogeneous (Z/W-NCs) and (b) homogeneous (W/W-NCs) shell structures as a function of excitation fluence (Φ_{exc}). (c) Full width at half-maximum (fwhm) for both samples at increasing Φ_{exc}. The Z/W-NCs (triangles) exhibit a slight increase in the fwhm, while strong broadening is observed for the W/W-NCs (circles) with the onset at ~ 0.5 μJ/cm^2, corresponding to the excitation fluence at which the core PL intensity starts to saturate (solid and dashed grey lines for the Z/W- and W/W-NCs, respectively).

based excitons.[130,161] This effect was previously observed in ref. [130], where it was explained by the activation of the Coulomb blockade of the core upon the capture of the first photogenerated hole, which prevented relaxation of additional holes into the core states. Because of this effect, the increase in Φ_{exc} gradually increases the portion of the NCs in the ensemble with an occupied core and thus producing PL from the shell-based states in addition to core emission. In contrast to this behavior, the shell PL decay in the W/W-NCs is unaffected by increasing Φ_{exc} (Figure 2.5b), which indicates the absence of the Coulomb blockade for core occupancies up to 10 excitons per NC. This suggests that, in the W/W-NCs, the core can accommodate multiple holes similarly to conventional giant CdSe/CdS NCs,[99,164] and hence, its occupancy has virtually no effect on dynamics of shell-based carriers, as opposed to the situation in the Z/W-NCs where the occupancy of the core states controls the relaxation of shell-localized holes via the Coulomb blockade process.

Yet another distinction between the two types of the DiB-NCs is observed in the measured dependence of the emission intensity on Φ_{exc} (Figure 2.3e,f). In Z/W-NCs, the total, spectrally integrated PL intensity (black open circles) shows essentially linear growth across the whole range of studied pump fluencies (up to $\langle N \rangle \sim 10$), indicating that the total PL quantum yield is independent of the NC occupancy. This further suggests that in the Z/W-NCs, the nonradiative Auger recombination is inactive even in the case of very high NC occupancies. On the other hand, the total PL intensity of W/W-NCs shows saturation above ~0.2 μJ/cm^2, indicating the onset of nonradiative deactivation via the Auger process.

The analysis of the core and shell PL behaviors allows to gain further insights into the mechanisms underpinning the difference in the fluence dependence of the total PL between the two systems. In both types of the DiB-NCs, the core PL shows a qualitatively similar behavior (red open circles in Figure 2.4c,d). It first grows linearly and then starts to saturate at ~0.2 μJ/cm^2. The behaviors of shell PL are, however, different between the two systems. In the Z/W-NCs, the shell emission shows multiple regimes in the dependence on Φ_{exc}. It starts with a linear growth ($\Phi_{exc} < 0.08$ μJ/cm^2, $\langle N \rangle < 1$), which is followed by a superlinear increase (0.08 μJ/cm$^2 < \Phi_{exc} < 0.2$ μJ/cm^2, $\langle N \rangle \sim 1$), and then again a linear dependence ($\Phi_{exc} > 0.2$ μJ/cm^2, $\langle N \rangle \gg 1$). The observation of the superlinear growth of the shell PL intensity indicates that the saturation of the core PL observed in the same range of pump fluences is not due to the onset of nonradiative Auger recombination, but instead is due to the Coulomb blockade mechanism[130] which limits the occupancy of the core hole states (and hence core PL) and forces the extra holes to recombine radiatively via the shell states. While leading to the redistribution of the photogenerated carriers between the two emission channels, this mechanism preserves the total number of emitted photons which explains the uninterrupted linear growth of the total PL signal. The activation of the hole-blocking effect in DiB-NCs with a polytypic crystal structure suggests a potential strategy for tuning the carrier dynamics through control of the thickness and/or the height of the core/shell potential barrier, which would affect the hole capture rate by core-based states.

In contrast to the above behavior, in the W/W-NCs the shell PL intensity shows a linear dependence on Φ_{exc} for over 4 orders of magnitude, in agreement with observations of pump-independent shell PL dynamics (Figure 2.5b). As a result, the total PL intensity follows the same

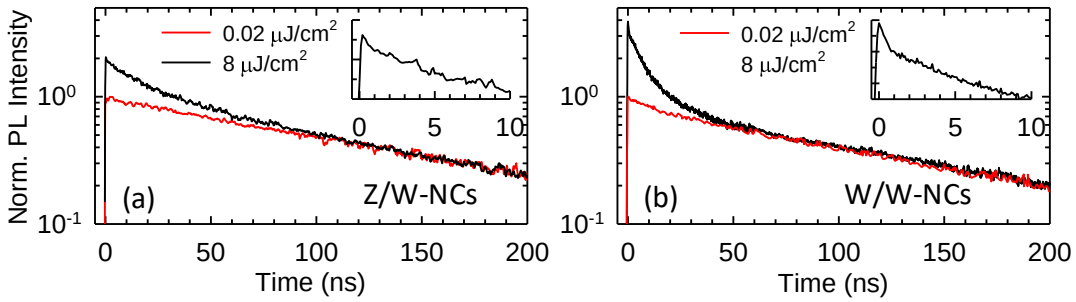

Figure 2.7 Decay traces of core PL for the (a) Z/W- and (b) W/W-NCs at Φ_{exc} of ~ 0.02 μJ/cm^2 (red lines) and ~ 8 μJ/cm^2 (black lines). Insets: an expanded view of the initial portion of the decay curve highlighting the fast contribution due to Auger recombination in W/W-NCs.

trend with increasing Φ_{exc} as the core emission that is it saturates at high pump fluencies as a result of activation of Auger decay dominated by the positive trion channel, i.e., the processes where the energy released in the core-exciton recombination is transferred to another hole coexisting in the core.

2.3 - Properties of Core-Based Photoluminescence

In light of the above observations, I expect that the W/W-NCs favor formation of multiple core exciton states, while the Z/W-NC can support only a single core-localized exciton. This conclusion is supported by the analysis of the Φ_{exc} dependence of the core emission spectra and decay dynamics as elaborated below. Figure 2.6a displays the normalized spectra of the Z/W-NCs core emission as a function of Φ_{exc} for the same pump fluencies as in Figure 2.4a.

In agreement with the expected suppression of formation of multiple core excitons,[174,175] the PL band shows only a weak change in its shape and position with increasing Φ_{exc}. In contrast, the core PL spectrum of the W/W-NCs exhibits a progressive broadening on its high-energy side (Figure 2.6b) due to the increasing fraction of NCs with the cores occupied by biexcitons that are repulsive in these quasi-type-II nanostructures and, therefore, emit on the blue side of the single-exciton band.[175] The difference between the two types of samples becomes particularly pronounced in the plots of the full width at half-maximum (fwhm) *vs* Φ_{exc} (Figure 2.6c). In the W/W-NCs, the fwhm is almost independent of Φ_{exc} at low fluencies, but at Φ_{exc} > 0.5 μJ/cm^2, it starts to rapidly increase (red open circles in Figure 2.6c). Interestingly, the onset of PL broadening matches that of core PL intensity saturation (Figure 2.4d; also shown by gray lines in Figure 2.6c for direct comparison), indicating that both are associated with the onset of the regime of the multiexciton occupancy of the core states. On the other hand, under the same conditions, the core-PL bandwidth in the Z/W-NCs does not show any pronounced changes, suggesting that the core still remains occupied with just a single exciton. I would like to point out that in both systems, the shell PL spectra do not show any significant spectral broadening at high fluencies (Figure 2.5c,d). This behavior is consistent with the bulk-like character of shell-based excitons. As was discussed earlier, they can be viewed as tightly bound excitations that even at high NC occupancies only weakly interact with each other due to their small spatial extent and the overall charge neutrality.

An additional piece of evidence for the limited occupancy of core hole states in the DiB Z/W-NCs with a polymorphic shell is provided by the analysis of the core PL dynamics as a function of Φ_{exc} reported in (Figure 2.7a). To perform this experiment, the repetition rate of the Ti:sapph laser has been reduced to 760kHz to match the nanosecond time regime of the core PL decay with a pulse picker based on a Conoptics 350-160 electro-optical modulator. The PL dynamics were measured with a Hamamatsu R943-02 time-correlated single-photon counting unit coupled to an Oriel Instrument Cornerstone 260 monochromator. At low Φ_{exc} (0.02 μJ/cm^2, corresponding to $\langle N \rangle < 0.01$, red traces), both systems show fairly slow dynamics controlled by the single exciton lifetime, which is τ_X = 150 ns and τ_X = 105 ns, for the Z/W and the W/W sample, respectively. As Φ_{exc} is increased to 7.9 μJ/cm^2 ($\langle N \rangle \geq 1$, black traces), faster decay components emerge for both samples, however their dynamics and amplitudes are different for the two samples (Figure 2.7). In the Z/W-NCs, the fast component has approximately the same amplitude as the single exciton signal, and its characteristic time is ~30 ns. This time constant is consistent with the radiative decay time of a core-localized charged exciton (so-called, trion), the state which is expected for the situation when the core hole occupancy cannot exceed one. Indeed, when the core is already occupied with an exciton, the second hole is blocked from the core, however, the second electron can still populate the 1S state of the core exciton forming a negative trion.[93,176,177] The pre-existing core hole can recombine with either of the 1S electrons, which accelerates its radiative dynamics, as observed in the measurements.[178] Additional acceleration may occur due to a weak contribution from Auger recombination; while this process is largely suppressed in the Z/W-NCs (compared to the W/W structures), it can still be operative on slow, ns timescales probed in measurements of Figure 2.7.

In the case of the W/W sample, the fast dynamics emerging at higher pump levels is approximately twice as large as in the Z/W sample. It also exhibits a trion-like, tens-of-ns component. However, in addition, it also shows a very fast initial decay unresolved in these measurements and manifested as a sharp spike (insets of Figure 2.7). This very fast early time dynamics is a clear manifestation of Auger recombination of core excitons, the process leading to the progressive saturation of the core emission intensity as well as the overall PL signal at high pump fluences (Figure 2.4d).

2.4 - Ultrafast Transient Absorption Measurements

To resolve Auger decay in the W/W sample, I use ultrafast transient absorption (TA) measurements (Figure 2.8). For these experiments, the laser source was a Ti:sapph with a chirped pulse amplification (Coherent LIBRA-HE), which provided 95 fs pulses at 800 nm at a repetition rate of 1 kHz. The excitation pulses were generated by frequency doubling the fundamental beam in a 2 mm thick β-barium borate crystal. The probe beam was a white light supercontinuum obtained by focusing a fraction of the fundamental pulse onto a 2 mm thick sapphire plate. The supercontinuum spectrum extends almost continuously from 450 nm to 1.6 μm, with a gap only around the fundamental wavelength at 800 nm. A computer-controlled optical multichannel analyzer acquired the map of the chirp-free differential transmission $\Delta T/T = (T_{on} - T_{off})/T_{off}$, as a function of the pump-probe time delay, on the visible part of the probe spectrum. T_{on} and T_{off} are the probe spectra transmitted by the excited and unperturbed

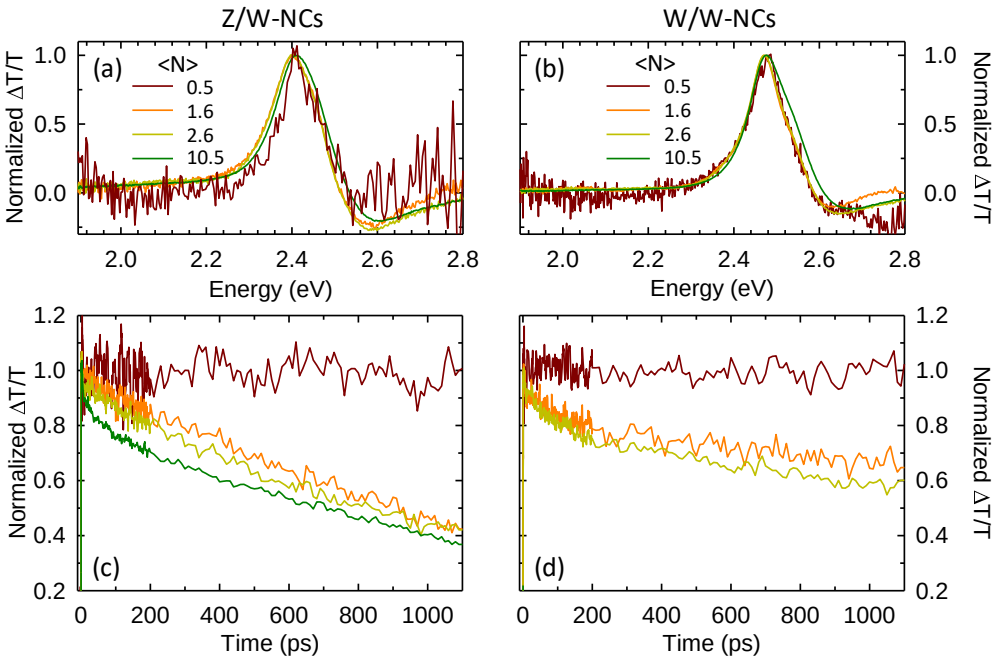

Figure 2.8 TA spectra of the (a) Z/W and (b) W/W CdSe/CdS NCs for NC occupancies ⟨N⟩ = 0.5, 1.6, 2.6, and 10.5 (3.05 eV excitation, 2 ps pump−probe delay for all spectra). The corresponding photobleaching dynamics are shown in panel (c) for the Z/W-NCs (probe energy is ~ 2.4 eV for all dynamics but ⟨N⟩ = 0.5; the trace shown for ⟨N⟩ = 0.5 is obtained by spectral integration of the probe signal between 2.34 and 2.48 eV) and (d) for the W/W-NCs (probe energy ~ 2.48 eV for all dynamics but ⟨N⟩ = 0.5; the trace shown for ⟨N⟩ = 0.5 is obtained by spectral integration of the probe signal between 2.42 and 2.55 eV). The same color scheme applies to all panels.

sample, respectively. The TA spectra of both samples (Figure 2.8a,b) are dominated by intense photobleaching (PB) band at ~2.4 eV, which corresponds to the shell-localized excitons. Because of its much smaller absorption cross-section, the core is not resolved in the TA measurements. In II−VI NCs, the bleach signals are primarily due to Pauli blocking of widely separated electron levels. The hole states are usually not resolved because they are closely spaced, and therefore, single-state occupation numbers are considerably smaller than those of electron states. Based on these general considerations, the 2.4 eV bleach arises from the filling of the 1S electron state, which is shared between the core and the shell,[82,93,130,133] and hence, bleach time transients report on 1S electron recombination dynamics.

At the low pump fluence (⟨N⟩ = 0.5), the PB decay is undetectable on the short 1 ns time scale of the TA measurements. Such long decay is expected for the DiB-NCs as in this excitation regime in both types of the samples, the photoexcited NCs sub-ensemble is populated exclusively with core excitons. As indicated by measurements in Figure 2.7, such excitons exhibit a very long decay constant of >100 ns. As ⟨N⟩ is increased to *ca*. 1 exciton per dot, the PB dynamics of the Z/W sample accelerate as a result of the increasing fraction of the NCs that, in addition to a core exciton, also contain a shell exciton, which is characterized by sub-nanosecond radiative recombination (Figure 2.5a and Figure 2.8c). On the other hand, the excitation of the second exciton in the W/W-NC leads to a much faster decay with a 80 ps time

constant (Figure 2.8d). This fast decay, manifested as a spike in the lower-resolution PL measurements of Figure 2.7b, arises from Auger recombination of a core-localized biexciton. Its amplitude increases with pump fluence due increasing fraction of doubly excited NCs. The TA data once again confirm my original assessment that in the Z/W-NCs, the core occupancy is limited by one hole, while multiple holes can coexist in the core of the W/W samples.

2.5 - Amplified Spontaneous Emission Due to Shell-Based States

The difference in hole relaxation dynamics also affects optical gain properties of the two DiB-NC systems which I evaluate by comparing their behaviors in side-by-side measurements of

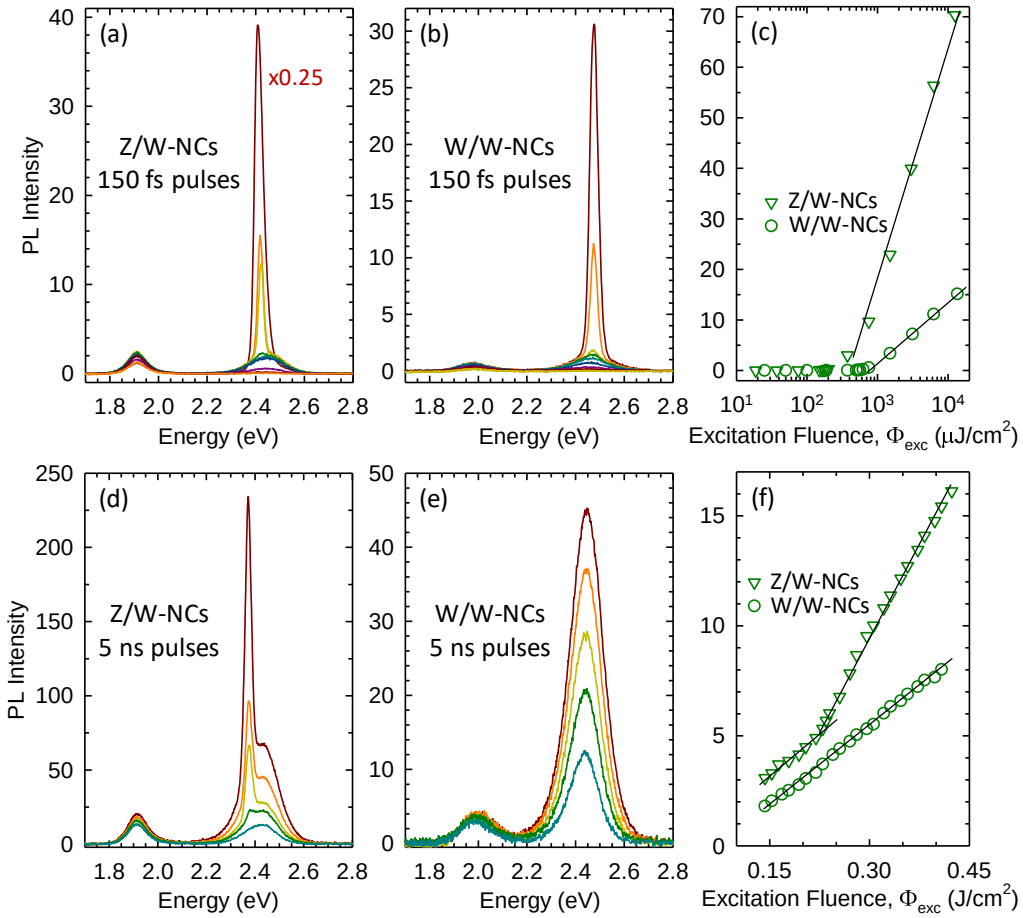

Figure 2.9 PL spectra of the CdSe/CdS DiB-NCs recorded using excitation with 3.05 eV, 150 fs pulses at 2 kHz: (a) a zincblende core and a polymorphic shell (Z/W-NCs) and (b) both the core and the shell have the wurtzite structure (W/W-NCs). Both samples exhibit ASE at ~2.45 eV due to emission from the shell. (c) Integrated shell PL intensity as a function of the excitation fluence (Φ_{exc}) for the Z/W-NCs (triangles) and the W/W-NCs (circles) under excitation with 150 fs pulses: ASE threshold is clearly observable for both samples. In the case of excitation with 5 ns pulses (3.5 eV, 1 kHz), the development of ASE is observed only for (d) the Z/W-NCs, while for (e) the W/W-NCs no ASE is detected at all studied pump fluencies. (f) Integrated shell PL intensity as a function of Φ_{exc} for the Z/W-NCs (triangles) and the W/W-NCs (circles) in the case of 5 ns pump pulses.

amplified spontaneous emission (ASE) using close-packed NC drop-casted films. The emission has been collected normal to the substrate with a CCD camera coupled to a spectrometer with an optical fiber bundle. I start my measurements with femtosecond 3.05 eV nm pulsed excitation focused into a circular spot with the area of 1.3×10^{-2} mm^2 (same Ti:sapph laser used for TA experiments described in the previous Section), which corresponds to excitation of primarily shell-based states. In more traditional giant CdSe/CdS NCs, this type of excitation usually results in the ASE from the core states that become quickly populated by holes relaxing from the shell on the sub-picosecond time scale.[107,171] In sharp contrast, in both DiB samples, ASE is observed not from the core but the shell states (Figure 2.9a,b). This is a direct result of a considerable extension support the development of the avalanche of the stimulated emission photons. After the ASE threshold is reached, shell-based excitons quickly recombine via stimulated emission before holes relax into the core, which prevents the development of ASE from to core-based states. The ASE produced by shell-localized excitons exhibit typical signatures of the optical-gain regime[171] including a pronounced line narrowing with increasing pump fluence, which is accompanied by a fast growth in intensity (Figure 2.9c) with a sharp change in the slope at the onset of the ASE regime.

A profound difference in optical gain properties of W/W- and Z/W-DiB-NCs is observed under nanosecond pulsed excitation. The same NC films were excited using the third armonic of a Nd:YAG laser (3.49 eV, 5 ns pulse duration, repetition rate 1 kHz) focued into a circular spot with the area of 1.9×10^{-2} mm^2. Specifically, using this type of excitation I could not achieve the ASE regime with the W/W-NCs, while it could be readily realized with the Z/W-NCs (Figure 2.9d–f). This difference in behaviors is directly linked to the difference in the lifetimes of shell localized holes (τ_h). In the W/W samples, for all studied fluences τ_h is *ca*. 45 ps (Figure 2.5b). Since it is much shorter than the pulse duration (τ_p = 5 ns), the effective per-pulse fluence is reduced by the factor $\tau_p/\tau_h \approx 100$, which raises the ASE threshold to values not sustainable by the samples. In the case of the Z/W-NCs, the effect of Coulomb blockade slows down hole relaxation by more than 10-fold (τ_h = 625 ps for Φ_{exc} = 17 μJ/cm^2; Figure 2.5a), leading to the proportional reduction of the ASE threshold compared to the W/W sample. Because of this reduction, I was able to realize ASE with high but accessible pump fluence (the ASE threshold was ~0.2 J/cm^2; Figure 2.9d,f) and before damaging the sample.

2.6 - Conclusion

In conclusion, I have performed side-by-side spectroscopic studies on two types of CdSe/CdS DiB heterostructures grown by similar fast shelling techniques that result in the minimal alloying at the core/shell interface, and hence, produce a sharp confinement potential for core-localized carriers. Both types of DiB-NCs are characterized by the same core size and overall dimensions but different crystal structure of their interior. One type of the NCs (W/W-NCs) comprises a WZ CdSe core overcoated with a WZ CdS shell, while the other (Z/W-NCs) has a ZB CdSe core and a two-component (polymorphic) shell, which contains an interfacial ZB layer of CdS, followed a thick layer of WZ CdS. I also compared the properties of the DiB-NCs to those of bulky-shell gradient CdSe/CdS NCs and of more common giant CdSe/CdS NCs synthesized by the SILAR methods which is known to produce a considerable alloying at the core/shell interface resulting in smooth, graded potential for core-localized carriers.[94] The “sharpness” of

the interfacial potential has a profound effect on the rate of hole relaxation from the shell to the core states. In thick-shell NCs with alloyed interface, the hole relaxation is an extremely fast, sub-picosecond process which leads to very fast depletion of shell based states. As a result, independent of whether charge carriers are injected in the core or the shell region, spontaneous emission as well as ASE occur from the core-based states. In contrast to this behavior, the abrupt core/shell interface of DiB-NCs leads to the situation where shell- and core-based states become much weaker coupled to each other compared to the graded-interface case, which leads to a dramatic lengthening of shell-hole lifetimes to ~45 ps in the W/W-NCs and even longer in the Z/W structures. A profound effect of the increased hole relaxation time is a peculiar two-band structure of the PL spectra that contain the shell-emission feature in addition to the usual core-emission band. Further, instead of ASE due to core excitons, the DiB-NCs exhibit ASE arising from the shell-based states, which is another indication of very long shell-hole relaxation times.

While the two types of DiB-NCs have common distinctions from CdSe/CdS thick-shell NCs with alloyed interfaces, in many aspects they differ from each other, which is due to a different structure of their shell. The interfacial layer of ZB CdS in Z/W-NCs, creates a potential barrier in the valence band, which together with Coulomb repulsion leads to a phenomenon of dynamic hole blockade which limits the occupancy of core valence-band states to one hole. As a result, Z/W-NCs feature a significant suppression of Auger recombination manifested in a continuous, almost linear growth of the total PL intensity with pump fluence up to very high NC occupancies of $\langle N \rangle$ more than 10. On the other hand, the W/W-NCs show saturation of the PL signal at $\langle N \rangle \gg 1$, due to the onset of fast Auger recombination of core-localized multiexcitons. Another prominent distinction between the two types of DiB-NCs is the ability of the Z/W structures to produce ASE under excitation with long 5 ns pulses, while no ASE is detected with the W/W samples under the same excitation conditions. This difference relates to the effect of dynamic Coulomb blockade in the Z/W-NCs, which simplifies the achievement of population inversion of shell-based states by closing the fast relaxation channel associated with hole trapping by the core.

These results highlight a profound effect of the composition and the crystal structure of the core/shell interface on carrier dynamics and optical properties of heterostructured NCs. For example, as was demonstrated previously,[92,94] the sharpness of the confinement potential controlled by the degree of the interfacial alloying has a significant effect on Auger recombination. I show that it also has a dramatic effect on the rate of carrier relaxation from the shell to the core, which underpins the ability of the structures with a sharp (unalloyed) interface to produce two-color emission due to both core and shell states. In addition to controlling the sharpness of the core/shell interface, one can manipulate carrier dynamics by incorporating interfacial potential barriers, which can be created using, e.g., a polymorphic shell structure. Together with the quantum-size effect and heterostructuring, the ideas of "*interface engineering*" should allow even for greater flexibility in controlling functionalities of colloidal nanomaterials.

Chapter 3

"Quantized" Doping of Individual Colloidal Nanocrystals Using Size-Focused Metal Quantum Clusters

The insertion of intentional impurities, commonly referred to as doping, into colloidal semiconductor nanocrystals is a powerful paradigm for tailoring their electronic, optical, and magnetic behaviors beyond what is obtained with size-control and heterostructuring motifs. Advancements in colloidal chemistry have led to nearly atomic precision of the doping level in both lightly and heavily doped nanocrystals. The doping strategies currently available, however, operate at the ensemble level, resulting in a Poisson distribution of impurities across the nanocrystal population. To date, the synthesis of monodisperse ensembles of nanocrystals individually doped with an identical number of impurity atoms is still an open challenge, and its achievement would enable the realization of advanced nanocrystal devices, such as optically/electrically controlled magnetic memories and intragap state transistors and solar cells, that rely on the precise tuning of the impurity states (i.e., number of unpaired spins, energy and width of impurity levels) within the nanocrystal host. The only approach reported to date relies on nanocrystal seeding with organometallic precursors that are intrinsically unstable and strongly affected by chemical or environmental degradation, which prevents the concept from reaching its full potential and makes the method unsuitable for aqueous synthesis routes. Here, I overcome these issues by demonstrating a doping strategy that bridges two traditionally orthogonal nanostructured material systems, namely, nanocrystals and metal quantum clusters composed of a "magic number" of atoms held together by stable metal-to-metal bonds. Specifically, I use clusters composed of four copper atoms (Cu_4) capped with D-penicillamine to seed the growth of CdS nanocrystals in water at room temperature. The elemental analysis, performed by electrospray ionization mass spectrometry, X-ray fluorescence, and inductively coupled plasma mass spectrometry, side by side with optical spectroscopy and transmission electron microscopy measurements, indicates that each Cu:CdS nanocrystal in the ensemble incorporates four Cu atoms originating from one Cu_4 cluster, which acts as a "quantized" source of dopant impurities.

Generally, the doping of nanocrystals (NCs) is performed following three main strategies, conventionally named after the stage of the synthesis reaction at which the insertion of the doping impurity takes place: *i*) nucleation doping,[179-181] in which an organo-metallic precursor containing the impurity atom[182,183] is directly mixed with the host precursors prior to nucleation, so that doping occurs directly on the adatom cores.[184] *ii*) Growth doping,[179,181] where the dopant precursors are added to the reactive medium during the growth stage and gradually decorate the NC surfaces that are successively over coated with layers of the same semiconductor material through a homogeneous shelling reaction.[185,186] *iii*) Cation exchange

reactions between undoped NCs and dopant precursors.[135,187,188] In this case, the introduction of the impurities occurs after the completion of the NC synthesis and the doping level is controlled by the relative concentration of NCs and the dopant source, as well as by the choice of ligands and reaction temperature. Cation exchange reactions can also be performed following the so-called *'inverted'* route, as in the case of Ag-doped CdSe NCs starting from Ag_2Se NCs, where the final doped systems are obtained by incomplete substitution of the Ag atoms with Cd ones, which leaves the inner core of the NCs doped with residual Ag impurities.[189] Similar to cation exchange reaction, but without the loss of host cations, 'diffusion doping' has been demonstrated to successfully incorporate large amounts of manganese ions in CdSe NCs.[190,191] Similarly, by reducing the size of the semiconductor host to the near minimum, sub-nanometre sized Mn:ZnTe and Mn:CdSe clusters[188,192] has been obtained with very high relative dopant concentration. Very recently, approaches have been proposed to realize diluted magnetic semiconductor NCs with uniform spatial distribution of impurities by synthesis of a small core containing magnetic ions followed by high temperature annealing and growth of the semiconducting matrix.[193]

Remarkable advancements in the chemistry of NC doping and in particular, in the knowledge of cation exchange reactions, have led to the achievement of nearly atomic precision of the doping level in both lightly and heavily doped NCs.[134,135] Despite successful in fine tuning the average amount of impurities per particle, the common feature of above mentioned NC-doping approaches is that they operate at the ensemble level, yielding a Poisson distribution of dopants across the NCs population. To date, the realization of monodisperse ensembles of NCs individually doped with an identical number of impurity atoms is still an open challenge and its achievement would be highly important from both a fundamental and a technological perspective, as it would offer a platform for investigating the dopant-to-host and dopant-to-dopant interactions that are typically rendered inaccessible by the inhomogeneity in the doping concentration.[194-196] This will enable us to realize and control the behaviour of novel NC devices, such as optically/electrically controlled magnetic memories[196] and intragap state transistors and solar cells that rely on the precise tuning of the impurity states (i.e. number of unpaired spins, energy and width of impurity levels etc.) within the semiconductor host.[197-199]

An important step in this direction has been made by Snee and co-workers[182], who used $[Na(H_2O)_3]_2[Cu_4(SPh)_6]$ organometallic precursors[200] to grow CdSe NCs doped with copper, indicating that monodispersity of the doping level across the NC ensemble can be achieved. The employed complexes, consisting of copper atoms bridged by benzenethiols, were synthesized following a modified synthetic protocol introduced by Dance *et al.*[200] to obtain copper-based hybrid compounds to be employed as monodispersed dopant source. Despite successful in overcoming the Poissonian distribution of dopants in the NC ensemble typical of other doping techniques, these metal complexes require manipulation under inert atmosphere due to their low stability to decomposition and oxidation, which further makes them incompatible with synthesis procedures employing aqueous solvents.

Here, by taking inspiration from that pioneering study, I propose a new quantized doping approach that utilizes a different kind of pre-tuned dopant source that extends the potential of the original strategy and further renders the synthesis procedure compatible with aqueous

solvents and environmental conditions useful for direct application of NCs to biologic and sensing applications.[201] Specifically, I employ metal quantum clusters, consisting of a core of copper atoms held together by stable metal-metal bonds to pre-tune the doping at the single particle level and thereby obtain ensembles of doped NCs, each one of which is grown on the same pre-determined number of impurity atoms. Metal quantum clusters are monodispersed ultra-small particles typically synthesised in aqueous media and highly stable in saline, as well as biologic environments.[202,203] They consist of a precise number of atoms that dictates their electronic properties,[204] which make them technologically appealing in nanomedicine,[202] electronics,[205] photo-catalysis[206] and photonics.[207] This applicative potential has triggered

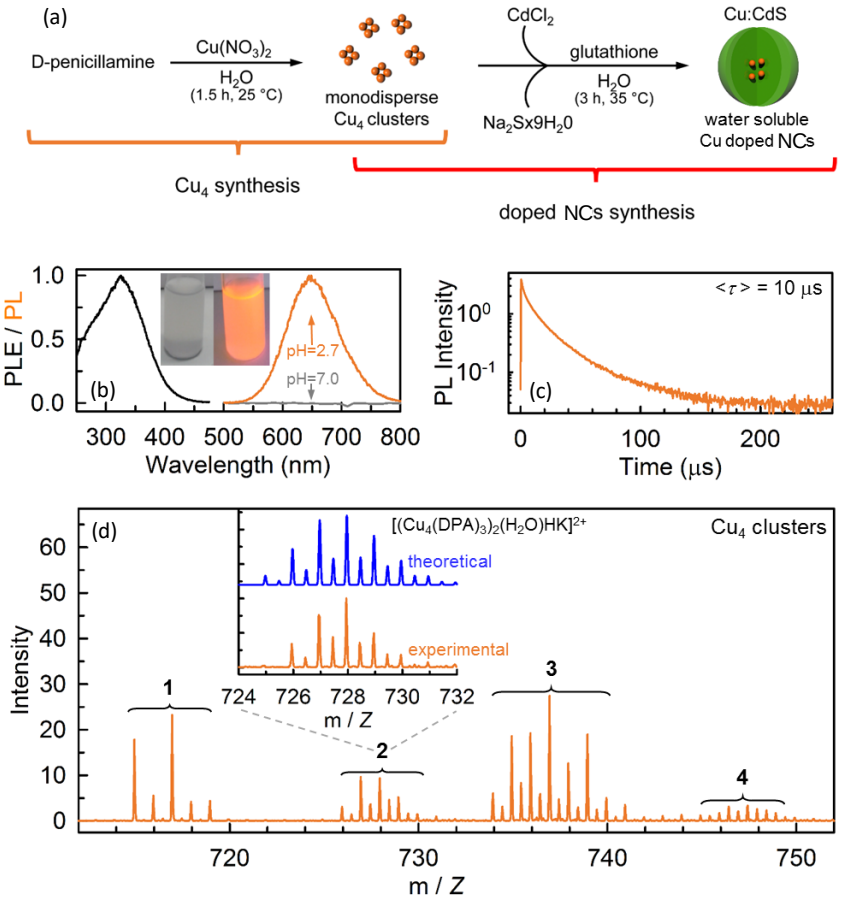

Figure 3.1 Synthesis and characterization of Cu_4 cluster seeds. (a) Schematics of the synthesis strategy of water-soluble copper quantum clusters. The copper clusters were prepared by chemical reduction of the metal precursor $Cu(NO_3)_2$ using D-penicillamine, which also acts as capping ligand. Cu-doped CdS NCs are obtained by seeding QD's nucleation through the addition of Cu clusters. (b) Photoluminescence (PL, orange line) and PL excitation (PLE, black line) spectra of Cu_4 clusters in water (pH = 2.7). (c) PL decay profile collected at 650 nm under pulsed 355 nm laser excitation. (d) Mass spectrum in positive-ion mode of copper clusters in water. All the recorded peaks (1, 2, 3, and 4) are ascribed to metal clusters composed of four Cu atoms. The details on the peak assignment are reported in Table 3.1. Inset: Experimental and simulated isotopic patterns of peak 2 corresponding to $[(Cu_4(DPA)_3)_2(H_2O)HK]^{2+}$.

growing efforts on their synthesis strategies, resulting in a variety of fabrication protocols for preparing clusters consisting of well-defined numbers of gold,[206,207] silver[203,208] and more recently, copper atoms.[209] Besides their chemical and environmental stability, a general feature of metal quantum clusters that is particularly relevant for their use as atomically precise sources of metal impurities for NC doping, is that by using size-focusing methodologies,[210] they can be obtained with monodispersed '*magic numbers*' sizes dictated by specific values of their nuclearity and this ultimately determines the thermodynamic selection of the most stable cluster dimension.[211] Finally, one important beneficial aspect of metal quantum clusters as tailored dopant sources is that they can be synthesized in both pure monometallic compositions, as well as in a large variety of 'alloyed' polymetallic forms,[212,213] which in principle offers an unmatched platform for dual- or multiple-doping through direct incorporation of pre-set arrays of different metal impurities in the semiconductor host, simultaneously ensuring a controlled doping level of all impurities and thereby overcoming the ubiquitous difference in reactivity of mixtures of molecular dopant precursors.

In this study, in order to provide a direct comparison with the approach based on organometallic copper-benzenethiols complexes, I use monometallic metal clusters composed of four copper atoms (Cu_4) as nucleation seeds for cadmium sulphide (CdS) NCs in water, at room temperature and ambient atmosphere, and employ glutathione biomolecules as capping ligands, which might further promote their suitability to bio-imaging and diagnostic applications.[214] The choice of copper as dopant metal is also advantageous due to the consolidated knowledge of the electronic properties of Cu-doped II-VI NCs, which makes the identification of the spectroscopic signatures of copper doping unequivocal.[181,194,215-218] The elemental analysis of the clusters and the doped NCs performed by electrospray ionization mass spectrometry (ESI-MS), X-ray fluorescence and inductively coupled plasma atomic emission spectroscopy (ICP-AES), side-by-side with optical spectroscopy measurements, indicates that each Cu:CdS NC in the ensemble contains four copper atoms and confirms that the growth of the doped NCs is seeded by individual Cu_4 clusters, which act as a 'quantized' source of dopant impurities. This is a fundamental difference with respect to approaches based on conventional doping sources that are typically incorporated in a variable number, leading to statistic distributions of the doping level across the ensemble. The obtained Cu:CdS NCs exhibit the typical spectroscopic properties of Cu-doped NCs synthesized via established nucleation- and growth doping routes,[219] such as long-lived Stokes shifted photoluminescence and insensitivity of the emission efficiency to hole withdrawing agents[215,217], which further confirms the incorporation of the Cu dopants in the bulk of the host NC.

3.1 - Synthesis and characterization of copper clusters

The synthesis route consists of a two-step solution-based bottom-up procedure with the preparation of Cu_4 clusters followed by the nucleation of the CdS NCs, as schematized in Figure 3.1a. Monodisperse water soluble Cu_4 clusters were synthesized using mild reducing conditions of $Cu(NO_3)_2$. Briefly, 40 µL of $Cu(NO_3)_2$ in water (100 mM) were added to 4 mL of the zwitterionic functional ligand D-penicillamine (DPA, 10 mM), which acts also as a mild reductant. The mixture was kept under vigorous stirring at room temperature for a few minutes, after which it turned turbid white due to the low solubility of the clusters in the

reaction mixture at pH = 2.7. Accordingly, the solution showed the characteristic luminescence at ~650 nm (Figure 3.1b) with ~10 μs lifetime (Figure 3.1c) commonly ascribed to aggregation-induced emission copper clusters.[220] After 90 minutes, the clusters precipitated out of solution and were collected and purified by centrifugation and repeated washing with ultrapure water. The final product was re-dispersed in ultrapure water, yielding a clear solution with pH = 7.0 of non-interacting isolated Cu_4 cluster, as confirmed by the disappearance of the characteristic luminescence.

To elucidate the size and monodispersity of the Cu clusters, ESI-MS measurements in positive-ion mode were carried out. ESI-MS experiments in positive-ion mode were performed on a hybrid quadrupole/time-of-flight instrument equipped with a nano-electrospray ion source (AB Sciex, Foster City, CA, USA). The samples were infused by borosilicate-coated capillaries of 1 μm internal diameter (Thermo Fisher Scientific, Waltham, MA, USA). The main instrumental parameters were as follows: ion-spray voltage 1.1 kV; curtain gas 20 psi; declustering potential 80 V. The recorded spectra were averaged over a 1 min acquisition time. The simulation of the peak distributions of the ESI-MS spectra was performed by IsoPro 3.1 based on the Yergey algorithm.[221] The positive mode ESI-MS spectrum of the Cu clusters in water is reported in Figure 3.1d, showing a series of peaks in the *m/z* range between 710 and 755 that are ascribed to clusters composed of four Cu atoms capped by three DPA ligands. Specifically, the peaks are assigned to $[(Cu_4(DPA)_3)(H_2O)]^+$ (**1**, *m/z* = 716.52), $[(Cu_4(DPA)_3)_2(H_2O)HK]^{2+}$ (**2**, *m/z* =727.84), $[(Cu_4(DPA)_3)_2\,(H_2O)_2HK]^{2+}$ (**3**, *m/z* = 736.91) and $[(Cu_4(DPA)_3)_2(H_2O)(K)_2]^{2+}$ (**4**, *m/z* = 746.74). The inset of Figure 3.1d reports the enlargement of peak **2**, highlighting the isotopic pattern of the $[(Cu_4(DPA)_3)_2(H_2O)HK]^{2+}$ mass distribution. The experimental data match closely the corresponding simulated pattern calculated considering the isotopic distribution of the constituent atomic species (theoretical *m/z* = 727.85), thus confirming the formation of Cu_4 clusters capped by three DPA units. The same correspondence between the theoretical and experimental spectrum is found for all other peaks, as reported in Figure 3.2 and Table 3.1. I highlight that the ESI-MS spectrum in the 300-1500 *m/z* range shows no additional features, which confirms the absence of clusters of different size and of cluster aggregates, in agreement with the complete disappearance of the

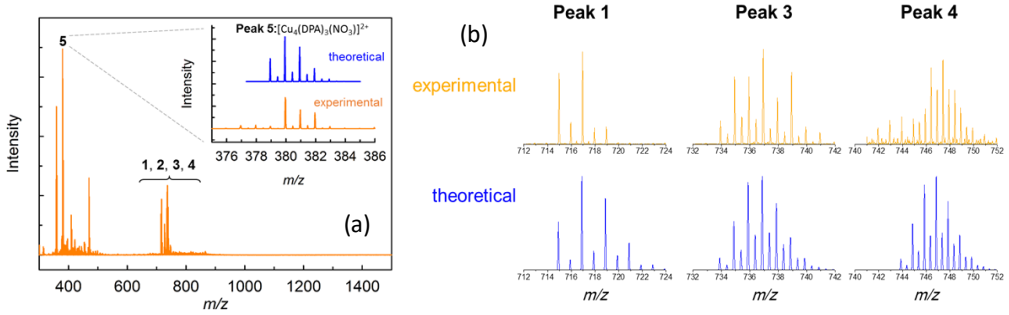

Figure 3.2 (a) Positive mode ESI-MS spectra of copper clusters in aqueous dispersion. The peaks are ascribed to copper clusters composed of four Cu atoms capped by three DPA ligands (1, 2, 3, 4 and 5). The inset shows the agreement between the experimental and simulated isotopic patterns peak 5 corresponding to $[Cu_4(DPA)_3(NO_3)]^{2+}$. (b) Experimental (orange) and simulated (blue) isotopic patterns of the *m/z* peaks not enlightened in Figure 3.1. The details on the peaks assignment are reported in Table 3.1.

Peak assignment for the ESI-MS measurement of Cu cluster in water shown in Figures 3.1 and 3.2

Peak	Chemical Species	Theoretical average *m/z*	Experimental average *m/z*
1	$[(Cu_4(DPA)_3)(H_2O)]^+$	716.81	716.52
2	$[(Cu_4(DPA)_3)_2(H_2O)HK]^{2+}$	727.85	727.84
3	$[(Cu_4(DPA)_3)_2(H_2O)_2HK]^{2+}$	736.86	736.91
4	$[(Cu_4(DPA)_3)_2(H_2O)(K)_2]^{2+}$	746.90	746.74
5	$[Cu_4(DPA)_3(NO_3)]^{2+}$	380.40	380.74

Table 3.1 Formula of the chemical and the adduct species observed in the Cu clusters mass spectrum measurements reported in Figures 3.1 and 3.2, together with the experimental and simulated *m/z* values. DPA is D-penicillamine, H and K are respectively hydrogen and potassium ions present in H_2O, and NO^{3-}, the counter-ion of the correspondent Cu precursor.

aggregation induced luminescence. The purified copper clusters were analysed by means of X-ray photoelectron spectroscopy (XPS) and X-ray induced Auger electron spectroscopy (XAES) in order to investigate the oxidation states of the constituent metal atoms. Measurements were performed on a Kratos Axis UltraDLD spectrometer using a monochromatic Al Kα source operated at 15 kV and 20 mA. The specimen for XPS was prepared by drop casting 200 μL of a clean and concentrated sample solution onto a silicon wafer, thus obtaining a circular drop (approximately 1 cm wide in diameter) on it. All the analyses were carried out over an area of 300 × 700 μm. High-resolution analyses were carried out with a pass energy of 10 eV. The Kratos charge neutralizer system was used during data acquisition. Spectra have been charge corrected to the main line of the carbon 1s spectrum set to 284.8 eV (C−C bond). Spectra were analyzed using Casa XPS software (version 2.3.16). In order to identify the oxidation state of Cu in the Cu_4 clusters, XPS data were collected over the 925-950 eV binding energy range, where the main Cu peaks and satellites should appear. The obtained XPS spectrum (Figure 3.3a) is characterized by two intense peaks centred at approximately 932 eV and 934 eV (due to photoelectrons coming from the $2p_{3/2}$ orbital of Cu), together with a low intensity contribution (shake-up satellites) centred at ~942 eV.[216] The presence of the peak at 934 eV and of the satellites is a clear indication of the presence of Cu^{2+} in the sample.[222] The dominant peak at ~932 eV could be assigned to both Cu^0 and Cu^{1+} species. In order to unequivocal ascribe to either the presence of Cu^0 or Cu^{1+} species, I further investigated the oxidation state of copper by analysing the Cu_{LMM} Auger peak via X-ray induced Auger electron spectroscopy (XAES, Figure 3.3b).[223] The XAES spectrum is featured by an intense peak at kinetic energy of 916 eV, which is peculiar of the +1 oxidation state (for comparison, the position of the Cu_{LMM} peak for metallic Cu is expected at ~918 eV).[216] Therefore, XPS and XAES data confirm that Cu_4 clusters are composed of Cu^+ and Cu^{2+} ions.[210]

3.2 - Synthesis of Cu doped CdS Nanocrystals

Once thoroughly purified and characterized, the Cu_4 clusters were added to the cadmium and sulphur precursors in order synthesize Cu_4-doped CdS NCs (Figure 3.1a). Prior to the

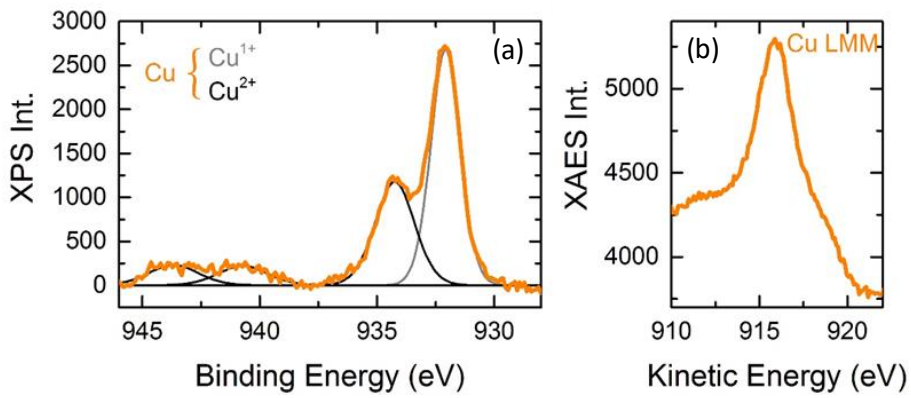

Figure 3.3 (a) X-ray photoelectron spectroscopy (XPS) data analysis for Cu_4 clusters. The experimental spectrum (orange profile) is symptomatic of two copper oxidation states in the sample. (b) The oxidation state of Cu atoms was further confirmed by X-ray induced Auger electron spectroscopy (XAES). The two analyses indicate that Cu_4 clusters are mostly composed of Cu^{1+} and Cu^{2+} ions.

preparation of doped NCs, undoped CdS NCs were synthesized using a modified version of the method in ref. [224] to optimize the reaction parameters and to obtain preliminary guidelines on the Cu_4 clusters concentration required for producing a monodisperse ensemble of Cu-doped CdS NCs in the assumption, confirmed experimentally (see below), that each copper cluster seeds the nucleation of one single CdS NC. Specifically, to synthesize the undoped, reference sample, a 7 mL amount of 0.1 M tripeptide L-glutathione was added to 35 mL of ultrapure water in a two-necked flask under stirring followed by adjusting the pH to 10 by dropwise addition of an appropriate amount of 1.0 M NaOH solution. Next, 350 µL of 0.1 M $CdCl_2$ was added to the mixture and stirred for 5 min, after which 350 µL of 0.1 M Na_2S was injected. The reaction temperature was fixed to 35 °C, and the mixture was left to react for 3 h, after which the solution was purified using a 10 kDa centrifuge membrane to separate the NCs from the excess reactants. Based on the information gained, to obtain Cu-doped CdS NCs, it has been followed the same synthesis route described for undoped CdS, with the only exception being the addition of 1.05 mL of Cu_4 clusters (4×10^{-2} M water solution) to the reaction medium (stated in the above procedure) for obtaining Cu^{EX}:CdS (see below) and 0.150 mL of Cu_4 clusters (4×10^{-2} M water solution) for obtaining Cu:CdS^{EX} NCs (see below). After a 3 h reaction, the solution was purified and concentrated by passing through a 10 kDa centrifuge filter to completely remove the excess reactants and nonreacted Cu_4 clusters remaining in solution. The obtained CdS NCs were characterized with high-resolution transmission electron microscopy (HR-TEM), performed on a JEOL JEM-2200FS microscope equipped with a field emission gun working at an accelerating voltage of 200 kV, a CEOS spherical aberration corrector of the objective lens, allowing to reach a spatial resolution of 0.9 Å, and an in-column Omega filter. X-ray diffraction (XRD) and optical spectroscopies as discussed below (Figure 3.4). Figure 3.4a reports representative HR-TEM images of the undoped and Cu-doped NCs together the respective size histogram, which reveal similar size of the two NC ensembles, with average size of ~3.8 ± 0.5 nm and ~3.8 ± 0.3 for the undoped and doped systems, respectively. The XRD

patterns of both systems (Figure 3.4b) show the signature peaks of zincblende CdS,[225] indicating that the doping process does not alter the crystal structure of the NCs.

3.3 - Optical properties of undoped and Cu-doped CdS Nanocrystals

The optical absorption and photoluminescence (PL) spectra of the two material systems are reported in Figure2c, showing nearly identical absorption profiles (Figure 3.4c), with a well-defined 1S absorption peak at 400 nm, in good agreement with the expected energy gap of quantum confined ~4 nm particles observed by TEM. The absorption spectra were acquired with the same experimental setup described in Section 2.1, whereas the steady-state PL measurements were performed on a Cary Eclipse Varian fluorescence spectrophotometer at room temperature with a xenon lamp as a continuous wave light source. The full width at half-maximum of the 1S peak is ~0.26 eV and ~0.25 eV for the doped and undoped NCs respectively, confirming the good size homogeneity on the NC ensemble. Despite such

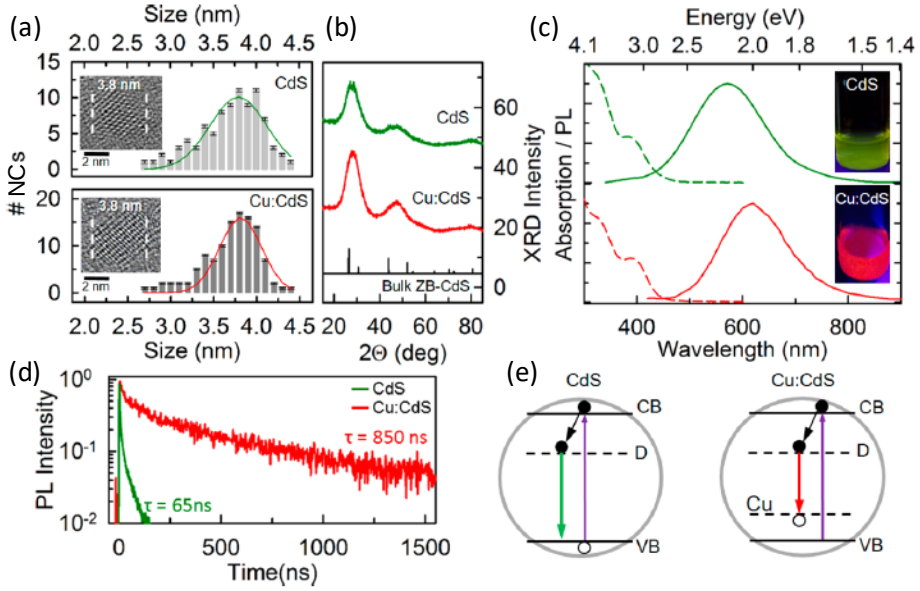

Figure 3.4 (a) Size distribution and high-resolution transmission electron microscopy (TEM) images of undoped and copper doped NCs, together with (b) the corresponding X-ray diffraction (XRD) patterns. The XRD pattern of bulk CdS in cubic zincblende structure is reported as reference (black line). (c) Normalized absorption (dashed lines) and PL (solid lines) profiles of undoped CdS (green) and Cu:CdS NCs (red) in water. The insets show a photograph of the NCs solutions under UV illumination. (d) Time resolved photoluminescence of undoped (green line) and Cu-doped CdS under 3.05 eV pulsed excitation (e) Schematic depiction of the recombination mechanism in undoped (left) and Cu:doped (right) NCs upon band-to-band excitation (blue arrows). The black arrows indicate the rapid localization of a conduction band (CB) electron in a localized state most likely associated with a surface defect (D). The recombination of the electron with a valence band (VB) hole in undoped NCs gives rise to the characteristic green defect luminescence (green arrow). The red arrow depicts the luminescence of doped NCs due to radiative decay of a photogenerated electron (represented as trapped in a surface state for consistency with the undoped NCs) in an intra-gap state associated to the Cu impurity.

similarities, undoped and Cu-doped NCs exhibit striking differences between their emission spectra and decay dynamics, deriving directly from the insertion of Cu atoms in the NC lattice.[194,215,218,226] Specifically, undoped NCs show a broad luminescence peak at ~580 nm, with characteristic lifetime of ~ 65 ns (Figure 3.4d), consistent with the trap-mediated green emission commonly observed in unshelled CdS NCs synthesized both in aqueous and organic media (left scheme in Figure 3.4e).[224,227-229] Time-resolved PL decays were recorded with an Edinburgh Instruments FLS 980 spectrofluorometer using a 405 nm EPL 405 (Edinburgh Inst.) as excitation source (pulse width 40 ps). The luminescence quantum efficiency of CdS NCs was determined by relative measurements in comparison with a 9,10-diphenylanthracene solution in deaerated tetrahydrofuran (10^{-6} M). In contrast, Cu-doped NCs show red luminescence at ~610 nm (Figure 3.4c) with decay time of ~850 ns (Figure 3.4d), which is over ten times longer than the undoped counterparts and is consistent with the radiative relaxation of photoexcited electrons -either delocalized in the NC conduction band or trapped in shallow defects, as schematized in Figure 3.4e for consistency with the trap-assisted decay of undoped sample- in the localized intragap acceptor level associated with the *d*-states of the Cu impurities (right scheme in Figure 3.4d).[215,218,230] I highlight that the PL features of doped NCs are markedly different from those of aggregated Cu_4 clusters (Figure 3.1b,c) both for their spectral position and decay dynamics, which excludes a possible contribution from aggregated clusters left in solution despite the thorough purification process and the unfavourable pH that leads to their dissolution in non-emissive isolated species. I also note that both doped and undoped NC samples show an initial fast decay component ascribed to surface trapping in surface defects, in agreement with the relatively low emission efficiency of both systems (Φ = 4.5 ± 0.4%) that present no additional protective shell. Further confirmation of the successful introduction of Cu atoms in the bulk of the NC and their key role in the photophysics of the doped NCs is obtained through side-by-side PL experiments in the presence and in the absence of a strong hole-withdrawing agent, such as 1-dodecanethiol (DDT), following the approach introduced by Viswanatha *et al.* for the investigation of the recombination mechanism in Cu-doped ZnSe/CdSe NCs.[194] Specifically, the addition of a Lewis base, such as DDT, has been shown to dramatically quench the luminescence of undoped NCs by ultrafast extraction of photoexcited holes prior to radiative exciton recombination.[194] On the other hand, copper ions introduce intragap *d* states close to the NC valence band that either behave as intrinsic hole-like states in the case of their

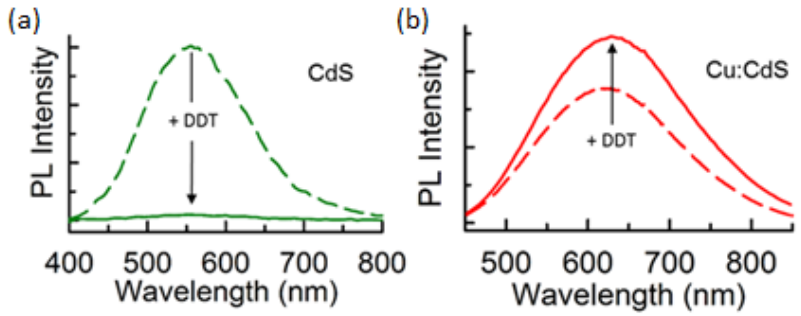

Figure 3.5 PL spectra of (a) CdS NCs and (b) Cu:CdS NCs before (dashed lines) and after addition (solid lines) of hole-accepting DDT (1-dodecanethiol) molecules.

substitutional incorporation as Cu^{2+} impurities (with d^9 electronic configuration),[194] or as efficient acceptors for photoexcited valence band holes when their oxidation state is +1 (corresponding to a filled d^{10} electronic shell).[218] In either situation, which most likely co-exist in copper-doped NCs,[194,217,218] exposure of Cu-doped NCs to electron rich moieties is inconsequential for the availability of hole-like states in the copper centres, leading to no luminescence quenching by nonradiative hole scavenging. On the other hand, the passivation effect by DDT of electron acceptor surface sites has been shown to significantly enhance the luminescence efficiency of Cu-doped NCs. Hence, the positive *vs*. negative PL response to the addition of DDT can be used to probe the presence of intragap copper states and, ultimately, to assess the successful incorporation of Cu impurities in the bulk of the semiconductor host. The data, reported in Figure 3.5, show nearly complete quenching of the luminescence of undoped NCs by efficient hole withdrawal by DDT and concomitant photobrightening of Cu:CdS NCs. This is in full agreement with the recombination mechanism of copper-doped NCs that involves the radiative relaxation of photoexcited electrons in impurity-related acceptor states,[215,218] which are unaffected by ultrafast hole scavengers and that benefit from the passivating effect of surface electron traps by electron donating moieties.[194] I finally stress that this behaviour is consistent with the response of previously reported Cu:NCs obtained through growth doping methods where the dopants are incorporated in the bulk of the host lattice.[194] In our case, the seeded growth approach ensures that the dopant ions are originally positioned in particle core and the low reaction temperature (35°C) makes lattice diffusion and ejection processes unlikely to occur, as it was demonstrated for nucleation-doped Cu:ZnSe NCs, which required temperatures above 210°C to activate self-purification mechanisms[181].

3.4 - Demonstration of Quantized Doping of Individual Nanocrystals

In order to quantitatively evaluate the doping level of individual NCs and to demonstrate that our approach yields uniform doping of the NC ensemble with the same number of dopant atoms per NC (corresponding to one Cu_4 cluster each), I performed side-by-side elemental analysis by ICP-AES and XRF spectroscopy on the undoped and copper-doped CdS NCs produced in the excess of Cu_4 (hereafter indicated as Cu^{EX}:CdS) presented in Figure 3.4 and on a second Cu-doped NCs sample I synthesized in the excess of NC precursors (Cu:CdS^{EX}). The ICP-MS instrument is a PerkinElmer ELAN DRC-e. The LA (laser ablation) sampler is a New Wave UP 213 working with a quintupled Tempest laser at 213 nm. The protocol used for this analysis is based on the PerkinElmer proprietary semiquantitative method TOTALQUANT based on the instrument internal standardization. For this analysis, the internal standardization has been improved by a single measure of NIST 610, a glassy multi-elemental solid standard. Nanoparticles are measured after deposition and drying on a silica substrate from the liquid solution. Laser pulse energy was tuned in order to ablate the sample deposit, leaving undamaged the silica substrate. Due to the sulphur interfering signal and possible sulphur compound contamination of this solution, the method is considered reliable for the metal content, and the sum of the measured metal levels represents by definition 100% of the metallic mass. As a general consideration, the absolute error for this elemental analysis protocol could be estimated in the range ±25% for the majority of the elements. This error is mainly related to the uncertainty in the NIST 610 standardization procedure, and it is due to the NIST 610

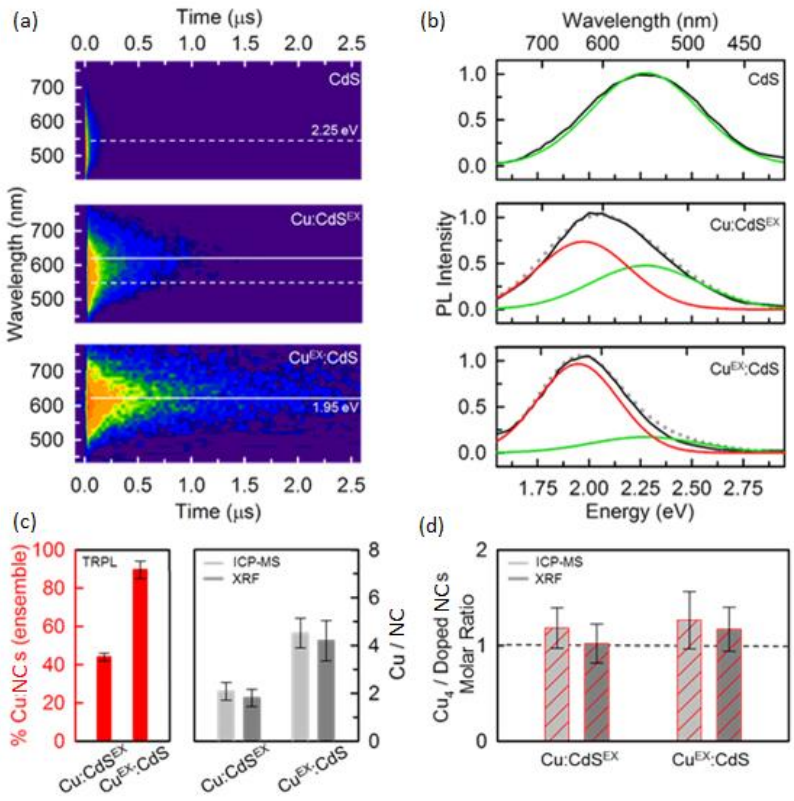

Figure 3.6 (a) Spectrally- and time- resolved PL of stirred solutions of undoped and doped CdS NCs synthesized in the excess of NC precursors (Cu:CdS^{EX}) or in the excess of Cu_4 clusters (Cu^{EX}:CdS) under 3.05 eV pulsed excitation. (b) Steady-state PL spectra of the same NCs as in 'a' (black lines) and their deconvolution using a global fit with two spectral components, respectively ascribed to the sub-population of doped NCs (red curve, obtained by time integrating the time-resolved emission profiles of Cu^{EX}:CdS in 'a' between 700-1500 ns) and undoped NCs (green curve, obtained by time integrating the time-resolved emission profiles of undoped NCs in 'a' between 0-50 ns). The global fit calculated as the sum of the two spectral components is shown as dotted grey curve. (c) Left panel: fraction of doped NCs in the Cu:CdS^{EX} and the Cu^{EX}:CdS ensembles extracted from the analysis of global fit of the time-resolved photoluminescence. Right panel: the average NC doping level estimated by ICP-MS and XRF spectroscopy. (d) Molar ratio between Cu_4 clusters and doped NC calculated by combining the spectroscopic and the elemental analysis data. The results highlight that in both the Cu:CdS^{EX} and the Cu^{EX}:CdS ensembles each doped CdS NC contains four copper atoms, which corresponds to one Cu_4 cluster per NCs.

composition uncertainty that has been estimated from the literature.[231] Due to the instrumental linearity range of 9 orders of magnitude and the stability, common for this kind of instrument, differently from an absolute measurement, the uncertainty of a relative measure between different samples showing the same matrix (if an internal standard is available for the signal normalization between samples) is reliable within a few points of the percent of error. Energy-dispersive XRF analysis was performed with a Bruker Artax 200 EDXRF spectrometer, equipped with an X-ray tube (Mo anode) with a beam collimated down to 0.65 mm in diameter. The induced characteristic X-ray fluorescence passes to a semiconductor detector, which works

according to the drift chamber principle (silicon drift detector). A Mo transmission filter (12.5 μm thick) was used. The working conditions were 30 kV and 0.9 mA with an acquisition time of 1800 s for each measurement. Bruker Spectra 5.1 software was used to perform peak deconvolution. Element concentrations were obtained using reference materials with a stoichiometric concentration of the analytes and using sulfur as an internal standard. Specifically, CdS bulk single crystals were used to determine stoichiometric sulfur counts with respect to cadmium counts in NCs. $CuInS_2$ was adopted as stoichiometric standard to evaluate the copper content with respect to the stoichiometric counts of sulfur in CdS NCs. I performed three measurements in different areas of the same sample on a series of seven different samples to check the homogeneity and to evaluate the standard errors.

In combination to the elemental analysis, I performed spectrally- and temporally-resolved PL measurements that allow us to quantify, through their characteristic spectroscopic signatures, the relative populations of undoped and doped particles within the NCs ensembles. By doing so for the Cu^{EX}:CdS NCs, I demonstrate that metal clusters effectively act as 'quantized' source for copper atoms and that a uniform population of doped NCs incorporating the equivalent of one cluster per dot can be easily synthesized at room temperature in water by operating in mild cluster excess conditions. Operating in excess of semiconductor precursors results instead in a bimodal distribution of two subpopulations of doped and undoped NCs. Importantly, the Cu-doped NCs obtained in the excess of NC precursors incorporate the atomic equivalent of one Cu_4 cluster per NC, similar to the Cu^{EX}:CdS NCs. Therefore, the co-presence of doped and undoped NCs is, in this case, not accidental, but it is direct consequence of the quantized doping approach, where the number of available metal clusters in the reaction medium strictly determines the relative population of undoped vs. homogenously doped NCs. Figure 3.6a reports the contour plots of the time resolved emission spectra of the undoped NC (top panel) in direct comparison with the two doped ensembles. In agreement with the data in Figure 3.4c,e, the PL of the undoped NCs is centred at 580 nm and the signal decays completely within the first 250 ns. In contrast, the Cu^{EX}:CdS NC (bottom panel) exhibit a much longer-lived emission at 610 nm, whose spectral position remains constant for over 2.5 μs, indicating that the solution is essentially a monodisperse population of doped particles. On the other hand, the Cu:CdS^{EX} NCs shows an intermediate behaviour between the two limiting cases, with a fast high-energy spectral contribution due to undoped NCs accompanied by a slower emission at lower energy arising from the subpopulation of copper-doped NCs.

In order to quantify the relative populations of doped and undoped particles in the three ensembles, I deconvolved the respective continuous wave luminescence spectra using the emission profiles of undoped and doped NCs (Figure 3.6b), respectively extracted by integrating the time-resolved emission spectra of the CdS NCs in the t=1-50 ns delay range and of the Cu^{EX}:CdS NCs for t = 700-1500 ns. The procedure, taking into account the comparable PL efficiency of undoped and doped particles (~4.5 ± 0.4%), yields a relative population of doped dots of ~45% in the Cu:CdS^{EX} NC ensemble and as high as ~95% for the Cu^{EX}:CdS NCs sample. This confirms that the Cu_4 clusters act as nucleation seeds for doped NCs and that the spontaneous nucleation of undoped CdS particles occurs only in the excess of semiconductor precursors, that is, when the available clusters are insufficient in number to seed the growth of

all CdS NCs. The quantitative elemental analysis by ICP-AES of the relative concentration of Cu and Cd atoms in the ensembles validates the original assumption that each NC contains one Cu_4 cluster, whose size determines the NC doping level. To demonstrate this aspect, I used the structural parameters provided by the TEM, XRD and optical absorption reported in Figure 3.4, to estimate the average number of Cd atoms per NC - in the approximation of spherical particles - and compared the outcome to the average number of Cu atoms in the two doped NC samples (Figure 3.6c). This procedure for the Cu^{EX}:CdS NCs yields an average doping level of 4.5 ± 0.6 copper ions per NC, which, together with the essentially complete doping of the ensemble highlighted by the spectroscopic analysis (95% of the total NC population), proves that each CdS NC contains the equivalent of one Cu_4 cluster (Figure 3.6d).

The same conclusion is obtained also for the Cu:CdS^{EX} NCs, for which the elemental analysis indicates a Cu/NC ratio of ~2.1 ± 0.4, that, once scaled for the 45% population of doped particles in the ensemble (Figure 3.6c), yields 4.4 ± 0.5 copper atoms per doped NC, corresponding to a molar ratio of one Cu_4 cluster per doped NC (Figure 3.6d).

Finally, to independently confirm the doping levels in the two NC ensembles extracted from the ICP-AES analysis, I performed elemental analysis by XRF spectroscopy on both NC samples. Consistently with the mass spectroscopy data, the XRF results indicate a Cu/NC ratio of ~4.2 ± 0.8 and ~1.8 ± 0.4 Cu^{EX}:CdS for and Cu:CdS^{EX} NCs, respectively (Figure 3.6c). Also in this case, by scaling the average doping level for the respective population of doped *vs*. undoped NCs in the ensembles, I obtain a molar ratio between Cu_4 cluster and doped NCs of 1.0 ± 0.2 and 1.1 ± 0.2 for Cu:CdS^{EX} and Cu^{EX}:CdS respectively (Figure 3.6d), thus demonstrating the effectiveness of the proposed doping concept.

3.5 - Conclusion

In summary, I demonstrated a strategy for controlling the doping level of NCs with atomic precision at the single particle level, capable of producing homogeneously doped NC ensembles in which each particle contains the same number of dopant atoms. This approach is based on the use of monodisperse colloidal metal particles acting as nucleation seeds for semiconductor NCs and providing a 'quantum' of dopant atoms determined by their 'magic size' that can be pre-tuned by suitable choice of the cluster synthesis conditions. This approach effectively combines two traditionally orthogonal nanomaterial systems and potentially opens the way to pre-tuned doping of other semiconductor materials with various types of doping metals or alloys for achieving highly controlled doped NCs with tailored optoelectronic and magnetic functionalities.

Chapter 4

Direct Measurements of Magnetic Polarons in $Cd_{1-x}Mn_xSe$ Nanocrystals from Resonant Photoluminescence

In semiconductors, quantum confinement can greatly enhance the interaction between band carriers (electrons and holes) and dopant atoms. One manifestation of this enhancement is the increased stability of exciton magnetic polarons in magnetically doped nanostructures. In the limit of very strong 0D confinement that is realized in colloidal semiconductor nanocrystals, a single exciton can exert an effective exchange field B_{ex} on the embedded magnetic dopants that exceeds several tesla. Here I use the very sensitive method of resonant photoluminescence to directly measure the presence and properties of exciton magnetic polarons in colloidal $Cd_{1-x}Mn_xSe$ nanocrystals. Despite small Mn^{2+} concentrations (x = 0.4–1.6%), large polaron binding energies up to ~26 meV are observed at low temperatures via the substantial Stokes shift between the pump laser and the resonant photoluminescence maximum, indicating nearly complete alignment of all Mn^{2+} spins by B_{ex}. Temperature and magnetic field-dependent studies reveal that $B_{ex} \approx 10$ T in these nanocrystals, in good agreement with theoretical estimates. Further, the emission line widths provide direct insight into the statistical fluctuations of the Mn^{2+} spins. These resonant PL studies provide detailed insight into collective magnetic phenomena, especially in lightly doped nanocrystals where conventional techniques such as non-resonant photoluminescence or time-resolved photoluminescence provide ambiguous results.

A particularly striking consequence of *sp–d* interactions in II–VI semiconductors is the formation of exciton magnetic polarons (EMPs), wherein the effective magnetic exchange field from a single photogenerated exciton -B_{ex}- induces the collective and spontaneous ferromagnetic alignment of the magnetic dopants within its wave function envelope, generating a net local magnetization even in the absence of any applied field.[232,233] In turn, these aligned local moments act back on the exciton's spin, which lowers the exciton's energy, further localizes the exciton, and further stabilizes the polaron. The stability and binding energy of EMPs therefore depends on the detailed interplay between many factors including the exciton lifetime, the polaron formation time, the exchange field B_{ex}, sample dimensionality, and temperature.

EMPs and collective magnetic phenomena have been experimentally studied in a variety of Mn^{2+}-doped semiconductor nanostructures, including CdMnSe and CdMnTe-based epilayers and quantum wells,[234-242] self-assembled CdMnSe and CdMnTe quantum dots grown by molecular beam epitaxy,[243-253] and most recently in CdMnSe NCs synthesized via colloidal techniques.[195,254] Common measurement techniques include the analysis of conventional

(i.e., non-resonant) photoluminescence (PL)[195,237,244,246,249,253,254] and time-resolved PL.[195,236,241,242,251,254]

However, an especially powerful and incisive experimental technique for directly revealing the presence and properties of magnetic polarons is the method of resonant PL.[234,235,238-241] In this experimental technique, a narrow-band excitation laser, tuned to the low-energy side of the exciton absorption peak, resonantly excites low-energy "cold" excitons. Subsequently, the exciton's exchange field B_{ex} aligns the Mn^{2+} spins and forms an EMP, which in turn lowers the exciton's energy. When the exciton recombines, it therefore emits a lower-energy photon. Thus, the Stokes shift between the pump laser energy and the emitted PL directly reveals the polaron binding energy. Temperature and magnetic field dependent measurements determine B_{ex} and therefore the strength of *sp–d* interactions in the material. Moreover, the resonant PL line width provides immediate insight into Mn^{2+} spin fluctuations. Resonant PL methods have been used to quantify EMP energies and spin fluctuations in Mn^{2+}-doped semiconductor epilayers[234,239] and quantum wells.[235,238,240] To date, however, this powerful technique has never been applied to study EMPs in colloidal NCs, even though they represent the strongest case of 0D quantum confinement, in which *sp–d* exchange is expected to be most enhanced.

To address this gap, I use resonant PL spectroscopy to directly reveal the presence and properties of EMPs in $Cd_{1-x}Mn_xSe$ colloidal NCs. Despite small Mn^{2+} concentrations (x = 0.4–1.6%), large EMP binding energies up to ~26 meV are observed at low temperatures,

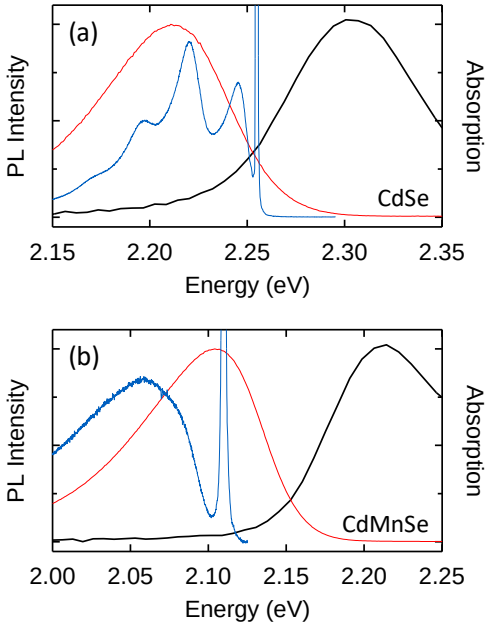

Figure 4.1 (a) Absorption (black), non-resonant PL (red), and resonant PL (blue) from a reference sample of nonmagnetic CdSe NCs at T = 1.8 K and B = 0 T. Under resonant (selective) excitation, the PL emission exhibits a series of sharp peaks that reveal exciton fine structure and LO–phonon replicas, in agreement with past studies. (b) Absorption, non-resonant PL, and resonant PL from the 1.6% CdMnSe NCs at 1.8 K and 0 T. In contrast to the nonmagnetic sample, resonant PL from these nanocrystals exhibits a large Stokes shift and is very broad, which provides a direct measure of the magnetic polaron binding energy and also the Mn^{2+} spin fluctuations, respectively.

indicating that within its radiative lifetime a photogenerated exciton completely aligns the Mn^{2+} spins within its host NC. The exchange field B_{ex} is found to lie in the range of 8−11 T, in good agreement with theoretical expectations for these NCs. Finally, the significant variations of the resonant PL line width are confirmed by numerical Monte Carlo simulations, providing direct insight into Mn^{2+} spin fluctuations. These studies highlight the utility of resonant PL as an effective tool for detailed studies of collective magnetic phenomena in colloidal nanomaterials.

Several batches of $Cd_{1-x}Mn_xSe$ NCs were grown by colloidal synthesis. CdSe NCs in wurtzite structure were synthesized with the same procedure of the CdSe core for W/W-NCs in Chapter 2 (Section 2.1).[105] Before Mn^{2+} doping, the octadecylphosphonic acid ligands were partially replaced with oleic acid. The preparation of lightly-doped $Cd_{1-x}Mn_xSe$ NCs were prepared by drying a ~0.13 mmol CdSe NCs that have been added to 0.17 g (2.1 mmol) of Se powder, 1 mL of 1-octadecene, and 1 mL of tributylphosphine in a septum-capped 5 mL round-bottom flask in a nitrogen-atmosphere glovebox. Separately, 12 g of 1-octadecene, 0.5 g of stearic acid, and 1 g of hexadecylamine were added to a 100 mL three-neck round-bottom flask. Following heating of the latter solution for 30 min at 100 °C under vacuum, 0.03 g (0.1 mmol) of $Mn(OAc)_2{\cdot}4H_2O$ was added against a nitrogen overpressure. The flask was then placed under vacuum to remove acetic acid and water and then heated under nitrogen to 300 °C, at which point the CdSe/selenide solution was injected rapidly. This reaction mixture was held at temperatures between 290 and 300 °C for between a few seconds and 29 h. The reaction is aided by the greater activity of tributylphosphine than the more common trioctylphosphine. As the solution was cooled to room temperature, 3 mL of toluene was added at ~120 °C to prevent stearic acid solidification.

As described in Section 1.3, the NCs were grown sufficiently large (5 nm average diameter) so that the 1S exciton energy lies below the $^4T_1 \rightarrow {}^6A_1$ transition energy of the Mn^{2+} ions. This results in long exciton recombination lifetimes exceeding 10 ns, which is much longer than typical sub-nanosecond polaron formation times.[236,241,242,251,254] Polaron formation is therefore not interrupted by exciton recombination and proceeds to an equilibrium condition. The Mn^{2+} concentrations (0.4%, 0.7%, and 1.6%, which correspond to $\langle N \rangle \approx 5$, 9, and 20 Mn^{2+}/NC) were intentionally kept low to minimize Mn^{2+} clustering effects. Reference samples of nonmagnetic CdSe NCs were also synthesized. The NCs were dispersed in optical-quality polyvinylpyrrolidone films to minimize scattering.

Here, I focus on resonant PL techniques to explicitly detect the presence and properties of EMPs. Therefore, I tuned a continuous-wave dye laser to the low-energy side of the inhomogeneously broadened 1S exciton absorption peak. This selectively pumps excitons into the subset of NCs whose optically allowed ("bright" exciton) absorption energy is exactly resonant with the laser, thereby mitigating the effects of ensemble broadening. Subsequently, these excitons can lower their energy by relaxing to "dark" states within the exciton fine structure[19,23] or also -in Mn^{2+}-doped NCs- by forming an EMP. The key point is that the resonant Stokes shift ΔE between the pump laser and the emitted PL therefore reveals the difference between the exciton's initial energy (i.e., at absorption) and final energy (i.e., at recombination). Resonant PL is closely related to fluorescence line narrowing methods that have been used to observe the bright-dark splitting (fine structure) of excitons in conventional undoped NCs.[19,23]

4.1 – Optical Properties

Optical-quality films exhibiting minimal scattering were essential for these resonant PL experiments. Typically, 2% weight-to-weight (w/w) polyvinylpyrrolidone in $CHCl_3$ was mixed with a 4 mL nanocrystal/$CHCl_3$ solution. After centrifuging this mixture, the pellet was then re-dissolved in 600 μL of 1% PVP in 20% w/w butanol/chloroform. Drops of this reformed mixture were spread onto glass cover slips and then spun at 500 rpm for 120 seconds followed by an additional 60 seconds at 2000 rpm. This procedure produced thick (~20 μm) homogenous nanocrystal films.[255]

All measurements were performed with the samples mounted in the variable-temperature insert of a 7 T magneto-optical cryostat. Magnetic fields were applied normal to the NC film and parallel to the direction of optical excitation/detection (i.e., the Faraday geometry). For resonant PL studies, a low-power continuous-wave dye laser with a narrow linewidth (~40 GHz) was tuned to the far red (low-energy) side of the 1S exciton absorption resonance in order to excite only a narrow distribution of the lowest-energy 1S excitons in the ensemble and to avoid effects due to energy transfer or photon re-absorption. The resonant PL was detected by a 500 mm spectrometer and a liquid nitrogen cooled CCD. For all the data shown, I pumped and detected circularly polarized light. No evidence of optical orientation of magnetic polarons was ever observed, likely due to the random nanocrystal orientation

To establish a reference against which to compare the Mn^{2+}-doped NCs, I first show in Figure 4.1a the characteristic absorption, non-resonant PL, and resonant PL spectra from an ensemble of conventional nonmagnetic CdSe NCs at low temperature (T = 1.8 K) and at B = 0. The 1S exciton absorption peak (black trace) is well-defined and ~70 meV wide, indicating a typical degree of inhomogeneous broadening due to the NCs' size distribution. The non-resonant PL (red trace) is similarly broad and is shifted to lower energies, as expected. The resonant PL spectrum (blue trace) exhibits a series of sharper peaks that are Stokes-shifted from the pump laser and is also quite typical.[19,23,43] Here, the energy difference ΔE between the laser and the closest emission peak (~6 meV in this sample) directly reveals the exciton's fine structure -i.e., the energy splitting Δ_{bd} between the "bright" (angular momentum projection J = ±1) and lower-energy "dark" (J = ±2) exciton states that is due to electron–hole exchange (Section 1.1). The additional peaks at lower energies are optical phonon replicas of the dark state.

In comparison, Figure 4.1b shows the same three spectra measured on the 1.6% CdMnSe NCs. The broad absorption and non-resonant PL spectra are dominated by the inhomogeneous size distribution and are essentially indistinguishable from those of the nonmagnetic reference sample (the overall shift in absorption/PL energy is because the nonmagnetic NCs in Figure 4.1a have smaller average diameter). Crucially, however, the resonant PL spectrum is completely different. Instead of a series of sharp emission peaks, the resonant PL at B = 0 exhibits a much larger Stokes shift ΔE and is broad and featureless. This indicates (i) that excitons in these magnetically doped NCs lower their energy much more during their lifetime as compared to nonmagnetic NCs and (ii) that the distribution of Stokes shifts is much broader. Both these properties are consistent with the presence of Mn^{2+} spins and the formation of EMPs.

4.2 – Magnetic Field Dependence of Resonant Photoluminescence

The most unambiguous evidence for EMP formation in these CdMnSe NCs is obtained via the dramatic evolution of the resonant PL spectra in applied magnetic fields. As shown in Figure 4.2a for the 1.6% CdMnSe sample, the initially broad and featureless resonant PL spectrum at 0 T evolves continuously into a series of narrow emission peaks at 7 T. The Stokes shift ΔE between the laser and the closest emission peak decreases from ~30 meV to ~5 meV. Importantly, at 7 T the resonant PL spectrum now closely resembles that which was obtained from the nonmagnetic CdSe NCs (see Figure 4.1a), namely, a narrow emission peak at small ΔE followed by a series of optical phonon replicas. Measurements of the 0.7% and 0.4% CdMnSe NCs show similar evolution with the field, but with smaller ΔE at B = 0 (Figure 4.2b,c). In marked contrast, all the nonmagnetic CdSe NCs show very little change in the resonant PL energy and width up to 7 T (Figure 4.2d), in agreement with prior studies.[23,43]

These two trends in the resonant PL -namely, the drop in both ΔE and the line width as B is increased- are telltale hallmarks of EMPs that have been previously observed in higher-dimensional and rather heavily Mn-doped diluted magnetic semiconductors such as

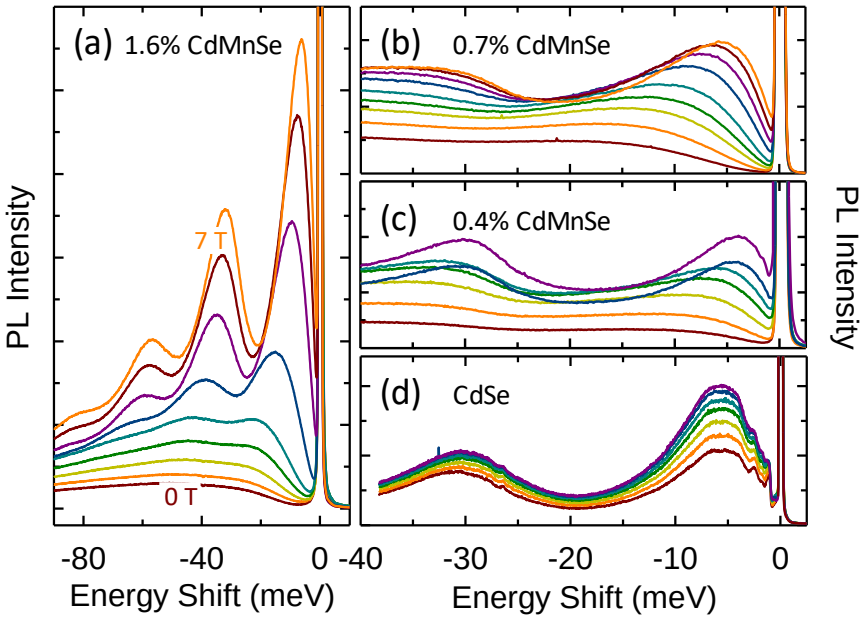

Figure 4.2 (a) Magnetic field dependent resonant PL spectra from the 1.6% CdMnSe NCs at 1.8 K. With increasing field B from 0 → 7 T (applied in the Faraday geometry), the resonant emission sharpens dramatically and evolves into a narrow peak (and its optical phonon replicas), while the Stokes shift between the excitation laser and the first emission peak is markedly reduced. Respectively, these indicate a suppression of Mn^{2+} spin fluctuations and a reduction of the magnetic polaron binding energy (because the Mn^{2+} are already initially aligned by B and further alignment by the exciton is not possible). Resonant PL spectra versus B at 1.8 K for the (b) 0.7% CdMnSe, (c) 0.4% CdMnSe, and (d) nonmagnetic CdSe NCs. As the Mn^{2+} concentration decreases, the zero-field Stokes shift and the line width both decrease (because both the polaron binding energy and Mn^{2+} spin fluctuations decrease). However, by 7 T the resonant PL spectra from the CdMnSe NCs closely resembles the resonant PL from the nonmagnetic CdSe NCs.

CdMnTe-based epilayers and quantum wells with x > 10%.[235,238-240] These trends, now clearly observed here in lightly doped but strongly confined 0D NCs, are due to the decrease of the EMP binding energy and also the decrease of Mn^{2+} spin fluctuations, by the applied field B. At B = 0 the excitons are initially photoinjected into NCs having a randomly oriented distribution of Mn^{2+} spins (the average Mn^{2+} spin polarization in the ensemble is zero). Subsequently, the excitons lower their energy by forming a magnetic polaron and eventually recombine from a lower-energy final state in which the Mn^{2+} spins are aligned (note this occurs independent of the NCs' orientation). In these ensemble measurements, this results in a large average Stokes shift ΔE at B = 0. Moreover, because of the initially random orientation of the Mn^{2+} spins, and also because the exact number and location of the Mn^{2+} spins within each NC varies, the energy lost by each exciton is different. This gives a broad distribution of measured Stokes shifts and correspondingly broad resonant PL features at B = 0 T.

In contrast, at B = 7 T (and at low temperatures), each exciton is initially photoinjected into a NC wherein all the paramagnetic Mn^{2+} spins are already aligned by B. The exciton cannot further align the Mn^{2+}, and so the final energy of the exciton is approximately the same as its initial energy. The net result is a small resonant Stokes shift ΔE that is expected to be like that from nonmagnetic NCs, as observed. Moreover, because the Mn^{2+} within each NC are aligned in both the initial and final states (again, independent of the NCs' orientation), there is no additional broadening from stochastic spin fluctuations. The resonant PL features are expected to be comparably narrow to those obtained from nonmagnetic NCs, again precisely as observed (e.g., compare Figure 4.2a and Figure 4.1a).

To better quantify the average Stokes shift ΔE and also the line width Γ of the resonant PL features, I fit all the resonant PL spectra from all the NCs to a series of Gaussian peaks. The results are shown in Figure 4.3a,b. I note that these values do not depend on the exact photon energy of the resonant pump laser, as long as it is tuned well below the 1S exciton. At B = 0, ΔE is largest for the 1.6% CdMnSe NCs (~31 meV), and is smaller for the more lightly doped samples (~17 meV for the 0.7% NCs and ~10 meV for the 0.4% NCs). Crucially, however, for all of the Mn^{2+}-doped NCs, ΔE falls monotonically as B → 7 T and converges toward a common value of ~5 meV at large B.

Interestingly, 5 meV is very close to the field-independent value of ΔE that is observed in nonmagnetic NCs of the same size (black points), which in turn is due to electron−hole exchange and the splitting Δ_{bd} between bright and dark excitons,[19] as discussed above. However, the presence of a similar 5 meV offset exhibited by ΔE in the CdMnSe NCs is somewhat unexpected, because the exciton ground state in conventional Mn^{2+}-doped II−VI semiconductors is typically bright at large B (this is because the *s*–*d* electron-Mn^{2+} exchange energy -the energy required to flip the electron spin- typically greatly exceeds Δ_{bd}).[138] Our resonant PL data are nonetheless consistent with a lower-lying and/or dark exciton ground state in these CdMnSe NCs at large B, whose origin is unclear but which could result, e.g., from slow EMP reorientation[254] or from a

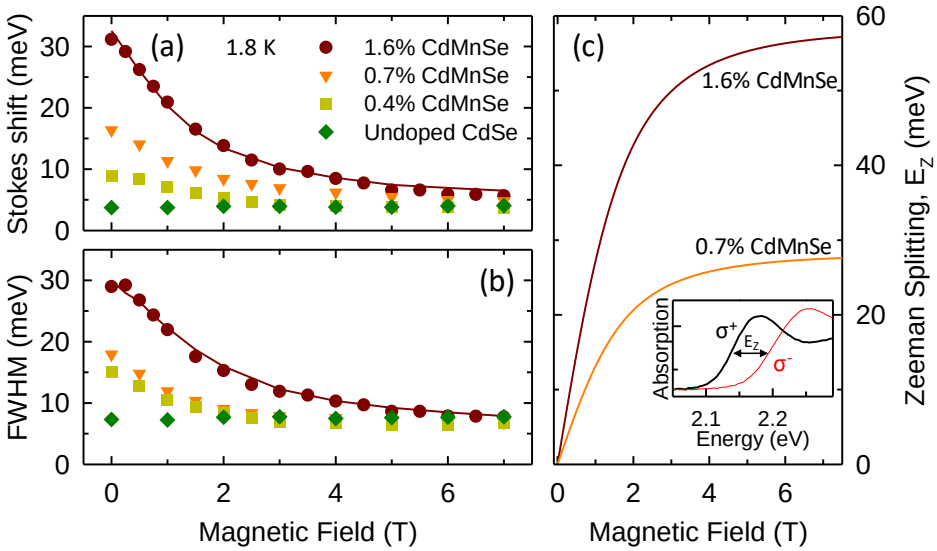

Figure 4.3 (a,b) Measured Stokes shift and full width at half maximum (FWHM) of the resonant PL peaks, for all samples at 1.8 K. At B = 0, they are largest in the most heavily doped NCs and decrease as B → 7 T, converging toward the value observed in the nonmagnetic CdSe NCs. This indicates a suppression of EMP binding energy and reduction of Mn^{2+} spin fluctuations, respectively. The solid lines show calculated Stokes shift and FWHM for the 1.6% CdMnSe NCs, from Monte Carlo simulations. (c) Brillouin functions corresponding to the measured total Zeeman splitting E_Z of the 1S exciton absorption peak in the 1.6% and 0.7% CdMnSe NCs at 3 K (see Eq. (1.16)). E_Z was measured by circularly polarized absorption; the inset shows example spectra at B = 6 T and T = 3 K. E_Z saturates at $E_{sp\text{-}d}$ = 58 and 28 meV, respectively, in these samples. The polaron binding energy can be directly compared with $E_Z/2$ to determine the degree of Mn^{2+} spin alignment due to EMP formation.

confinement-induced reduction/inversion of the *s–d* exchange interaction (a scenario recently explored in quantum-confined semiconductors[196,199,256,257]). Regardless, the essential observation and key point is that ΔE clearly converges to a constant value of ~5 meV at large B. I therefore associate the EMP binding energy (i.e., the energy that is lost by the exciton at B = 0 due explicitly to EMP formation) with ΔE − 5 meV ≡ 26, 12, and 5 meV for the 1.6%, 0.7%, and 0.4% CdMnSe NCs, respectively.

Similar to the Stokes shifts, the resonant PL line widths Γ are, at B = 0, largest for the 1.6% CdMnSe NCs and smaller for the 0.7% and 0.4% samples (see Figure 4.3b). As B → 7 T, all the line widths decrease and converge toward a common value of ~8 meV, which is again very close to the line width observed in the nonmagnetic CdSe NCs. This trend indicates a narrowing distribution of Stokes shifts in the ensemble, due to a suppression of spin fluctuations as the Mn^{2+} spins are forced to align by B. Note this behavior is also in agreement with the fluctuation–dissipation theorem, which mandates that magnetization (spin) fluctuations scale with χ, the magnetic susceptibility: $\langle M^2 \rangle / k_B T \propto \chi$. For paramagnetic ions, $\chi = \partial M / \partial B$ is simply the slope of the Brillouin function (discussed in Section 1.3, Eq. (1.17)) and therefore χ → 0 as B → ∞. However, I emphasize that the measured line widths are surprisingly large at zero field -comparable to ΔE itself. Given that ΔE should scale approximately as N (the average number of Mn^{2+} per NC), then the broad line widths at B = 0 are in contrast with simple expectations

that Γ should scale as $\sqrt{N}$. Furthermore, the resonant PL peaks are slightly asymmetric -the distribution's tail is longer on the low-energy side (most clearly seen at large B, where the phonon replicas do not overlap). Again, this contrasts with the expectation of symmetric distributions that derives from stochastic (Gaussian) $\sqrt{N}$ fluctuations alone. As discussed below, the unexpectedly broad widths and asymmetric lineshapes are due to the statistics of the overlap of randomly placed Mn^{2+} ions with $\psi_h(r)$, the hole's spatially nonuniform envelope wave function in the NC. To estimate B_{ex} and the degree of Mn^{2+} spin alignment due to EMP formation, I must compare the measured polaron binding energy (ΔE − 5 meV) to the giant Zeeman splitting of the 1S exciton absorption that occurs when the Mn^{2+} spins are intentionally aligned by applied fields B. Figure 4.3c shows the total Zeeman splitting, E_Z, for the 1.6% and 0.7% CdMnSe NCs as determined from polarized absorption spectroscopy (the inset shows the right- and left-circularly polarized absorption spectra of the 1S exciton at 6 T and 3 K).

As expected for Mn^{2+}-doped NCs,[199,258,259] E_Z is very large and follows the modified Brillouin form discussed in Section 1.3. By fitting the experimental results with Eq. (1.16), I obtain an intrinsic *g*-factor of excitons in CdSe NCs in agreement with previous reports ($|g_x| \simeq 1.4$)[217], that makes this term very small (~0.5 meV at 6 T) and therefore can be ignored. The second term, that considers the additional exciton splitting due to *sp*–*d* exchange interactions with the Mn^{2+} ions, gives a Mn^{2+}-ion *g*-factor, $g_{Mn} = 2$. The saturated magnitude of this second term, $E_{sp\text{-}d}$, is sample-specific and depends on the net overlap of $|\psi_{e,h}(r)|^2$, the probability density of the carrier envelope wave functions, with the embedded Mn^{2+} ions. In bulk diluted magnetic semiconductors, $E_{sp\text{-}d}$ is typically given within the mean-field and virtual crystal approximation as $E_{sp\text{-}d} = xS_{eff}(N_0\alpha - N_0\beta)$, where x is the Mn concentration, S_{eff} is the effective Mn^{2+} spin (≈ 5/2 for small x), and $N_0\alpha$ and $N_0\beta$ are the exchange constants characterizing the *s*–*d* and *p*–*d* interactions for electrons and holes, respectively.

In large B where the Mn^{2+} spins are completely aligned, I find that E_Z saturates at $E_{sp\text{-}d} \approx 28$ and 58 meV in the 0.7% and 1.6% CdMnSe NCs, respectively. Therefore, if an exciton at B = 0 forms an EMP and completely aligns all of the Mn^{2+} spins within its wave function envelope, then these aligned spins acting back on the exciton will lower its energy by $E_{sp\text{-}d}/2$ on average. Comparing the EMP binding energy with $E_{sp\text{-}d}/2$ therefore provides a means to roughly estimate both the degree of Mn^{2+} spin alignment due to EMP formation and also the exchange field B_{ex} that the exciton exerts on the Mn^{2+} spins.

In the 0.7% CdMnSe NCs, the measured EMP binding energy of 12 meV at 1.8 K is close to $E_{sp\text{-}d}/2$ (= 14 meV), indicating that the Mn^{2+} ions in these NCs are nearly completely aligned by EMP formation at B = 0. Similarly, the 26 meV EMP binding energy measured in the 1.6% CdMnSe NCs is close to $E_{sp\text{-}d}/2$ = 29 meV, again indicating nearly complete alignment of the Mn^{2+} ions due to EMP formation at 1.8 K. In principle, the exchange field B_{ex} can be equated with the magnetic field required to achieve this degree of alignment. In practice, however, such estimates are accurate only when the degree of Mn alignment is modest and the polaron binding energy is much less than $E_{sp\text{-}d}/2$. Here at 1.8 K, when the EMP binding energy approaches its maximum value of $E_{sp\text{-}d}/2$ and the Mn alignment saturates, estimates of B_{ex} become very sensitive to any small systematic offsets, and I can infer only that B_{ex} is large, at least of order several tesla but possibly much larger.

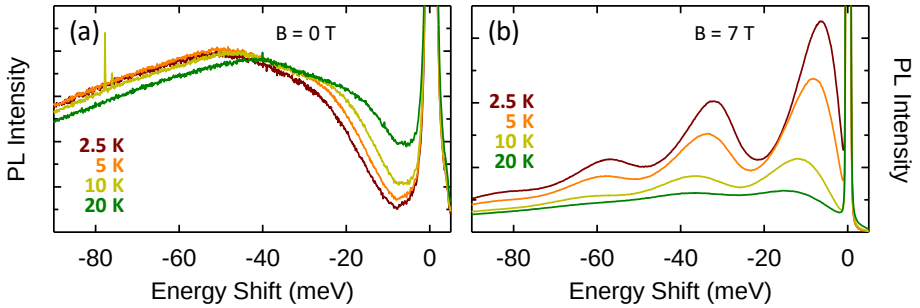

Figure 4.4 (a) Temperature-dependent resonant PL spectra from the 1.6% CdMnSe NCs at B = 0 T. (b) Same, but at B = 7 T. Note that the spectra shift in the opposite direction (see text).

4.3 – Temperature Dependence of Resonant Photoluminescence

Temperature-dependent studies provide a more accurate estimate of B_{ex}. Figure 4.4a shows resonant PL spectra from the 1.6% CdMnSe NCs from 2.5 to 20 K, at B = 0. In qualitative agreement with prior studies of CdMnTe/CdMgTe superlattices,[239] the resonant Stokes shift ΔE decreases as temperature increases. This indicates a reduction of the EMP binding energy, because the Brillouin-like magnetization of the Mn^{2+} spins, $\langle S_Z \rangle$, no longer saturates in the exchange field B_{ex} at elevated temperatures (put differently, the Mn^{2+} susceptibility decreases as temperature rises). This can also be understood by explicitly considering the difference between final and initial exciton energies given by the B- and T-dependent Zeeman energy from Eq. (1.16): the quantity $\Delta E \approx [E_Z(B = B_{ex}) - E_Z(B = 0)]/2$ decreases as temperature rises.

Similarly, Figure 4.4b shows temperature-dependent resonant PL spectra at B = 7 T. In contrast to the zero-field case, here ΔE increases with increasing temperature. This can also be understood by considering final and initial exciton energies: the quantity $\Delta E \approx [E_Z(B = 7\,T + B_{ex}) - E_Z(B = 7\,T)]/2$ is small at low temperatures (the Mn^{2+} spins are already initially saturated, and the additional B_{ex} has little effect) but increases as temperature rises (the Mn^{2+} are no longer initially saturated and can be further aligned by B_{ex}).

Figure 4.5 compares the measured ΔE (points) with expectations from the Brillouin function (lines) for both cases. The best agreement is found using $B_{ex} \approx 8$ T for the case of zero applied field, and, in reasonable concurrence, $B_{ex} \approx 11$ T when B = 7 T. Thus, I conclude that B_{ex} lies in the range of 8–11 T for the 1.6% CdMnSe NCs. Similar values of B_{ex} are obtained for the other samples. This large value of the exchange field B_{ex} exceeds typical values observed in epitaxially grown and lightly doped superlattices and quantum dots (~3 T),[232,244] but agrees rather well with straightforward theoretical estimates of B_{ex} for colloidal NCs of this size, as discussed immediately below.

First, I adopt the common assumption that B_{ex} derives entirely from the spin of the hole, and neglect the influence of the electron spin.[232,249] This assumption is justified because the *p–d* exchange constant $|N_0\beta|$ significantly exceeds the *s–d* exchange constant $|N_0\alpha|$: in bulk CdMnSe, $|N_0\beta| = 1.27$ eV while $|N_0\alpha| = 0.23$ eV. Moreover, $N_0\alpha$ is likely even further reduced in colloidal nanostructures due to quantum confinement effects.[199,256,257,260] Next, I recall that B_{ex} is actually

position-dependent within a NC and scales with the probability amplitude of the hole's envelope wave function:[232]

$$B_{ex}(\boldsymbol{r}) = \frac{1}{3\mu_B g_{Mn}} \beta J |\psi_h(\boldsymbol{r})|^2 \tag{4.1}$$

where J = 3/2 is the hole spin. To simplify Eq. (4.1), I use the popular "exchange box" model[232,246] wherein $|\psi_h(\mathbf{r})|^2$ and therefore $B_{ex}(\mathbf{r})$ are taken to be constant within an effective hole localization volume V and zero everywhere else. In this model, all Mn^{2+} ions within V interact equally strongly with the hole. I then obtain the following relationship between B_{ex}, the *p–d* exchange constant, and polaron volume

$$B_{ex} = \frac{|N_0\beta|}{2\mu_B g_{Mn}} \frac{1}{N_0 V} \tag{4.2}$$

where N_0 is the number of cations per unit volume ($N_0 \approx 18.0$/ nm^3 for CdSe). B_{ex} is therefore very sensitive to V, which can be significantly less than the physical volume of the NC because $\psi_h(\mathbf{r})$ approaches zero toward the NC surface. In general, V can be defined[232,234] as $V \equiv (\int |\psi_h(\boldsymbol{r})|^4 d^3\boldsymbol{r})^{-1}$. If the NCs are modeled as infinite spherical potential wells with radius a, then the 1S carrier envelope wave functions have functional form $\psi(\mathbf{r}) \propto \mathrm{sinc}(\pi r/a)$, and V is only ~36% of the total NC volume [here, sinc(x) = sin(x)/x]. Our NCs have 5 nm average diameter, from which I estimate within this "box" approximation that $B_{ex} \approx 13$ T, which is in reasonable agreement with the values of 8–11 T that were experimentally determined from resonant PL as shown in Figure 4.5. Variations in the exact spatial extent and functional form of $\psi_h(r)$ will also influence V and therefore B_{ex}.

Per Eq. (4.2), B_{ex} scales inversely with NC volume, and therefore small changes in NC diameter will significantly influence B_{ex}. However, the measured resonant Stokes shift depends only on $E_{sp\text{-}d}$ (assuming complete EMP formation) and therefore only on the effective Mn concentration in the NC (see Eq. (1.15)) and is therefore in principle independent of NC size.

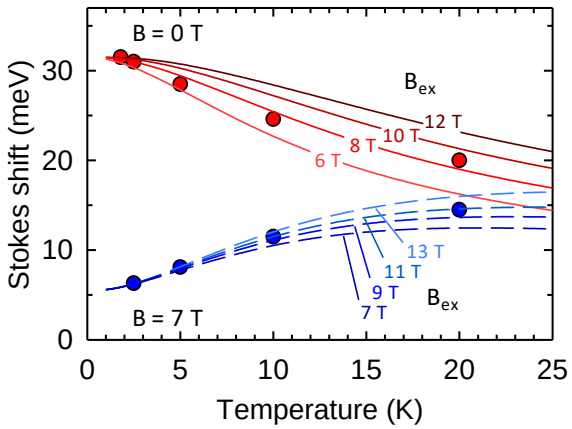

Figure 4.5 Comparing the measured resonant Stokes shifts (points) with calculations based on the known field- and temperature-dependent exciton Zeeman splitting for these NCs (the experimentally observed 5 meV offset has been added to the calculations). Reasonable agreement with the data at 0 and 7 T are found using an exchange field B_{ex} = 8 and 11 T, respectively.

It is worth noting that some earlier studies have analyzed the temperature dependence of conventional (non-resonant) PL to infer the properties of EMPs. For example, in ref. [195], very large values of B_{ex} in the range of 75–120 T were inferred in CdMnSe NCs with 4.3–5.0 nm diameters. However, analysis of EMP properties based on conventional PL/absorption spectroscopy may therefore also be influenced by effects due to inhomogeneous broadening in the ensemble and/or temperature-dependent energy relaxation within the broad manifold of states that comprise the exciton fine structure.[19] Both effects are significantly mitigated in resonant PL studies.

4.4 – Monte Carlo Simulations

Finally, to quantitatively interpret the unexpectedly large line widths and the asymmetry of the resonant PL peaks that have been observed experimentally, I report a model of these resonant PL spectra using a simple numerical Monte Carlo method. These simulations account for the

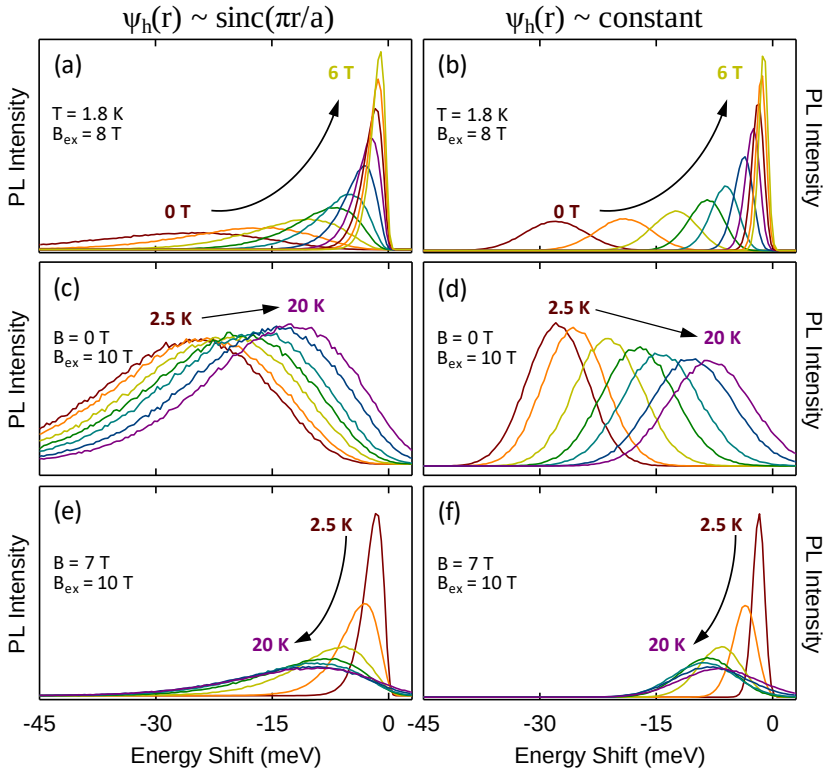

Figure 4.6 Numerical Monte Carlo simulations of the resonant PL spectra. For clarity, optical phonon replicas are not included. Here, ⟨N⟩ = 20 (corresponding to the 1.6% CdMnSe NCs). Spectra are calculated using both $\psi_h(r) \propto \mathrm{sinc}(\pi r/a)$ and $\psi_h(r)$ = constant (left and right panels, respectively). The additional 5 meV offset of the resonant Stokes shift that is observed experimentally is not included in these simulations. (a,b) Calculated spectra at T = 1.8 K for increasing applied field B (compare with experimental data in Figure 4.2). Calculated spectra at (c,d) B = 0 and (e,f) B = 7 T for increasing temperature (compare with data in Figure 4.4a,b). The broader line widths and asymmetric line shapes are accurately reproduced when using a realistic functional form of $\psi_h(r)$ but are not reproduced within a simple "box" model where $\psi_h(r)$ is constant.

effects of fluctuating Mn^{2+} spins and their random spatial distribution within the NCs. For each NC, N random locations within a unit sphere are first generated for the Mn^{2+} ions. ⟨N⟩ ranged from 5 to 20, corresponding to our 0.4%, 0.7% and 1.6% CdMnSe NCs, with an appropriate Poisson distribution. A random spin orientation is then generated for each Mn^{2+} ion, weighted by the appropriate distribution for the given temperature and applied field. The initial energy of the exciton is calculated by summing over the individual exchange energies from each Mn^{2+} ion, weighted by the probability amplitude of the properly normalized hole wavefunction $|\psi_h(r)|^2$. Then, to account for polaron formation, each of the same N Mn^{2+} ions is assigned new random spin orientation drawn from a new distribution that corresponds to the total magnetic field $B + B_{ex}(r) = B + B_{ex}|\psi_h(r)|^2$. Note that this procedure adopts the simplification that B and B_{ex} are parallel and can be added as scalars; in actuality B and B_{ex} may not be strictly parallel. The final exciton energy is again obtained via the sum over the individual exchange energies from each Mn^{2+} ion, weighted by $|\psi_h(r)|^2$. The Stokes shift ΔE is given by the difference between initial and final exciton energies, and the distribution of ΔE is obtained by repeating the simulation hundreds of thousands of times. A related Monte Carlo approach was described in Ref.[234] to simulate bound magnetic polarons in a very dilute regime in bulk CdMnTe.

Figure 4.6 shows calculated resonant PL spectra with increasing field and temperature. Phonon replicas are ignored for clarity. The pronounced shift and narrowing of the spectra with increasing applied field B are captured very well (e.g., compare Figure 4.6a,b with the field-dependent experimental data shown in Figure 4.2). Similarly, the temperature-dependent decrease and increase of ΔE at B = 0 and B = 7 T, respectively, are also modeled accurately (e.g., compare Figure 4.5c-f with the temperature-dependent data shown in Figure 4.4a,b).

Importantly, these simulations allow us to study how the line widths and the detailed lineshapes of the resonant PL features depend on the exact functional form of the hole wave function $\psi_h(\mathbf{r})$. For example, Figure 4.6 shows results for both the simplest "box" model wherein $\psi_h(\mathbf{r})$ is constant throughout the entire NC (panels b,d and f), and also for the more realistic scenario where $\psi_h(\mathbf{r}) \propto \mathrm{sinc}(\pi r/a)$ (panels a,c and e). When $\psi_h(\mathbf{r})$ is constant, the calculated resonant PL spectra are relatively narrow and symmetric, as expected because all Mn^{2+} spins interact equally strongly with the hole. In this case the random spatial distribution of Mn^{2+} within the NCs is irrelevant: at B = 0, the resonant Stokes shift is determined by N, and the line width is determined by the $\sqrt{N}$ spin fluctuations alone.

In contrast, both the much larger line width as well as the asymmetric line shape of the resonant PL peaks are more accurately captured when using $\psi_h(\mathbf{r}) \propto \mathrm{sinc}(\pi r/a)$. This is because the random spatial distribution of the Mn^{2+} ions now matters: different NCs having the same number of randomly placed Mn^{2+} ions can exhibit very different Stokes shifts depending on whether the Mn are statistically located closer to or further from the centre of the NC. Mn^{2+} spins located near the NC centre where $|\psi_h(\mathbf{r})|^2$ is large are less probable, but significantly impact the exciton energy. These effects further broaden the measured line width and cause the asymmetric line shape. For direct comparison with experimental data, results from these Monte Carlo simulations are shown for the 1.6% CdMnSe NCs by the solid red lines in

Figure 4.3a,b. When the field- and temperature-independent offsets for both ΔE and Γ are included, quite good agreement with the experimental data is obtained.

4.5 - Conclusion

In summary, resonant PL is demonstrated to be a powerful technique for studying magnetic polarons in magnetically doped colloidal NCs. Via a systematic analysis of the Stokes shifts and line widths of resonant PL spectra, the binding energies of EMPs and Mn^{2+} spin fluctuation properties are directly measured as a function of temperature, applied magnetic field, and magnetic doping concentration. In these strongly quantum confined CdMnSe NCs, the exchange field B_{ex} that is "seen" by the Mn^{2+} due to an exciton is determined to be approximately 10 T, in very reasonable agreement with theoretical expectations for NCs of this size. These studies highlight the utility of resonant PL as an important tool for studies of collective phenomena in new colloidal nanomaterials.

Chapter 5

Excitonic Pathway to Photoinduced Magnetism in Colloidal Nanocrystals with Nonmagnetic Dopants

An emerging electronic-dopant in III-V and II-VI nanostructures is Ag^+, which introduces intragap electronic states optically-coupled to the host conduction band. Having a full 4d shell, Ag^+ is nonmagnetic and the dopant-related luminescence is ascribed decay of the conduction-band electron following transfer of the photoexcited hole to Ag^+. This optical-activation process and the associated modification of the electronic configuration of Ag^+ remain unclear. Here I trace a comprehensive picture of the excitonic process in Ag-doped CdSe nanocrystals and demonstrate that, in contrast to expectations, capture of the photohole leads to the conversion of Ag^+ to paramagnetic Ag^{2+}. The process of exciton recombination is thus inextricably tied to photoinduced magnetism. Accordingly, I observe strong optically activated magnetism and diluted-magnetic-semiconductor behavior, demonstrating that optically-switchable magnetic nanomaterials can be obtained by exploiting excitonic processes involving nonmagnetic impurities.

Doping chalcogenide NCs with manganese[258] has been particularly extensively investigated for applications in spin-based electronics.[199,255] Because Mn^{2+} ions are isovalent to the lattice cations, their substitutional incorporation in II-VI NCs introduces no additional charge in the system. For small, wide-band-gap CdSe NCs (E_g > 2.2 eV, Section 1.3), the Mn *d*-states behave as radiative recombination centres for band-edge excitons, resulting in the typical Mn^{2+} luminescence at ~2.1 eV sensitized by the host particle,[258] while for larger CdSe NCs (E_g < 2.2 eV, see Section 1.3 and Chapter 4), the unpaired electronic spins of the Mn-ions interact with photogenerated[261] and electrically injected[262] excitons to form magnetic polarons. Conversely, copper and silver ions introduce a single intragap deep acceptor level close to the host valence band (VB),[263-266] which radiatively captures a conduction band (CB) electron,[135,194,215,267] making the dopant-related emission subject to quantum confinement and heterostructuring.[194] Furthermore, being aliovalent with respect to cations in II-VI and III-V semiconductors, their insertion changes the overall charge within the host compound, resulting in *p*- or *n*- type doping depending on their coordination state.[134,135,187,189,194,267] For this reason, they are commonly labelled as *electronic dopants*. In the case of silver-doped NCs, electric transport measurements on Ag:CdSe NCs by Norris and co-workers reported that, in the low doping regime (<1%), Ag atoms incorporate as interstitial impurities, whereas for higher doping levels they occupy substitutional cation sites, respectively leading to *n*- or *p*-type transport.[135,268] Consistently, Kang *et al.*[187] observed *p*-type transport in field effect transistors incorporating PbSe NCs with high Ag doping level and scanning tunnel spectroscopy by Mocatta *et al.*[134] showed the Fermi level (FL) of heavily doped Ag:InAs NCs close to the VB onset. Recent theoretical calculations of the electronic structure of

Ag:CdSe NCs (3.9% Ag) predicted a deep acceptor state close to the NC valence band with optical behaviour similar to the acceptor state in NCs with Cu^+ impurities, yet with a more pronounced *s*-character deriving from the coordinating Se anions.[267]

Despite silver and copper belonging to the same group of the periodic table, their electronic properties show fundamental differences arising from the interplay between their second ionization (IE_2) and crystal-field stabilization energies. In the case of Cu (atomic radius r_0=1.35Å), the enhanced stability due to tetragonal distortion of the local environment of Cu^{2+} compensates the energy required to form a doubly-charged ion (IE_2^{Cu} = 20.29eV).[269] This results in the amphoteric character of Cu dopants, which exhibit stable oxidation states +1 or +2 depending on the position of the Fermi energy.[215,265,266] Conversely, silver is energetically less sensitive to the breakdown of local symmetry due to its ~20% larger atomic radius (1.60Å) with respect to copper, making its crystal-field stabilization energy typically insufficient to counterbalance its larger second ionization energy (IE_2^{Ag} = 21.45eV).[269-272] As a result, silver cations assume almost exclusively the +1 oxidation state, whereas stable +2 configuration is found in rare compounds where Ag^{2+} ions are protected against reduction by suitable ligands.[269,273] Consistently, in bulk metal chalcogenides, silver atoms are inserted as nonmagnetic +1 impurities[274] with electronic configuration [Kr]$4d^{10}$, often coupled to a compensating defect ensuring charge neutrality.[263,275] Having a full *d*-shell, luminescence in Ag-doped systems requires transfer of the photoexcited hole from the host VB to the Ag^+ site, which then behaves as radiative acceptor centre for a CB electron.[267,270,275,276] Similarly, Cu^+ centres are not magnetic (there is no unpaired electron spin in their full 3*d* shell) and are optically passive; capture of a VB hole is necessary to promote them to Cu^{2+} with electron-accepting capability and thereby activate the Cu-related luminescence.[215,218] For lower Fermi energies, the oxidation state of Cu becomes +2 (electronic configuration [Ar]$3d^9$): the 3*d* shell now contains one unpaired electron and therefore exhibits paramagnetic character and hole-like behaviour, resulting in the characteristic Cu-luminescence without the explicit need for a photogenerated VB hole.[194,266] Spectro-electrochemistry experiments[215] corroborated by spectroscopic measurements in the presence of a hole-scavenging Lewis base,[194] indicated that the emission efficiency of copper-doped NCs is unaffected by ultrafast trapping of the VB hole, suggesting a dominant role of substitutional Cu^{2+} centres in the emission process. In support of this picture, magnetic circular dichroism studies on the same Cu:ZnSe NCs revealed enhanced and strongly temperature-dependent Zeeman splitting of the 1S exciton, indicating *sp-d* exchange coupling between the 1S exciton to paramagnetic spins in the NC -a defining characteristic of diluted magnetic semiconductors (DMS).[217] Surprisingly, the paramagnetism of Cu-doped NCs was observed to be intensified by UV illumination. This was ascribed to the localization of the VB hole at the nonmagnetic Cu^+ making it formally Cu^{2+}-like and thereby increasing the number of paramagnetic centres in a NC.[217]

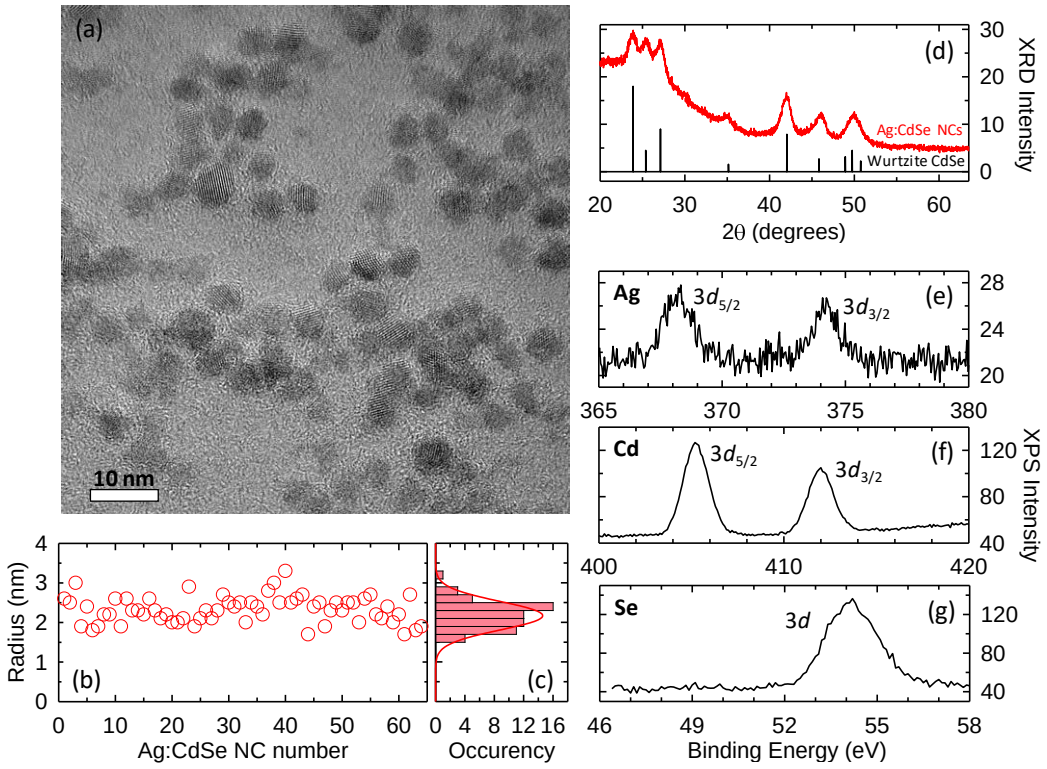

Figure 5.1 (a) Transmission electron microscopy (TEM) images of an ensemble of Ag-doped CdSe NCs. (b) Radius of 65 Ag:CdSe NCs as extracted from the TEM image in panel 'a' and (c) respective statistical analysis of the NC radius occurrences with 0.2 nm steps. The NCs' average size 2.2 ± 0.4 nm (red line). (d) X-Ray Diffraction (XRD) pattern of the same NCs (red line) together with the pattern of bulk pure CdSe in wurtzite phase (black line). X-Ray Photoelectron Spectroscopy (XPS) spectra of Ag:CdSe NCs for (e) silver, (f) cadmium and (g) selenium states.

This result brought into focus the idea that optically-switchable magnetism can be obtained by exploitation of excitonic mechanisms in nanostructures doped with nominally nonmagnetic dopants, such as silver. To date, such concept has not yet been realized and a comprehensive picture of the photophysical and magnetic phenomena in Ag-doped NCs is still lacking. In this chapter, I aimed to address this by combining photoluminescence (PL) and transient absorption (TA) measurements with spectro-electrochemical (SEC) methods and magnetic circular dichroism (MCD) spectroscopy on Ag-doped CdSe NCs. PL experiments in site-selective excitation conditions show, for the first time, that the Ag^+-related emission in Ag:NCs can be achieved both via sensitization from the NC host using above-gap excitation *and* by resonant excitation with below-gap light. This provides a first indication that the $Ag(d^{10}) + h\nu \rightarrow Ag(d^9) + e_{CB}$ transition, effectively corresponding to the transient conversion of nonmagnetic Ag^+ to paramagnetic Ag^{2+}-like species, can be promoted optically. Accordingly, TA measurements show that both the 1S excitonic band and the sub-band-gap Ag^+ absorption are bleached by band-edge excitation, confirming the promotion of the Ag^+ electron to the NC CB. The different dynamics of the 1S and dopant TA signals further enables us to measure the localization time of the VB hole in Ag^+. SEC measurements support this picture and clarify the role of radiative and nonradiative channels in the recombination mechanism. Remarkably, temperature- and

magnetic field-dependent MCD experiments show strong *sp-d* spin-exchange interactions and over 100% enhancement of the magnetic response under additional UV illumination, demonstrating the original hypothesis that ground-state nonmagnetic dopants, such as Ag^+ in II-VI NCs, can be used to realize photo-switchable nanostructures exhibiting paramagnetism. Time-resolved measurements finally show that the photoinduced MCD follows minutes-long dynamics that correlates well with the PL transient due to charging/discharging of the NCs, indicating that the lifetime of the metastable paramagnetic state is strongly extended by trapping of electrons.

5.1 - Synthesis and optical properties of Ag:CdSe NCs

Silver-doped CdSe NCs with 3% Ag were prepared via in-situ reaction and cation exchange of Ag nanoparticles (NPs).[189] Monodisperse ~5 nm Ag NPs were prepared first by adding 0.17 g of $AgNO_3$ (1 mmol) and 0.04 g of $Fe(NO_3)_3 \cdot 9H_2O$ (0.1 mmol) into the mixture of 10 mL of oleic acid and 10 mL of oleylamine at room temperature. After continuous stirring for ~10 min, the mixture was heated to 120 °C at the rate of 5 °C min^{-1}, and kept for another 60 min at 120 °C under a N_2 atmosphere. The as-prepared products were cooled down to room temperature and were collected after washing with excess ethanol for three times. The Ag NPs have been then used to prepare amorphous Ag_2Se NPs by reaction with a selenium precursor in the molar ratio of 1:5 at 50 °C. The selenium precursor was prepared from 1 mmol selenium powder with 7 mL octadecylene at 270 °C. The obtained Ag_2Se NCs (0.035 mmol) were dispersed in 10 mL toluene with 0.2 mL oleic acid and 0.1 mL oleylamine. After that, 1 mL methanol solution containing 0.1 g of $Cd(NO_3)_2 \cdot 4H_2O$ was added. After 2 mins magnetic stirring, 0.1 mL tributylphosphine was added and the mixture was heated at 55 °C for 1 hour under magnetic stirring.

The compositional and structural details of the NCs are reported in Figure 5.1. High-resolution transmission electron microscopy (HR-TEM) image shows spherical particles (Figure 5.1a) with average radius of 2.2 ± 0.4 nm (Figure 5.1b,c). Samples for TEM characterization were prepared by placing one drop of toluene solution, together with the product, onto a 300 mesh copper grid with a carbon support film. A JEOL JEM 1200EX working at 100 kV and a HR-TEM (FEI Tecnai G2 F20 S-Twin working at 200 kV) were utilized to characterize the morphology of CdSe NCs. X-ray diffraction (XRD) pattern of the Ag:CdSe NCs is reported in Figure 5.1d together with XRD spectrum of bulk CdSe in wurtzite structure for direct comparison (the experimental setup for the XRD measurement is described in Section 2.1). The NCs show the typical diffraction signal of CdSe in hexagonal crystal structure with broad peaks, characteristic of nanostructured materials. Importantly, to characterize the Ag concentration in the NCs, I carried out X-ray photoelectron spectroscopy (XPS) experiments on as-prepared Ag-doped CdSe NCs (Figure 5.1e-g). The XPS spectra were obtained with a PHI Quantera II X-ray photoelectron spectrometer using Al Kα non-monochromatic radiation. The colloidal NCs were dip-coated on silicon substrate for XPS characterization. The measurement parameters were: light spot size 100 μm; power 100 W; voltage 20 kV. An energy correction was made to account for sample charging based on the C1s peak at 284.8 eV. The Cd 3*d* peak is split into $3d_{5/2}$ (405.3 eV) and $3d_{3/2}$ (412 eV) peaks (Figure 5.1f), whereas the peak at 54.2 eV corresponds to the Se 3*d* transition (Figure 5.1g). These observed binding energies are in agreement with reported data on CdSe NCs and confirm the intrinsic CdSe lattice framework. The clear split Ag

Elemental Analysis of Ag:CdSe NCs by XPS Spectra

	Cd Atomic Concentration (%)	Se Atomic Concentration (%)	Ag Atomic Concentration (%)
Ag:CdSe NCs	55.2%	41.8%	3%

Table 5.1 Relative atomic concentrations of Cd, Se and Ag in Ag-doped CdSe NCs calculated using the XPS data shown in Figure 5.1e-g.

3*d* peak in Figure 5.1e confirms the existence of Ag^+ dopants. From the XPS data it is possible to calculate the relative atomic concentration reported in Table 5.1. The elemental concentrations in Table 5.1 are reported relative to carbon, calculated from the XPS spectra based on the area of the characteristic photoelectron peaks after correcting for atomic sensitivity. The estimated atomic concentration of Ag is ~3%, which corresponds to an average number of Ag atoms (N_{Ag}) per NC $N_{Ag} = 49 \pm 8$. In this condition, no undoped NCs are statistically expected in the ensemble.

I start the optical analysis by looking at the absorption (acquired with the instrument described in Section 2.2) and PL spectra of Ag:CdSe NCs reported in Figure 5.2a, showing the 1S absorption peak of the CdSe host at ~2.11 eV, closely resonant to a weak band-edge emission (BE-PL) at ~2.05 eV with average lifetime of ~11 ns (Figure 5.2b), likely arising from a minor subpopulation of NCs in which transfer of the photohole to the Ag^+ centre is less efficient than BE exciton decay. Here, PL measurements were performed using a pulsed diode laser at 3.05 eV (Edinburgh Inst. EPL 405, 40 ps pulse width) as excitation source and collecting the emitted light with a TM-C10083CA Hamamatsu mini-spectrometer. Time-resolved PL experiments were conducted using the same excitation source and collecting with the experimental setup used in Section 2.3 to acquire the core dynamics. All PL measurements were performed with power density of 100 nJ/cm^2. The emission spectrum of Ag:CdSe NCs is dominated by a broadband component at ~1.66 eV with average lifetime of ~220 ns (Figure 5.2b) due to the radiative decay of CB electrons to the localized intragap states of silver (Ag^+-PL), Stokes-shifted by ~ 400 meV from the 1S absorption peak.[189,267] Notably, the absorption spectrum shows a broad low-energy component extending to 1.7 eV, nearly resonant to the Ag^+-PL band. By tuning the excitation energy from 3.0 eV (above CdSe band-gap) down to 1.8 eV (below NC band-edge) Ag^+-PL is still observed (Figure 5.2c). This indicates that the *d*-electrons of Ag^+ can be promoted to the NC conduction band by direct optical excitation using sub-band-gap excitation following the reaction $Ag(d^{10}) + h\nu \rightarrow Ag(d^9) + e_{CB}$, where Ag^+ species are temporarily photoconverted into Ag^{2+}-like centres. As a result, the PL excitation (PLE) spectrum of the 1.7 eV emission shown in the inset of Figure 5.2a resembles well the absorption profile down to sub-band-gap energies. A scheme of the photophysical mechanism under either above-gap or below-gap excitation is reported in the inset of Figure 5.2c. For PLE and PL experiments under resonant excitation conditions, a spectrally narrow photoexcitation source (< 0.5nm full width at half-maximum) was produced by filtering the output of a 150 W Xenon lamp with a

1/3 m double-grating Gemini monochromator. The emitted PL was collected with a Horiba Scientific Triax 180 1/2 m spectrograph and detected with an Instrument SA Spectrum One liquid nitrogen cooled CCD.

Independent confirmation of the proposed mechanism is provided by the TA spectra under BE excitation and intragap pumping of Ag^+ in Figure 5.2d. The experimental setup is similar to that

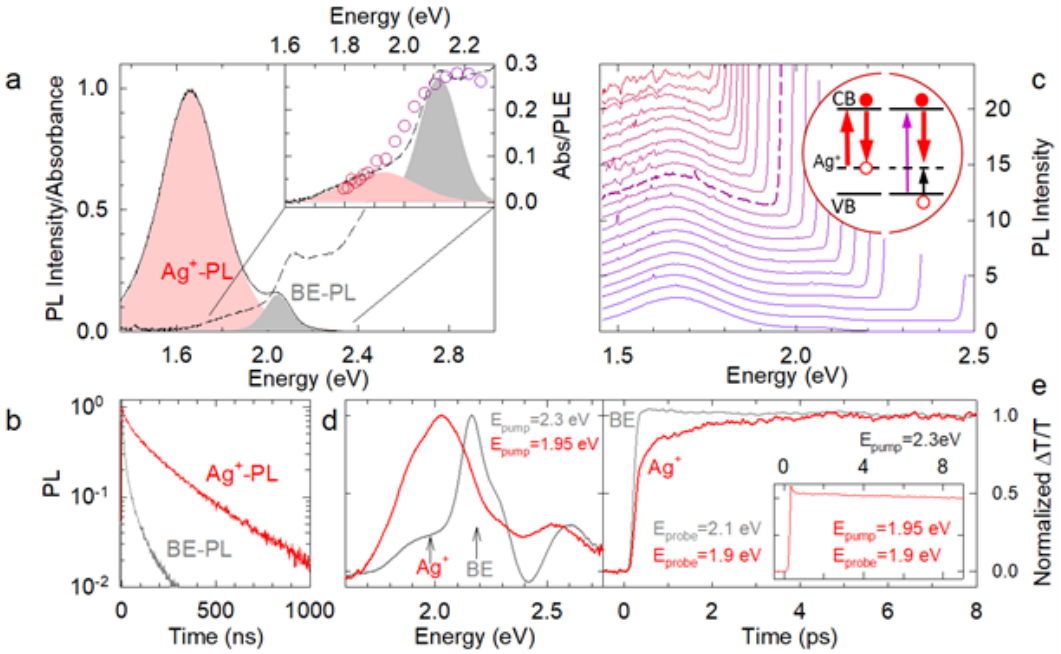

Figure 5.2 (a) Optical absorption (dashed line) and photoluminescence (PL) spectra of Ag-doped CdSe NCs (pulsed excitation at 3.05 eV, 500 kHz repetition rate, 100 nJ/cm^2, 2 seconds acquisition time) in toluene showing the band-edge PL band (highlighted in grey) and the dopant-related emission (red shading). The inset shows an enlargement of the 1.6-2.25 eV region emphasizing the intragap absorption band peaked at ~1.9 eV due to sub-band-gap absorption by the Ag^+ impurities (red shading) on the low-energy side of the 1S feature at ~2.1 eV (grey shading). The circles report the PL excitation (PLE) spectrum of the Ag^+-PL at ~1.65 eV. (b) PL decay curves of the BE-PL and the Ag^+-PL measured at 2.05 eV and 1.66 eV (bandwidth ~20 meV) using 3.05 eV excitation. (c) PL spectra of the same NCs under progressively lower energy excitation (from bottom to top). The colour scheme is the same as the respective circle in the inset of 'a'. A portion of the excitation light is included for reference; it allows for direct comparison between the different measurements. The dashed line roughly indicates the transition between above-gap and below-excitation depicted in the right and left-hand side of the scheme shown in the inset. All these measurements are performed at room temperature. (d) Normalized transient transmission spectra after band-to-band pumping at 2.3 eV (grey curve) and intragap excitation of Ag^+ at 1.95 eV (red curve). The spectra are collected after 1.5 ps delay, in both cases the fluence is set to excite an average of 0.1 excitons per NC. (e) Normalized bleaching ΔT/T kinetics at the 1S absorption (2.1 eV, grey line) and of the Ag^+ absorption (1.9 eV, red line) upon pumping close to the band-edge at 2.3 eV to discard thermalization effects. The bleaching of the 1S absorption is instantaneous whereas the Ag^+ signal shows a longer rise time due to transfer of the photohole from the VB to Ag^+. Inset: The kinetics of the Ag^+ bleaching becomes instantaneous upon direct pumping at 1.95 eV. The fast component at early delay times is due to interference effects.

described in Section 2.4. The laser is a Coherent LIBRA-HE Ti:sapph featured by 95 fs pulse duration at 800 nm and 2 kHz repetition rate. The excitation pulses at 2.3 eV (540 nm) and 1.95 eV (635 nm) were generated with an Optical Parametric Amplifier (OPA). The bandwidth of the pump pulses is 10 nm which correspond to a pulse duration ~100 fs. Pump fluences in the position of the white probe light are in the order of 35 μJ/cm^2 for 2.3 eV pump energy and 95 μJ/cm^2 for 1.95 eV pump energy. The probe beam is generated as described in Section 2.4. The acquisition and pump-probe delay systems are the same as in Section 2.4.

Band-edge pumping results in the typical TA spectrum of CdSe NCs, with an intense positive band at ~2.15 eV corresponding to bleaching of the 1S absorption due to state filling of the double-degenerate CB.[277] More importantly, the TA spectrum shows an additional positive band resonant to the Ag^+ absorption at 1.9 eV, which indicates that the transition of Ag^+ centres is bleached by BE pumping. Note also that under intragap pumping of Ag^+ at 1.95 eV, further to the Ag^+ bleaching, I observe the photo-bleaching of the 1S absorption, with its excitonic components. Both these effects confirm that direct excitation of Ag^+ promotes its *d*-electron to the NC CB (leading to photo-bleaching by state filling). The inspection of the time transients of the bleaching signals in Figure 5.2e further enables us to measure the hole localization time from the NC VB to the Ag^+. Under BE pumping at 2.3 eV, the 1S bleaching growth is instantaneous with a rise time below the resolution limit of our apparatus (about 100 fs). In contrast, the Ag^+ bleaching rise shows a slower component with a time constant of ~1.4 ps. Differently under intragap direct Ag^+ excitation, with 1.95 eV light (inset of Figure 5.2e), the Ag^+ bleaching growth is instantaneous. Thus the difference in the bleaching signals is related to hole dynamics, in particular under BE excitation the slow rise time describes the migration of the photohole from the NC VB to the Ag^+, similarly to the hole localization observed in CdSe/CdS core/shell structures upon shell excitation.[107]

5.2 – Spectro-electrochemistry Experiments

To confirm the above mechanism and to clarify the nature of the intragap dopant state, I conduct SEC experiments on Ag-doped NCs. The custom experimental setup is illustrated in Figure 5.3a. Specifically, indium tin oxide (ITO) coated glass slides (50×7×0.7 mm, R_S < 100 Ω) were purchased from Delta Technologies (Part No. CG-90IN-CUV). The ITO coated surface was first covered with zinc oxide (ZnO) nanoparticles (NP) (Nanograde, ~50 nm diameter) to avoid quenching of NC emission by fast charge/energy-transfer to ITO. The ZnO NP layer (~60 nm thick, as measured using a Dektak profilometer) was deposited by dip-coating the glass/ITO substrate into an ethanol suspension of ZnO NPs (2 mg/mL, one dip for 10 s) and annealed at 150° C for 10 min in a nitrogen glovebox. To test the stability of the glass/ITO/ZnO NP substrates during the potential scans, I performed control experiments in which I monitored changes in optical absorption spectra for prolonged exposures to negative and positive potentials. The results of these measurements indicate that the substrates are unaffected by either positive or negative EC potentials for exposure times of tens of minutes, which are much longer than the measurement time used in our SEC experiments (~10 min). The NCs were deposited onto the ZnO NP layer as a few-monolayer-thick film by dip-coating from a dilute toluene solution (optical density of 0.07 at 500 nm; 2 dips for 10 s). The ZnO NPs layer used in this study was not treated with cross-linkers and therefore it represented a dielectric tunnelling

barrier of ~1 V. The introduction of the additional ZnO spacer along with the presence of insulating surface ligands can also lead to an appreciable attenuation of the actual shift of the Fermi level compared to the nominal applied EC potential. The ITO was connected as a working electrode to the potentiostat (Bio Logic SP-200 Research grade Potentiostat/Galvanostat) and the film was placed into a quartz cuvette filled with the electrolyte (0.1 M tetrabutylammonium

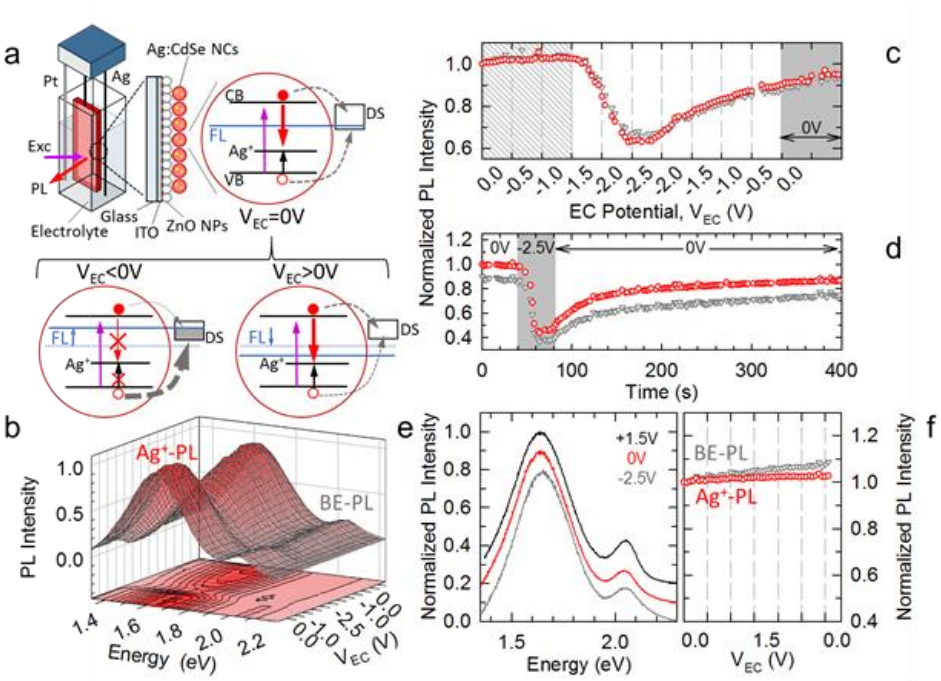

Figure 5.3 (a) Schematics of the SEC setup consisting of an EC cell with tetrabutylammonium perchlorate in propylene carbonate (0.1 M) as an electrolyte and a working electrode comprising an ITO-coated glass covered with a layer of ZnO nanoparticles (NPs) and Ag:CdSe NCs. The figure also illustrates the radiative recombination pathway (red arrow) of photoexcited conduction band (CB) electrons to the intragap Ag-state following the capture of the valence band (VB) hole (black arrow). The competitive nonradiative carrier trapping processes to defect states (DS) are shown as grey dashed arrows. The effect of the EC potential on the PL intensity depends on the filling/emptying DS (right of the band diagram) in response to changes in the position of the Fermi level (FL; blue line). (b) A series of PL spectra (0.5 s acquisition time per frame) for a stepwise scan of the EC potential to negative values (100 mV steps each lasting 10 s). (c) Spectrally integrated intensity of the BE and Ag^+-PL bands (grey triangles and red circles respectively) as a function of V_{EC} extracted from the spectra in 'b'. The patterned area for $V_{EC} \leq 1V$ highlights the regime in which the ZnO NPs interlayer and the dielectric ligands attenuate the effect of the applied potential. The grey shaded portion emphasizes the PL growth over time at $V_{EC}=0V$. (d) Intensity of the BE and Ag^+-PL bands (grey triangles and red circles respectively) for excitation at 3.05 eV during ON/OFF voltage cycles for the negative electrochemical potential (V_{EC} = 0, −2.5, 0 V) showing the recovery of the initial intensity due to slow release of trapped holes. e. Normalized PL spectra at V_{EC} = 0 V (red line), -2.5 V (grey line) and +1.5 V (black line). The spectra are shifted vertically for clarity. (f) Spectrally integrated PL intensity during a stepwise scan of the EC potential to positive values (100 mV steps each lasting 10 s). All intensities in 'c', 'd' and 'f' are normalized to their values at V_{EC} = 0 V. All measurements are conducted using 3.05 eV excitation with fluence of 100 nJ/cm^2.

perchlorate, $TBAClO_4$, in propylene carbonate). Silver and platinum wires were used as quasi-reference and counter electrodes, respectively. All potentials reported in this work are measured relative to the quasi-reference silver electrode during staircase voltammetry scans (10 s scan rate). The film was excited at 3.05 eV with continuous wave diode lasers and the emitted light was collected with a focusing lens and sent to a spectrometer coupled to a USB4000 Ocean Optics spectrometer.

Together with the experimental setup, Figure 5.3a also reports a schematic depiction of the NC band structure featuring the fully occupied *d*-state of Ag^+ in the lower part of the energy gap. In unperturbed conditions, the FL is placed between the Ag^+-level and the conduction band of the NC host. The intragap defect states (DS) responsible for the SEC behaviour are placed in energy slightly above the FL, in agreement with the EC response described below. The NCs are excited with a continuous-wave laser and the PL is collected under the application of an EC potential (V_{EC}) that tunes the position of the FL.[215,278] Specifically, negative V_{EC} correspond to a raising Fermi energy and leads to passivation of nonradiative traps for photoexcited electrons. Concomitantly, excess electrons accumulated in surface defects become efficient traps for photogenerated holes. Conversely, positive V_{EC} (corresponding to lowering the FL) depletes the NC of photoexcited electrons and concomitantly passivates hole-trapping defect states. The brightening versus quenching effect of V_{EC} on the NC emission efficiency is therefore determined by the competition between the selective passivation/activation of carrier traps, by the respective trapping rates and by the occupancy of the surface states in unperturbed conditions. For this reason, SEC measurements are particularly useful for identifying the trapping mechanisms that mostly affect the exciton decay and therefore can help to design specific passivation strategies for optimizing the PL yield of NCs. Furthermore, the selectivity of SEC measurements for band-edge carriers enables us to probe the nature of intragap states (i.e. donor *vs*. acceptor, both intrinsic due to points defects or introduced by doping) involved in the recombination mechanism and to reveal the sequence of events leading to radiative decay.

I start by applying a negative V_{EC} to Ag:CdSe NCs. In Figure 5.3b, I report the complete set of PL spectra of the NCs under application of a negative V_{EC} scanned from 0 V to −2.5 V and then back to 0 V. To quantify the effect of the EC potential on the efficiency of the BE-PL and the Ag^+-PL, in Figure 5.3c I show the evolution of the respective integrated PL intensity during the scan. For $|V_{EC}| < 1.5$ V, no significant effect is observed. This is in agreement with previous SEC results on NCs using ITO/ZnO substrates and is due to the effect of the dielectric surface ligands and of the potential drop across the ZnO layer.[116,215,279] At negative $V_{EC} \geq -1.5$ V, both PL intensities undergo a sudden drop, reaching ~40% dimming at $V_{EC} = -2.5$ V. For both emissions, when returning to V_{EC}=0V, the PL intensity increases resulting in ~ 90% recovery of the original intensity at V_{EC}=0V. It is worth noting that the PL brightening is markedly slower than the respective drop and proceeds over time also when no potential is applied, with an additional 5% recovery after about one minute at $V_{EC} = 0$ V. In order to investigate this aspect in deeper detail, I have performed an ON/OFF scan, in which the PL is continuously monitored while the potential, initially set to $V_{EC} = 0$ V, is raised to -2.5 V where it is kept constant for 30 s after which it is brought back to 0 V.

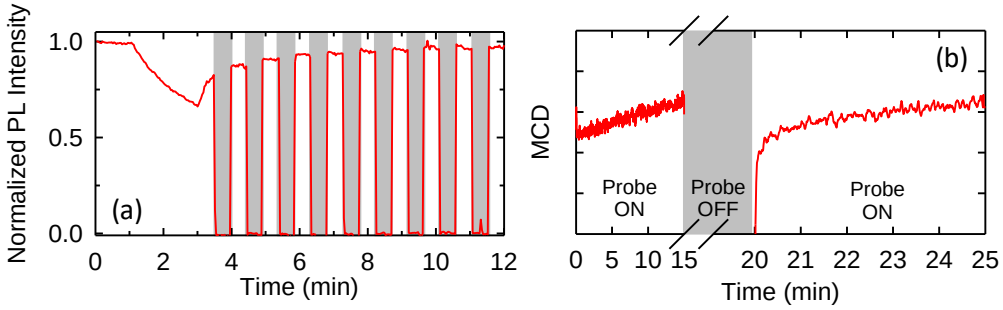

Figure 5.4 (a) Intensity of the Ag^+-PL band during an ON/OFF voltage cycle for the negative electrochemical potential (V_{EC} = 0, −2.5, 0 V) under intermittent excitation at 3.05 eV (shaded area corresponds to laser OFF conditions) highlighting that the recovery of the PL intensity is essentially unaffected by photoexcitation. (b) Time evolution of the peak MCD signal as the probe beam is turned OFF (grey shading). After 5 minutes in totally dark conditions (no probe, no additional illumination), the MCD intensity is markedly lower and is observed to intensify over time. This further indicates that detrapping (responsible for the slow MCD dynamics) is not a photo-assisted process.

The evolution of the integrated intensity of the BE-PL and the Ag^+-PL during the scan are reported in Figure 5.3d, showing the sudden drop of both bands with applied negative V_{EC} followed by their slow recovery that proceeds over time for ~15 minutes. This indicates that the potential sweep causes no significant damage to the NC surfaces, as confirmed by the inspection of the PL spectra collected for different V_{EC} values (Figure 5.3e) that show identical emission profiles in all EC conditions. The SEC response is therefore ascribed to reversible activation/passivation of trap sites likely associated with under-coordinated surface atoms or dangling bonds. Specifically, since the application of negative V_{EC} passivates electron traps and concomitantly activates hole traps, the observed drop of the PL intensity suggests that nonradiative trapping of holes in activated defects states is not counterbalanced by the concomitant PL brightening effect of suppressed electron trapping. The slow PL recovery at V_{EC} = 0 V, in turn, suggests slow detrapping of trapped holes, in agreement with the long discharging time found in IV-VI NCs.[280] I notice that the PL recovery is unaffected by illumination and occurs nearly identically under continuous or intermittent excitation condition (Figure 5.4a). Most importantly, the similar SEC response of the BE-PL and the Ag^+ emission, indicates that the intrinsic and dopant-related decay pathways are equally quenched by hole trapping, which confirms the picture of the dopant-related emission requiring the localization of a photoexcited VB hole in the Ag^+ site to activate its capability of accepting a CB electron. The SEC measurements performed under intragap excitation of the Ag^+-PL are reported in Figure 5.5. Figure 5.5a,b show the SEC response of the Ag:CdSe NCs under negative V_{EC} and intragap excitation of the Ag^+-PL at 1.95 eV. Data reveal a ~25% dimming of the Ag^+ luminescence under negative potential, which is nearly half of the drop observed under above-gap excitation. This is consistent with the fact that the silver centres are located inside the NCs core and more protected from surface electrons than the photoexcited valence band holes of the NC host. Notably, the dynamics of the SEC response under intragap excitation (Figure 5.5c,d) nearly instantaneous with the voltage variation, in contrast with the behaviour observed under UV excitation. This suggests that the EC response under intragap excitation of

the Ag^{+} ions is primarily due to direct reduction of the photoexcited Ag^{2+} like species by the additional electrons provided by the negative EC potential, which is in agreement with the high reactivity of doubly charged silver ions.

Finally, I also performed SEC measurements under positive potentials, which provide complementary insight into the nature of the surface defect states. The results, reported in Figure 5.3g, show no variation of either the BE-PL or the Ag^{+}-PL for V_{EC} up to +1.5 V. Since these NCs are not passivated with a thick wide energy gap shell that suppresses electron trapping, the absence of a quenching effect by positive V_{EC} points to a situation in which localized states are positioned in energy just above the FL of the NCs, that is, they are already devoid of electrons at V_{EC} = 0 V (Figure 5.3a). As a result, similar to what observed in perovskite NCs,[279] their occupancy cannot be further reduced by positive V_{EC}, which makes the PL essentially insensitive to oxidative potentials. This argument also explains the absence of a PL brightening effect due to suppressed hole trapping by EC removal of excess electrons localized in NC surface states and indicates that, in unperturbed conditions, electron trapping is the main responsible for the nonradiative losses in our NCs (PL quantum yield, $\Phi_{PL} \sim 5\%$). Finally, the position of the localized states deep inside the NC energy gap is in agreement with the observed minute-long

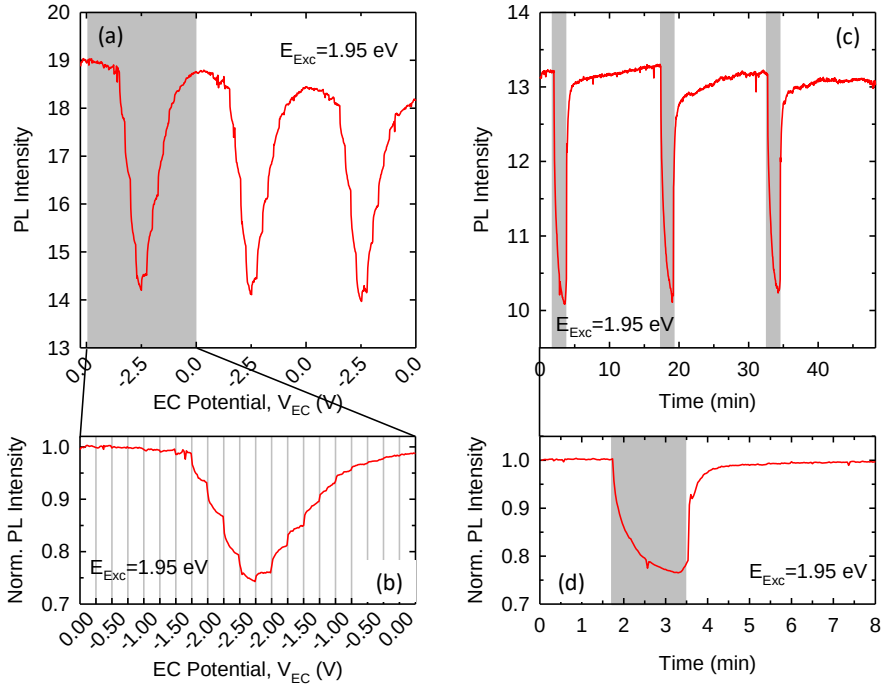

Figure 5.5 (a) Spectrally integrated intensity of the Ag^{+}-PL band as a function of V_{EC} (250 mV steps each lasting 30s) under intragap excitation at 1.95 eV. The measurement was performed trice to highlight the reproducibility of the EC response. (b) Enlargement of the first SEC cycle showing the multistep drop of the PL intensity with increasing negative V_{EC}. (c) Intensity of the Ag^{+}-PL band for excitation at 1.95 eV during ON/OFF voltage cycles for the negative electrochemical potential (V_{EC} = 0, −2.5, 0 V) showing the rapid recovery of the initial intensity. (d) Enlargement of the first cycle in 'c' highlighting the instantaneous recovery of the initial PL intensity upon removal of the EC potential. All measurements are conducted using 1.95 eV continuous wave excitation with fluence of 10 W/cm^2

detrapping time of trapped holes at V_{EC} = 0V leading to the asymmetry between the dimming versus brightening dynamics (Figure 5.3c,d).

5.3 - Magnetic Circular Dichroism Measurements

One important consequence of the recombination mechanism emerging from the PL, TA and SEC measurements is that the optical activity (that is, the electron-accepting capability) of the dopant site depends on the transient excitation of Ag^+ from its $4d^{10}$ ground state configuration with nonmagnetic character to $4d^9$ with paramagnetic behaviour. An analogous process underpins the optical excitation of Cu^+-doped NCs, leading to the formation of paramagnetic Cu^{2+} centres whose unpaired electron spin leads to a strong *sp-d* spin-exchange between the 1S exciton and the embedded paramagnetic Cu^{2+} (ref. [217]). In Ag-doped NCs, because of the large second ionization energy of Ag not being compensated by the local lattice distortion, such behaviour would be somewhat unexpected. On the other hand, an experimental observation of *sp-d* exchange between the NC bands and any unpaired *d*-electrons of silver, would unambiguously indicate that capture of the VB hole leads to a metastable Ag^{+2}-like excited state

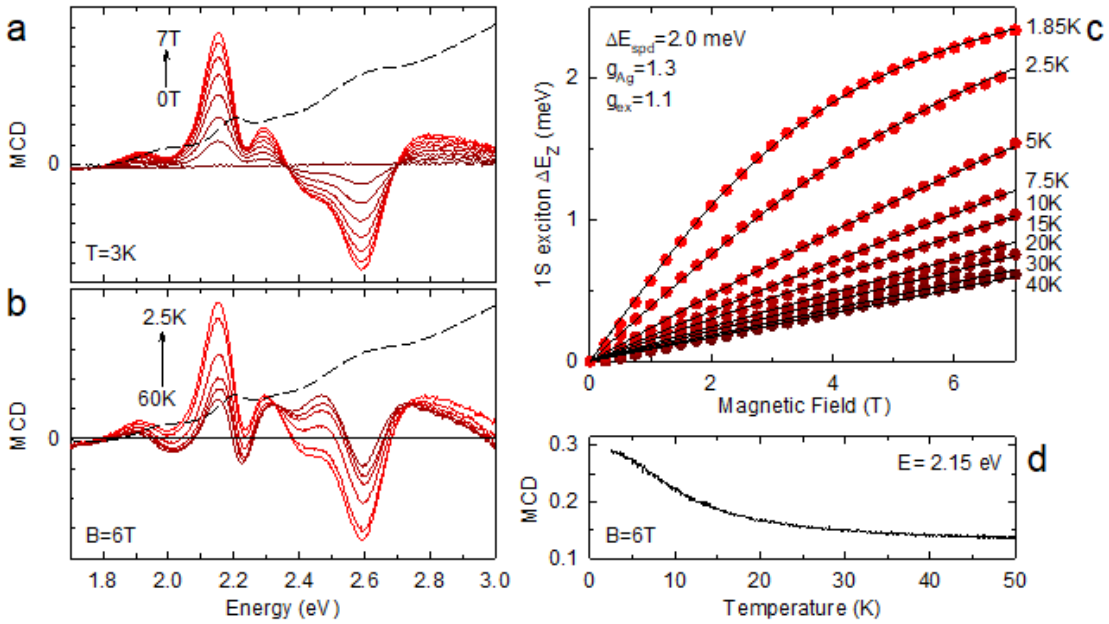

Figure 5.6 MCD spectra of Ag:CdSe nanocrystals, from which the Zeeman splitting of the 1S exciton can be inferred. (a) MCD spectra are shown at 3 K in different magnetic fields from 0 to 7 T. (b) MCD spectra at 6 T, at temperatures from 2.5 to 60 K. The linear absorption spectrum is reported as dashed black line in both 'a' and 'b' for direct comparison with the MCD spectrum. (c) Enhanced Zeeman splitting of the 1S band-edge exciton versus magnetic field, at different temperatures. The high field saturation and strong temperature dependence indicate the existence of *sp–d* exchange coupling between the conduction/valence bands of the semiconductor host and a paramagnetic species in the nanocrystals. This species is likely Ag dopants excited by fast localization (capture) of the valence band hole. Lines are fits to a Brillouin function using a single set of parameters. d. Intensity of the MCD signal of the 1S exciton at 6T as a function of temperature from 2.5 K to 50 K.

in CdSe NCs and would demonstrate that DMS physics can be triggered optically in NCs with nonmagnetic dopants.

In order to address this aspect, I performed MCD experiments as a function of temperature and magnetic field (B). I used standard MCD methods[26] to measure the field- and temperature-dependent Zeeman splitting (ΔE_Z) of the 1S exciton absorption resonance in our nanocrystals, from which the presence of any additional *sp-d* exchange coupling of the exciton to paramagnetic dopants can be inferred. As in conventional diluted magnetic semiconductors,[138] paramagnetic moments in the nanocrystal are revealed via an enhanced and strongly temperature dependent ΔE_Z. MCD measures, as a function of photon energy, the (normalized) difference in transmission between right- and left-circularly polarized light through the nanocrystal film in the Faraday geometry, $(T_R - T_L)/(T_R + T_L)$.[199] When the Zeeman splitting is small compared to the width of the 1S exciton absorption (as is the case here), the MCD spectrum is therefore derivative-like with a low-energy maximum that is proportional to ΔE_Z. NC films were mounted in the variable-temperature insert (1.5–300 K) of a 7 T superconducting magnet with direct optical access. Probe light of tuneable wavelength was derived from a Xenon lamp directed through a spectrometer. The probe light was mechanically chopped at 137 Hz, and was modulated between right and left circular polarizations at 50 kHz using a photo elastic modulator. The transmitted light was detected with a silicon avalanche photodiode. Photo-magnetization was induced with additional light from a continuous wave 3.05 eV diode laser.

In Figure 5.6a, I report the MCD spectra of Ag:CdSe NCs at increasing magnetic field up to B=7 T at 3 K, together with the corresponding linear absorption spectrum. The MCD spectrum shows two main peaks at ~2.15 eV and ~2.6 eV corresponding to the NC's 1S and 2S exciton absorption peaks and a minor contribution at 1.9 eV due to direct absorption by the Ag^+ dopants.

Fundamentally, the magnetic response of the 1S absorption peak shows intensification with increasing B and decreasing temperature (Figure 5.6b), revealing strong paramagnetic response. I stress that, temperature-dependence of the MCD is the most direct and arguably the only definitive indication of the presence of coupling between carriers in the NC bands and paramagnetic species.[199,217] Data in Figure 5.6 are therefore unambiguous signatures of *sp-d* exchange due to the progressive alignment of the photoexcited Ag^{2+} spins to the magnetic field. This provides the first demonstration of photoinduced DMS physics in Ag-doped NCs.[138] To further quantify this effect, I extracted the Zeeman splitting energy (ΔE_Z) of the 1S exciton as a function of B and temperature. In Figure 5.6c, I report the evolution of ΔE_Z upon continuously increasing B from 0 to 7 T in the 1.85-40 K temperature range. In agreement with Figure 5.6a and 5.6b, ΔE_Z is markedly temperature-dependent and shows clear saturation for T < 5 K. This is supported by the fitting of ΔE_Z with the Brillouin functional form for conventional DMS materials[138] of Eq. (1.16) where the first term is the linear and temperature-independent Zeeman splitting arising from the intrinsic Landé-factor of the CdSe exciton (g_{ex})[26] and the second term accounts for any additional splitting due to the *sp-d* exchange interaction between the semiconductor bands and the dopant spins.[138] The magnitude of *sp-d* splitting energy, $\Delta E_{sp\text{-}d}$, is weighted for the average spin projection along B, which is modelled by the Brillouin function $B_J(g_{Ag}\mu_B JB/k_BT)$, describing the magnetic field and temperature dependent paramagnetism of

the ions with spin *J*. Here, g_{Ag} is the Ag^{2+} *g*-factor, μ_B is the Bohr magneton and k_B the Boltzmann constant. For d^9 dopants in II-VI compounds,[281,282] the tetragonal crystal-field lowers and increases the energy of the six-fold degenerate t_{2g}-states and of the four-fold degenerate e_g-states respectively. Therefore, I use $J = 1/2$ for the lowest Kramer doublet to fit the experimental data with Eq. (1.16) (black lines, Figure 5.6c), setting as shared parameters the *sp-d* exchange interaction and the exciton and dopant Landé-factors. The best fit of whole set of data in Figure 5.6c is obtained using $\Delta E_{sp\text{-}d} = 2.0$ meV, $g_{ex} = 1.1$, and $g_{Ag} = 1.3$. The obtained g_{ex} is comparable to the values reported for both undoped[26,38,283] and copper-doped CdSe NCs[284], and g_{Ag} is consistent to Ag-doped bulk ZnSe showing magnetic response that was suggested to originate from a photoexcited $[Ag_{Zn}^{2+}\text{-}Se^{2-}\text{-}Ag_i^{+}]^{+}$ paramagnetic acceptor complex involving a substitutional and an interstitial silver ion.[285] The effect of temperature on the MCD intensity at the 1S absorption energy is quantified in Figure 5.6d, confirming the strong paramagnetic response below T = 20K. Within the assumption of a random and uniform distribution of the Ag^+ ions in the CdSe NCs, it is possible to approximately estimate the net exchange constant. Following standard procedures developed for traditional DMSs (i.e. Mn-doped nanostructures):

$$\Delta E_{sp-d} = S_{eff} * [Ag^+] * N_0(\alpha - \beta) \qquad (5.1)$$

where $[Ag^+]$ is the silver concentration (3%, see Section 5.1), S_{eff} is the effective Ag spin (taken to equal 1/2) and $N_0(\alpha\text{-}\beta)$ is the combined exchange constant for both conduction and valence band. This gives a net exchange constant $N_0(\alpha\text{-}\beta) \sim 130$ meV, which is approximately one order of magnitude smaller than for the classic case of spin-5/2 Mn^{2+} in CdSe.[199]

5.4 - Photoinduced paramagnetism in Ag:CdSe NCs

It is worth noting that the observed magnetic behaviour in Ag:CdSe NCs is not a ground-state property, but a photoinduced effect due to the probe light that is used for the MCD measurements that necessarily matches the absorption spectrum of the NCs. This effect is highlighted in Figure 5.7a,b, showing the linear growth of the MCD signal with increasing probe intensity. This behaviour is unusual because the MCD signal is an intrinsically normalized physical quantity corresponding to the ratio between the absorption difference of right- and left-circularly polarized light and the intensity of the transmitted portion of the light probe. Therefore, the amplitude of the MCD signal for conventional magnetic materials is independent of the intensity of the probe beam. Conversely, in our case the observed strong dependence of the MCD amplitude on the probe intensity is direct consequence of the particular physics of Ag^+ dopants in CdSe NCs. To further investigate this aspect, I performed MCD spectroscopy at B = 6 T in the presence and in the absence of additional 3.05 eV laser excitation (excitation fluence $\sim$10 $\mu W/mm^2$). Remarkably, as shown in Figure 5.7c, the MCD signal increases substantially up to by $\sim$100% upon additional illumination with UV light without any spectral modification. The effect of the additional illumination is further emphasized in Figure 5.7d, where I report the MCD signal of the 1S absorption peak at 2.15 eV during a magnetic field ramp

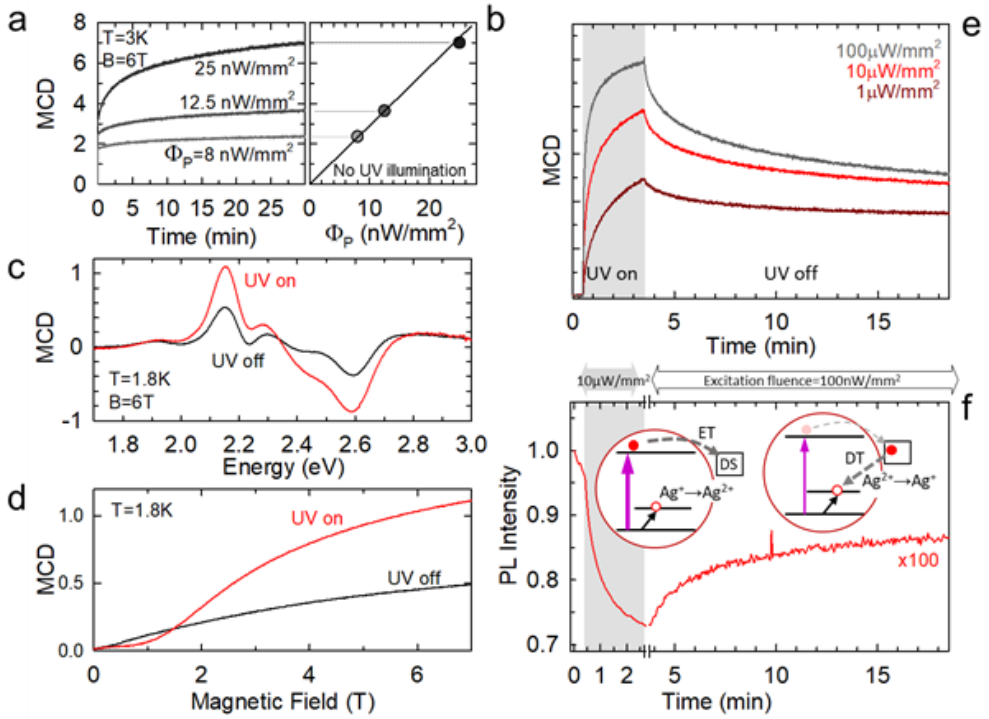

Figure 5.7 (a) Evolution of the MCD signal of the 1S exciton of Ag:CdSe NCs over time measured at 3K and 6T using increasingly higher probe fluence. (b) Linear dependence of the MCD intensity on the probe intensity (as measured after 30 minutes). (c) MCD signals measured at constant probe intensity in the presence (red line) and in the absence (black line) of additional illumination with 3.05 eV ultraviolet light (100 μW/mm^2). In order to avoid parasitic heating effects by the UV light source, I performed the experiments in superfluid helium at T=1.8 K, which ensures optimal heat sinking. (d) Peak MCD signal (measured at 2.15 eV) as a continuous function of applied magnetic field with and without additional UV illumination (100 μW/mm^2). (e) Time evolution of the peak MCD signal as the additional UV illumination is turned on (grey shading) and off. Stronger UV light leads to larger MCD signal and faster dynamics of both 'on' and 'off' phases. In all cases, the MCD decay is markedly slower than the corresponding rise under UV excitation. (f) Time evolution of the integrated PL intensity under low or high excitation regimes, corresponding to the UV-off and UV-on conditions in the MCD scan in 'e'. The time axes are on the same scale for direct comparison of the similar temporal dynamics, emphasizing the close anti-correlation between the PL intensity and MCD signal. Inset: schematic depiction of the electron trapping(ET)/detrapping(DT) mechanisms in defect states (DS) responsible for the ultra-long lifetime of the metastable paramagnetic state. Under intense (10 μW/mm^2) UV excitation (left scheme), the PL is quenched by ET that enhances the MCD signal in 'd' by favouring the accumulation of photoinduced paramagnetic Ag^{2+} states. When the UV excitation is lowered to 100 nW/mm^2 (right scheme), slow DT of trapped electrons leads to recovery of the PL signal and concomitant decrease of the MCD intensity.

up to 7 T, with and without UV illumination, confirming, in both cases, the strongly nonlinear field-dependence characteristic of *sp-d* exchange (Figure 5.6c). Apart from the low-field region

(< 2 T), both trends are well described by Eq. (1.16) using appropriate scaling of $\Delta E_{sp\text{-}d}$ to account for the larger number of photo-activated paramagnetic impurities in the sample.

To gather deeper insights into the effect of photoexcitation on the magnetic response of Ag:CdSe NCs and to identify correlations with the exciton recombination mechanism emerging from the SEC results, I monitored the evolution of the photoinduced MCD over time as a function of the UV excitation fluence. As shown in Figure 5.7e, increasing the fluence of the UV light leads to faster MCD growth and higher maximum values (as measured after 3 minutes monitoring), confirming the direct relationship between the magnetization and NC excitation. It is worth noticing that, at all adopted UV excitation fluence, the NCs are well within the single exciton regime and thus only one Ag^{+} centre per NC is photoconverted to Ag^{2+}. The intensification of the MCD signal with increasing UV excitation power is, therefore, due to larger number of photoexcited NCs in the ensemble. Interestingly, for all fluence used, when the UV laser is turned off, the MCD signal decreases very slowly over several minutes. Such minute-long persistence of the metastable paramagnetic state, extending for over nine orders of magnitude longer than the dopant emission lifetime (~220 ns, Figure 5.2b), indicates that radiative decay of the CB electron in the silver state is not the determining process in the $Ag^{2+} \rightarrow Ag^{+}$ dynamics responsible for the drop of the photoinduced MCD. This effect can be explained by the presence of localized states positioned in energy above the NC Fermi energy efficiently trapping CB electrons, as indicated by SEC in Figure 5.3. Because of electron trapping, the lifetime of the metastable paramagnetic state would be dramatically extended with respect to the corresponding PL decay and the MCD recovery time would be dictated by the electron detrapping dynamics (see scheme in Figure 5.7f). This suggests a direct correlation between the MCD growth (drop) and the PL dimming (brightening) due to carrier trapping (detrapping). In order to experimentally validate this hypothesis, I monitored the PL intensity of the Ag-doped NCs film over an analogous time scale as the MCD time trace. To reproduce the conditions of the MCD scan in the absence of additional UV illumination, I used 3.05 eV light with 100 nW/mm^2 fluence. The situation in which the sample is exposed to further UV excitation is recreated by increasing the fluence to 10 μW/mm^2, corresponding to the laser intensity used in the photoinduced MCD experiments. In all excitation conditions, the excitation rate is well below 10^{-3} excitons/NC, thus excluding multiexcitonic effects. Figure 5.7f shows the remarkable anti-correlation between the PL trend and the MCD time trace in Figure 5.7e, with the emission intensity undergoing a relatively faster drop under intense UV excitation due to photocharging by electron trapping, while the MCD signal is concomitantly intensified. Once the excitation fluence is reduced to 100 nW/mm^2, the PL intensity is slowly recovered on a time scale compatible to the slow decay of the photoinduced MCD. This result confirms the above assumption that the process responsible for the persistence of the photoinduced magnetism is likely the slow release of CB electrons trapped in relatively deep acceptor surface states.

5.5 - Conclusion

In summary, through the combination of complementary optical, spectro-electrochemical and magnetic circular dichroism experiments I showed that NCs doped with silver ions exhibit optically-activated paramagnetic properties and concomitant *sp–d* exchange interactions between excitons and Ag dopants, suggesting that optically switchable magnetic nanomaterials

can be obtained by exploiting the excitonic processes involving nominally nonmagnetic impurities.

Chapter 6

Spectro-electrochemical Probing of Intrinsic and Extrinsic Processes in Exciton Recombination in I–III–VI_2 Nanocrystals

Ternary $CuInS_2$ (CIS) nanocrystals are attracting attention as nontoxic alternatives to heavy-metal–based chalcogenides for many technologically relevant applications. The photophysical processes underlying their emission mechanism are, however, still under debate. Here I address this problem by applying, for the first time, spectro-electrochemical methods to core-only CIS and core/shell CIS/ZnS nanocrystals. The application of an electrochemical potential enables us to reversibly tune the nanocrystal Fermi energy and thereby control the occupancy of intragap defects involved in exciton decay. The results indicate that, in analogy to copper-doped II–VI nanocrystals, emission occurs via radiative capture of a conduction-band electron by a hole localized on an intragap state likely associated with a Cu-related defect. I observe the increase in the emission efficiency under reductive electrochemical potential, which corresponds to raising the Fermi level, leading to progressive filling of intragap states with electrons. This indicates that the factor limiting the emission efficiency in these nanocrystals is nonradiative electron trapping, while hole trapping is of lesser importance. This observation also suggests that the centres for radiative recombination are Cu^{2+} defects (preexisting and/or accumulated as a result of photoconversion of Cu^{1+} ions) as these species contain a pre-existing hole without the need for capturing a valence-band hole generated by photoexcitation. Temperature-controlled photoluminescence experiments indicate that the intrinsic limit on the emission efficiency is imposed by multiphonon nonradiative recombination of a band-edge electron and a localized hole. This process affects both shelled and unshelled CIS nanocrystals to a similar degree, and it can be suppressed by cooling samples to below 100 K. Finally, using experimentally measured decay rates, I formulate a model that describes the electrochemical modulation of the PL efficiency in terms of the availability of intragap electron traps as well as direct injection of electrons into the nanocrystals conduction band, which activates nonradiative Auger recombination, or electrochemical conversion of the Cu^{2+} states into the Cu^{1+} species that are less emissive due to the need for their "activation" by the capture of photogenerated holes.

Recently, toxicity and environmental concerns have led to strict regulations around the well-known classes of cadmium- and lead-based chalcogenide systems, which has boosted the interest in heavy-metal-free alternatives, such as I–III–VI_2 ternary NCs featuring technologically interesting optical properties, such as size-tunable band-gap from visible to NIR,[286-288] intense broadband absorption[289,290] and efficient Stokes-shifted

luminescence.[147,291-293] In addition, they can be fabricated in large quantities via high-throughput, non-injection techniques using inexpensive precursors.[294] NCs of $CuInS_2$ (CIS), $CuInSe_2$ (CISe), and their alloys $CuInSe_xS_{2-x}$ (CISeS) have been successfully used in photocatalysis,[295] sensing,[296] and bioimaging,[297-299] as well as in photonic devices such as LEDs,[300,301] solar cells[302-308] and, more recently, reabsorption-free luminescent solar concentrators.[147,309-311] Because of its technological relevance in photon-management and lighting applications,[312,313] particular attention has been devoted to the elucidation of the origin of the broad,[314,315] strongly Stokes-shifted photoluminescence (PL).[147,316] Recent interpretations suggest the partial forbiddances of optical transitions between the electron and hole ground states due to the tetragonal symmetry of the crystal lattice[317] or exciton self-trapping processes[318] as possible mechanisms. A more commonly accepted emission mechanism, however, is radiative recombination of a photoexcited band-edge electron and a hole residing in an intragap state[147,292,315,316,319-325] often associated with off-stoichiometric effects that have been shown to enhance the emission efficiency.[286,320,326,327]

To date, the nature of the intragap state in CIS NCs is not fully understood and is often related[291,316,328] to optically active centres responsible for the non-resonant long-lived PL in copper-doped II–VI semiconductors whose optical and magnetic properties are very similar to those of ternary I–III–VI compounds.[194,215-217,316,329-332] In copper-doped II–VI semiconductors, the *3d* states of the Cu impurities introduce a fairly deep intragap acceptor level near the NC valence band (VB).[265,333,334] The crystal-field of the host lattice splits the degeneracy of the *3d* state into two distinct sublevels within the gap, the higher in energy being 6-fold degenerate and conventionally labelled as *t*, whereas the lower level is 4-fold degenerate and labelled *e*.[265,333] The Fermi energy of the NC determines the occupancy of these states: when the Fermi level is above them, the *3d* shell is completely filled, which corresponds to the +1 oxidation state of Cu with electronic configuration (Ar)$3d^{10}$. When the Fermi level is below the *t*-state, the electronic configuration becomes (Ar)$3d^9$, corresponding to the +2 oxidation state of Cu.[334] In this latter case, the impurity acts as a paramagnetic acceptor state, which can radiatively capture a conduction band (CB) electron without the need for a photogenerated hole.[194,230,335,336] On the contrary, capture of a VB hole by the dopant is necessary in order to enable the radiative decay of a CB electron via a Cu^{1+} centre.[222,337] Notably, while spectro-electrochemistry (SEC) experiments pointed to a major role of Cu^{2+} species in the emission process of Cu:ZnSe/CdSe NCs, magnetic circular dichroism (MCD) studies on the same systems revealed that photomagnetism due to *sp-d* spin-exchange coupling in NCs with +2 copper impurities undergoes strong (up to 100%) enhancement upon UV illumination, suggesting that diamagnetic Cu^{1+} dopants can be photoconverted into paramagnetic Cu^{2+} centres.[217]

The photophysical and structural similarities between Cu-doped II–VI NCs (i.e., CdSe, ZnSe)[318] and I–III–VI_2 NCs, which feature a unit cell composed of two zinc-blende unit cells distorted along the *c*-axis,[338-340] suggest a similar recombination mechanism also for CIS (or CISeS in general) NCs. Notably, in these NCs the intragap recombination centre seems to be a "native" defect, as indicated by the consistency of the optical features exhibited by ternary NCs obtained via different synthetic techniques.[290,326,328,341-343] Compositional analyses by X-ray

photoelectron spectroscopy[342] indicate that the main oxidation state of copper in CIS NCs and their alloys is +1. Nevertheless, the exact ascription of the copper state responsible for the PL of I–III–VI_2 is still debated with some studies indicating Cu^{1+} as the emissive centre,[290,337] whereas other studies point to the presence of small amounts of paramagnetic Cu^{2+} defects (complemented, e.g., by Cu vacancies, V_{Cu}, for charge neutrality)[316] in the NC lattice as the species responsible for the optical and magnetic properties of CIS NCs.[147,217,316] A more recent theoretical study of wurtzite CIS NCs by Macdonald and co-workers suggests that interstitial Cu^0 defects introduce an intragap acceptor state with the localization energy comparable to the experimentally observed Stokes shift.[321] While such charge-neutral Cu species might occur in CIS NCs, a considerable amount of literature points toward the prevailing role of substitutional Cu^{1+} (might occur as an anti-site $CuIn^{1+}$–$InCu^{3+}$ pair) and Cu^{2+} (paired, e.g., with V_{Cu}) defects[315,316,326,339,344-346] in defining photophysical properties of CIS NCs. In fact, several recent studies seem to suggest that the radiative decay centres are likely Cu^{2+} species at least in some of the samples where the position of the Fermi level favors this type of states.[315,316,347] Furthermore, similar to previous observations for Cu:doped II–VI NCs, Cu^{1+} states can in principle be photoconverted to Cu^{2+} centres upon capture of a VB hole. In this case, the interplay between the hole capture by the Cu^+ defects and surface traps would determine the sensitivity of the emission efficiency to external hole withdrawing agents. The scenario of Cu^{2+}-mediated luminescence in CIS NCs (due to either pre-existing or photoconverted Cu^{2+} states) is, for example, supported by recent spectroscopic investigations,[291] showing that the main factor controlling the PL efficiency in CIS NCs is nonradiative trapping of photoexcited electrons, whereas hole trapping does not appreciably affect the PL quantum yield. Another piece of evidence in favor of the Cu^{2+} emission mechanism is a quantitative similarity in light-emission properties (including PL spectral and relaxation characteristics) between CIS NCs and Cu-doped ZnSe NCs.[316] The Cu^{2+} character of emissive species in the latter system was indicated by the fact that intragap PL was enhanced when NCs were treated with hole scavengers.[215]

To address this gap, I combine temperature-controlled PL studies and SEC methods to elucidate the emission mechanism in I–III–VI_2 NCs and shed light on the nature of the intragap state involved in the radiative recombination process. I demonstrate that by tuning the position of the Fermi level through the application of an electrochemical (EC) potential, I alter the occupancy of intragap states and thereby reversibly change the NC's emission intensity by promoting/hindering selective carrier trapping in defect sites. The effect of the EC potential is reduced in core/ shell CIS/ZnS NCs compared to core-only structures, which is an expected consequence of suppressed extrinsic nonradiative decay processes due to improved electronic passivation of the CIS–core surfaces by a wide-gap shell[147] that effectively reduces the abundance of intragap traps. Our data show that the PL efficiency of unshelled NCs is strongly enhanced upon raising the Fermi level, which leads to filling (passivation) of electron trapping sites. Because the same conditions lead to activation of additional hole trapping states, this observation indicates that enhanced trapping of photogenerated holes does not diminish the PL efficiency, pointing toward a recombination pathway involving either a pre-existing hole-like Cu^{2+} intragap state or a photogenerated acceptor produced via hole trapping by Cu^{1+} defects occurring on a faster time scale than hole trapping by EC activated surface defects.[194,316] Furthermore, both core-only and core/shell NCs with passivated surfaces show a drop in the

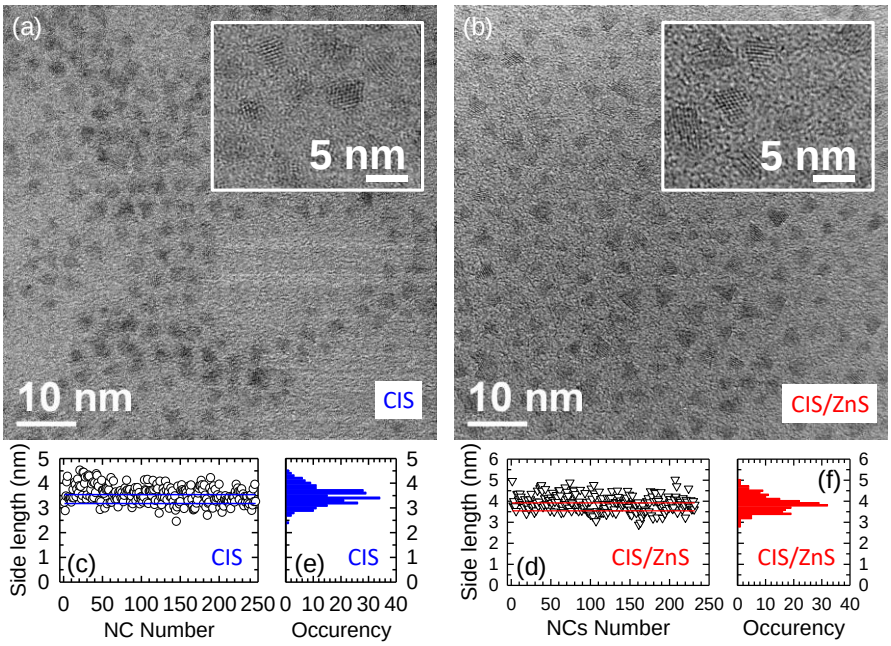

Figure 6.1 Transmission electron microscopy (TEM) images of an ensemble of (a) CIS and (b) CIS/ZnS NCs. Side length of ~250 (c) CIS and (d) CIS/ZnS NCs as extracted from the TEM images in panel 'a' and 'b', and respective statistical analyses of the side length occurrences with 0.1 nm steps. The average sizes of (e) CIS and (f) CIS/ZnS NCs are 3.5 ± 0.4 nm and 3.9 ± 0.4 nm, respectively.

PL intensity at the highest negative potentials, which might be associated with either direct injection of electrons into the NC conduction band, which activates nonradiative Auger recombination,[60,348] or EC conversion of the Cu^{2+} states into the Cu^{1+} species that are less emissive due to the need for their "activation" by the capture of photogenerated holes.[215] Temperature-controlled PL measurements on both shelled and unshelled NCs point to the presence of an intrinsic thermally assisted nonradiative decay process with similar activation energies in both structures. The suppression of this nonradiative pathway at cryogenic temperatures leads to a two-fold enhancement of the PL quantum yield. Finally, in order to rationalize the SEC observations in terms of competition between the involved recombination channels, I develop a model which links the PL efficiency to the occupancy of intragap traps and also accounts for the possibility of either direct injection of electrons into the NC conduction band or EC reduction of Cu^{2+} centres to Cu^{1+}.

6.1 - Optical Properties of Core-Only and Core/Shell CIS/ZnS Nanocrystals

The core-only and core/shell CIS/ZnS NCs with ~4 nm side length were synthesized following the route described in ref. [341]. Briefly, heavy-metal-free CIS NCs were produced by dissolving copper(I) iodide and indium(III) acetate in a mixture of 1-dodecanethiol and oleylamine in a round-bottomed flask, and the mixture was degassed for 30 mins. The reaction flask was then heated to 230 °C for ~30 mins. The ZnS shell of CIS/ZnS NCs has been grown through exposure of the CIS NCs to a solution of zinc-oleate at elevated temperature, which formed the shell by cation exchange. The transmission electron micrographs are reported in Figure 6.1, together

with the respective statistical analyses of the average side length of the NCs. The optical absorption spectrum (acquired as in Section 2.2) and the characteristic Stokes-shifted PL of core-only CIS and core/shell CIS/ZnS NCs are shown in Figure 6.2a together with the respective PL excitation (PLE) spectra collected at the emission maximum (both PL and PLE experiments have been performed as described in Section 5.1). The spectra of the core/shell NCs are slightly blue-shifted with respect to the respective core-only NCs as typically observed for the situation when the shell growth occurs via cation exchange, which leads to the effective reduction of the emissive core accompanied by the increase in the degree of spatial confinement.[292] In both cases, the PLE spectra follow nearly perfectly the respective absorption profile, which confirms that the PL is excited by intrinsic electronic transitions of the NCs. The PL quantum yield, as measured with an integrating sphere, is Φ_{PL} = 5 ± 1% and Φ_{PL} = 35 ± 3% for the core-only and the core/shell NCs, respectively. The increase in the PL efficiency in the case of the core/shell sample indicates the effectiveness of electronic passivation of the core surface by a wide-gap

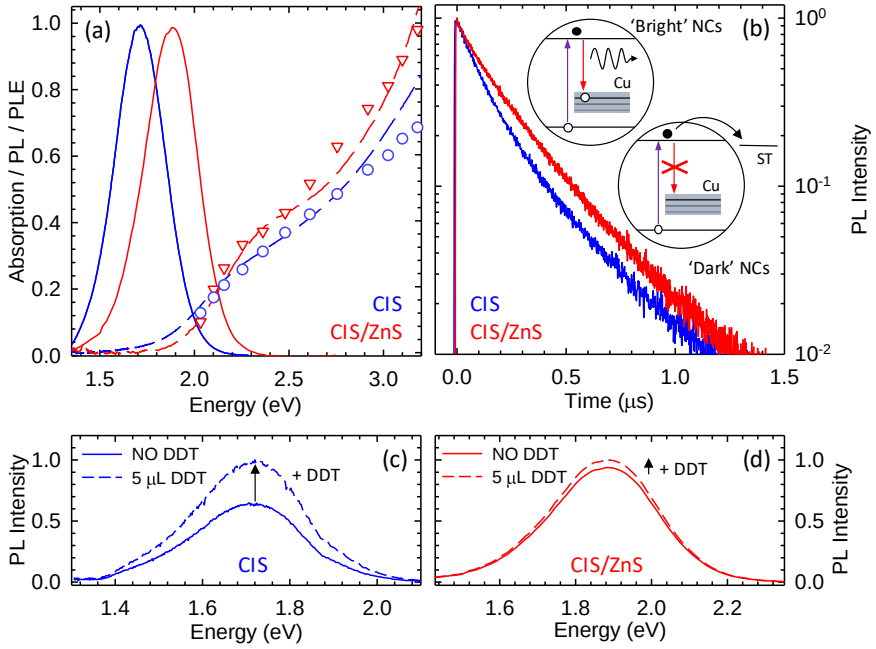

Figure 6.2 (a) Absorption (dashed lines) and photoluminescence (PL) spectra (solid lines) of CIS core-only (blue lines) and core/shell CIS/ZnS (red lines) NCs in toluene. The PL excitation (PLE) spectra are shown as blue circles for CIS NCs (collected at 1.7 eV) and red triangles for CIS/ZnS NCs (collected at 1.9 eV). (b) PL decay traces of the same solutions collected at the respective PL maxima. Inset: A simplified structure of the band-edge electronic states in CIS NCs responsible for optical absorption and PL. Light absorption is dominated by optical transitions between intrinsic quantized states, while the PL arises from the radiative capture of a band-edge electron by an intragap state associated with a Cu-related defect acting as the emission centre. The absence of electron trapping channels leads to "bright" NCs whereas fast electron-transfer to surface traps (ST) leads to nonemissive "dark" particles in the ensemble. PL spectra of (c) CIS NCs and (d) CIS/ZnS NCs in the absence (solid lines) and in the presence (dashed lines) of the 1-dodecanethiol, DDT (5 μL DDT per mL solution), a known hole scavenger. The PL spectra of both samples are normalized to their value after the addition of DDT. All PL measurements were performed using pulsed 3.05 eV excitation (per-pulse excitation fluence is 0.5 μJ/cm^2).

ZnS layer which creates a type-I energetic barrier.[147,315,349] As shown in Figure 6.2b, the ~7-fold enhancement of Φ_{PL} upon shelling the CIS NCs with ZnS occurs without significant changes in the PL decay dynamics that for both systems is slightly multiexponential in agreement with previous results.[147,286,291,292] Time-resolved PL measurements were carried out using ~70 ps pulses at 3.05 eV from a Picoquant LDH-P pulsed diode laser. The emitted light was collected with the same experimental setup described in Section 2.3 for the core PL of DiB NCs, that gives a time resolution of ~600 ps. The effective PL lifetimes, extracted as the time for which the PL signal drops by a factor of e, are ~200 and ~175 ns for the core/shell and core-only NCs, respectively. This indicates that the deposition of the ZnS shell suppresses rapid (unresolved in our measurements) nonradiative surface trapping that occurs prior to radiative decay, while leaving the spatial overlap between the electron and hole wave functions nearly unaltered. I note that surface trapping could, in principle, affect both "hot" and relaxed band-edge carriers, however, a close match between the PLE and the absorption spectra (Figure 6.2a) indicates that the trapping process involves primarily carriers close to the NC's band-edges. The lower emission yield of the core-only CIS NCs sample with respect to core/shell particles is, therefore, likely due to a larger fraction of non-emissive ("dark") NCs, in which electron surface trapping outpaces radiative decay, compared to the fraction of emissive "bright" NCs that do not contain "fast" electron traps (inset of Figure 6.2b).

SEC experiments reported in the following sections can also be explained using the above two sub-ensembles model. In fact, they demonstrate that the application of an EC potential reversibly converts "dark" NCs into "bright" ones and vice versa by passivating/activating electron surface traps. In II−VI NCs doped with Cu^{2+}, PL quenching has been mostly ascribed to rapid electron trapping,[215] while trapping of VB holes has been considered to have a minor role due to the ability of a Cu^{2+} acceptor state to directly capture a CB electron via a radiative transition.[194] Indeed, the addition of 1-dodecanethiol (DDT), which has been observed to quench the PL from CdSe NCs[350] due to rapid extraction of photogenerated VB holes, leads to brightening of Cu:ZnSe/CdSe NCs resulting from the passivation of electron accepting surface defects.[194] A similar behavior has been also observed for CdTe NCs,[350,351] whose band-edge holes reside above the redox level of DDT and thus cannot be reduced by it. Interestingly, similarly to Cu-doped NCs, the exposure of CIS NCs to DDT enhances their PL efficiency, although their VB energy (E_{VB} ~ −6.26 eV)[294,351,352] is comparable to CdSe NCs (E_{VB} ~ −6.1 eV).[350,353] In Figure 6.2, I display the PL spectra of both unshelled (panel 'c') and shelled (panel 'd') samples recorded in the absence and in the presence of DDT (5 μL in 1 mL of NCs solution). The addition of DDT to core-only CIS NCs leads to strong 60% enhancement of the PL efficiency suggesting that, as in Cu-doped II−VI NCs, the main emission intensity-limiting mechanism is electron trapping,[291] which becomes suppressed upon exposure to electron-donating DDT molecules.[350] On the other hand, the absence of PL quenching due to rapid hole withdrawal is indicative of an emission process involving an intragap acceptor state, which is occupied with a pre-existing hole, or act as a very fast trap for photogenerated VB holes outcompeting hole extraction by DDT. These two types of behaviours can be expected, respectively, for Cu^{2+} and Cu^{1+} intragap defects. The addition of DDT also improves the PL efficiency of CIS/ZnS NCs, although, in this case, the enhancement is less than 10%

(Figure 6.2d). The diminished effect of electron-donating species in this case is due to already effective passivation of surface electron traps by the ZnS layer.

6.2 - Temperature-Controlled Photoluminescence Experiments

To quantify the effect of nonradiative decay channels in our NCs and to investigate the intrinsic radiative decay rates in the "bright" particles in both the CIS and CIS/ZnS NCs ensembles, I perform temperature-controlled PL experiments by mounting a drop-casted film of the NCs samples inside a liquid nitrogen cooled cryostat with optical access. In Figure 6.3, I report the PL spectra and the decay curves at decreasing temperature of CIS and CIS/ZnS NCs. Both samples show monotonic enhancement of the emission intensity from T = 300 K to T = 70 K.

At any temperature, both PL dynamics are slightly multiexponential, as typically observed for CIS NCs.[147,286,291,292] At T = 300 K, the effective decay lifetime is $\tilde{\tau}$ = 200 ns (corresponding to an

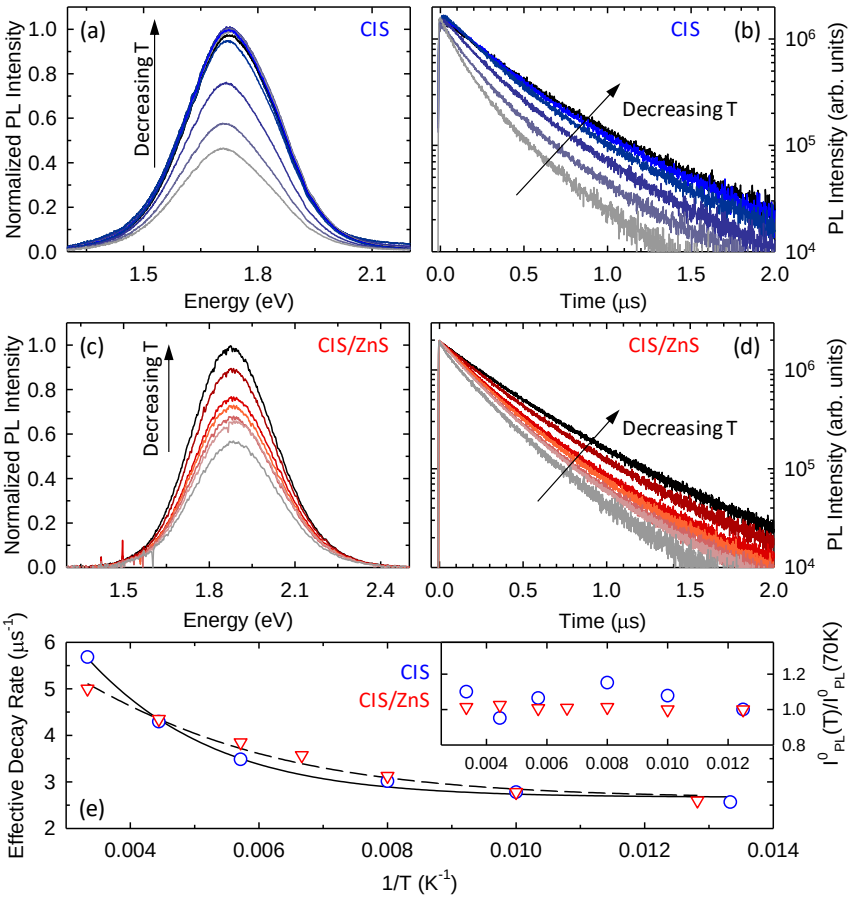

Figure 6.3 (a,c) PL spectra and (b,d) time-resolved PL traces for core-only CIS NCs and CIS/ZnS as a function of decreasing temperature as indicated by the arrows. The PL spectra are normalized to their value at T = 77 K. (e) Effective decay rates ($\tilde{k}$) extracted from the PL traces in panels b and d as a function of T^{-1} (blue circles for CIS NCs and red triangles for CIS/ZnS). The respective fits to Eq. (6.1) are shown as a solid line for the CIS NCs and as a dashed line for CIS/ZnS NCs. The zero-delay PL intensities normalized to their respective values at 70 K are shown in the inset. The same color scheme applies throughout the figure.

effective decay rate $\tilde{k} = 1/\tilde{\tau} = 5\ \mu s^{-1}$) and $\tilde{\tau} = 175$ ns ($\tilde{k} = 5.7\ \mu s^{-1}$) for CIS and CIS/ZnS NCs, respectively. In both cases $\tilde{\tau}$ increases to ~370 ns ($\tilde{k} = 2.7\ \mu s^{-1}$) at T = 70 K. Importantly, as evident from Figure 6.3b,d and additionally highlighted in the inset of Figure 6.3e, no appreciable effect of temperature is observed for the zero-delay PL intensity, indicating that ultrafast electron trapping is virtually temperature-independent.[354] This further suggests that the relative fraction of "bright" versus "dark" NCs in the ensemble is unaltered by temperature. On the other hand, changes in temperature affect the decay dynamics in the sub-ensemble of "bright" NCs. This observation, together with the strong resemblance between the temperature dependent trends observed for core-only and core/shell NCs, suggest that the nonradiative process competing with radiative decay might involve phonon-assisted trapping of electrons at internal structural defects. Accordingly, the effective decay rates of CIS and CIS/ZnS NCs follow a very similar trend with decreasing temperature. The evolution of the effective decay rate is shown in Figure 6.3e together with the respective fit to the equation: $\tilde{k} = k_{RAD} + k_{NRAD}(T)$, that neglects ultrafast surface electron trapping and describes the nonradiative decay rate by the standard displaced harmonic oscillator model:

$$k_{NRAD}(T) = A \cdot \exp(-\frac{E_A}{k_B T}) \qquad (6.1)$$

Through this fit, I obtain essentially the same effective radiative decay rate (k_{RAD}) for CIS and for CIS/ZnS NCs ($k_{RAD} = 2.58 \times 10^6\ s^{-1}$ and $k_{RAD} = 2.61 \times 10^6\ s^{-1}$, respectively) and activation energies for the nonradiative decay of 56 meV for CIS NCs and of 40 meV for CIS/ZnS NCs. Using the obtained radiative and nonradiative decay rates, I finally use the equation $\Phi_{PL,BRIGHT} = k_{RAD}/\tilde{k}$ to quantify the room temperature PL efficiency of the "bright" NCs in the two ensembles that is found to be $\Phi_{PL,BRIGHT}$ ~50% for both core-only and core/shell CIS/ZnS NCs. Considering that the overall PL quantum yields are 5 ± 1% and 35 ± 3% for the CIS and the CIS/ZnS sample, respectively, this indicates that the fractions of "bright" particles in the core-only sample is ~10%, and it increases to 70% upon shelling.

6.3 - Spectro-electrochemistry Experiments

To gain a deeper insight into the effect of intragap states on the radiative and nonradiative recombination in CIS and CIS/ZnS NCs, I have performed SEC measurements, wherein I tune the Fermi level in a controlled and reversible fashion through the application of an EC potential.[60,215,355] Figure 6.4a shows a schematic depiction of the experimental setup used in the SEC measurements, which has been thoroughly described in Section 5.2. A working electrode comprises an ITO-coated quartz substrate covered by a film of sintered ZnO particles (~50 nm diameter) and a thin layer of NCs; silver and platinum wires are used as reference- and counter-electrodes, respectively. I start the measurements by applying a negative EC potential, which corresponds to raising the Fermi level in the NC film leading to progressive passivation (activation) of the surface electron (hole) traps (ET and HT in Figure 6.4a, respectively). In Figure 6.4b, I report the complete set of PL spectra of CIS NCs under application of a negative EC potential (V_{EC}) scanned from 0 to −2.5 V and then back to 0 V. To quantify the effect of the EC potential on the PL intensity of both the core and core/shell NCs, in Figure 6.4c I plot the respective integrated PL intensities as a function of the EC potential normalized to their values

at V_{EC} = 0 V. In the case of CIS NCs (blue circles, Figure 6.4c), no noticeable changes in the PL intensity occur at the initial stage of the potential ramp (up to V_{EC} = −1 V). This is common in SEC measurements of colloidal nanostructures that use ITO/ZnO electrodes[116,215,279,355] to suppress PL quenching by energy- and/or charge-transfer from the NCs to the ITO.[355,356] The introduction of the additional ZnO spacer along with the presence of insulating surface ligands

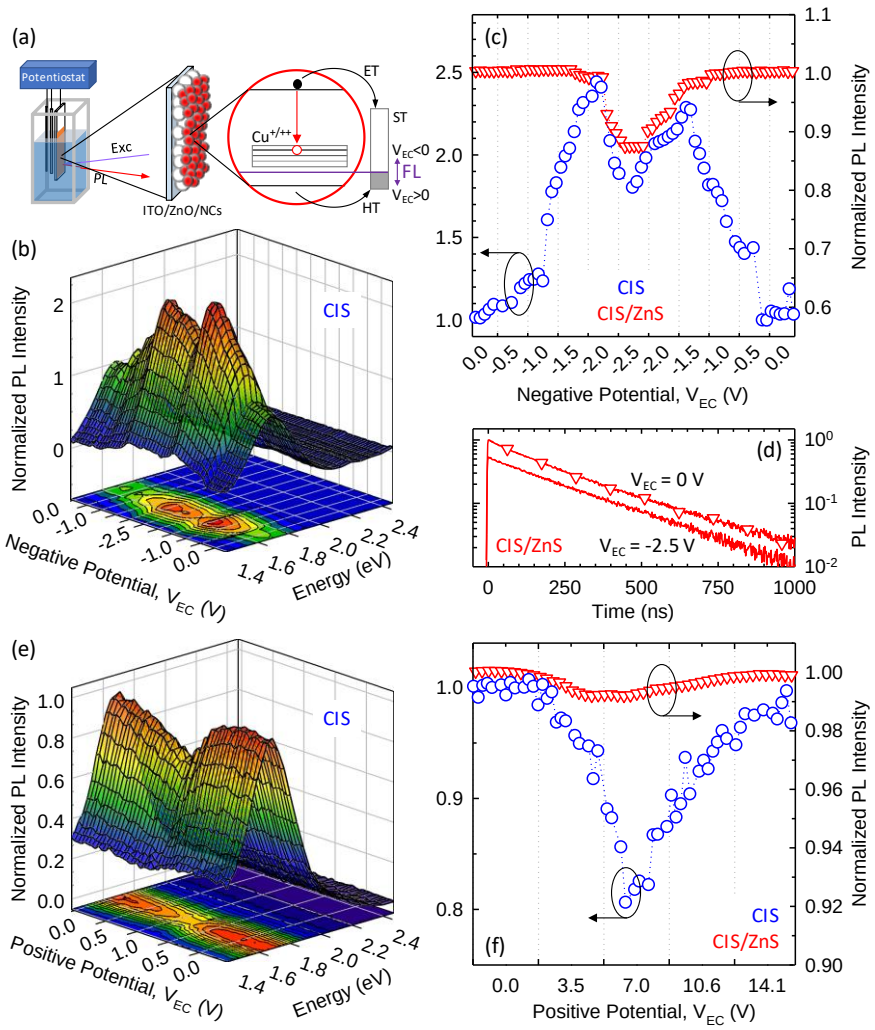

Figure 6.4 (a) Schematics of the SEC setup and the effect of the EC potential on the PL intensity of CIS NCs due to filling/emptying of surface traps (ST) in response to changes in the position of the Fermi level (FL; purple line). (b) Series of core-only CIS NCs PL spectra (5 s acquisition/frame) during a stepwise scan of the negative EC potential from V_{EC} = 0 to −2.5 V (0.5 V step, 30 s). (c) Integrated PL intensity of CIS NCs (blue circles, left y-axis) and CIS/ZnS NCs (red triangles, right y-axis) under applied negative EC potential based on the spectra in panel b and Figure S3. Both dependences are normalized to their values at V_{EC} = 0 V. (d) Time-resolved PL traces of CIS/ZnS NCs at V_{EC} = 0 and −2.5 V. (e) Series of PL spectra (5 s acquisition/frame) of CIS NCs during a stepwise scan of the positive EC potential from V_{EC} = 0 to 1 V (0.5 V step, 30 s). (f) Integrated PL intensities for CIS NCs (blue circles, left y-axis) and CIS/ZnS NCs (red triangles, right y-axis) as a function of applied positive EC potential. Both dependences are normalized to their values at V_{EC} = 0 V. All measurements are performed using pulsed 3.05 eV excitation with fluence of 10 nJ/cm^2.

can lead to an appreciable attenuation of the actual shift of the Fermi level compared to the nominal applied EC potential.[357] At negative potentials above V_{EC} = −1 V, I observe strong PL brightening as indicated by ~150% enhancement of the PL intensity for V_{EC} = −2 V. The effect of the reductive EC potential is similar to that of the exposure to DDT (Figure 6.2c), which points to the similarity of the underlying mechanisms that in both cases involve gradual filling of electron trap sites on the NC surface, leading to the progressive increase in the fraction of "bright" NCs versus the "dark" non-emissive ones.

Accordingly, the PL decay dynamics shows an appreciable enhancement of its zero-delay intensity and only a minor change of the PL lifetime, which confirms that surface electron trapping is very fast (unresolved in these measurements) and occurs prior to radiative decay. Importantly, the concomitant activation of hole traps occurring for raising Fermi energy does not affect the PL intensity, indicating that in the studied CIS NCs the emission process is nearly independent of hole trapping. This is consistent with a scenario in which radiative recombination of CB electrons occurs via hole-like Cu^{2+} centres, either already present in the ground state (due, e.g., to sample off-stoichiometry) or induced by transient photooxidation of Cu^{+} sites by capture of VB holes occurring faster than nonradiative trapping by surface defects. Upon reaching a potential of −2 V, the trend in the dependence of the PL intensity versus V_{EC} reverses, and I observe a stepwise ~20% drop in the PL signal at V_{EC} = −2.5 V.

The core/shell CIS/ZnS NCs do not show initial electrochemically induced PL brightening (red triangles, Figure 6.4c) due to already effective passivation of surface electron traps by the ZnS shell, as was discussed earlier in the context of experiments involving titration with DDT. However, as in the case of core-only structures, application of a strongly reducing potential ($|V_{EC}| > 2$ V) also leads to the appreciable (~15%) PL quenching. For both the core-only and core/shell NCs, I observe a full recovery of the initial PL intensity upon returning back to the zero EC potential, suggesting that the observed PL quenching is not caused by any permanent chemical degradation of the NCs.

The sudden drop in the PL intensity at high negative EC potentials is consistent with previous observations for Cu-doped II–VI NCs[215] in which it was ascribed to the EC-induced conversion (reduction) of Cu^{2+} centres into Cu^{+} in the NCs sub-ensemble in which the position of the Fermi level favors the incomplete filling of the copper *d* electronic shell. Cu^{+} species can participate in the radiative decay only after capturing a photogenerated VB hole, a necessary step that is rendered less efficient under increasing reductive potentials due to the increase in the abundance of active hole traps competing with the Cu^{1+} centres for the photoinjected hole. As a result, a progressive Cu^{2+}-to-Cu^{1+} conversion for increasingly negative V_{EC} can indeed lead to PL dimming without changes in the PL decay dynamics independently of the original oxidation state of the Cu ion. This picture seems to be consistent with observations for CIS/ZnS NC reported in Figure 6.4d. Specifically, the recorded PL time transients show a drop of the zero-delay PL intensity upon increasing V_{EC} from 0 to −2.5 V, however, the PL lifetime remains unaltered.

While the above scenario is plausible, there is also an alternative (or additional) mechanism, which can lead to PL dimming at high negative potential. This mechanism is direct electron

injection into the NC conduction band, which would activate nonradiative Auger recombination through the so-called negative trion pathway,[348] that is, the process where the energy released in the exciton recombination is transferred to another electron coexisting in the NC. Such a process, occurring between 30 and 300 ps in CIS NCs,[346,358] would render a portion of the NC population non-emissive, resulting in early time dimming of the PL amplitude unresolved in the PL decay measurements in Figure 6.4d, while leaving the dynamics of emissive NCs unmodified. The uncertainty in the exact nature of PL quenching process relates to the uncertainty in the absolute magnitude of the Fermi level shift for a given EC potential. Specifically, the interpretation of experimental data of ref. [215] was made under the assumption that the division coefficient between an applied V_{EC} and the resulting shift of the Fermi level was large ($f \sim 20$), therefore, despite large variations in V_{EC}, the actual modulation of the Fermi level was considerably smaller. However, for a highly conductive ZnO layer the division factor can become greater, which might allow for electron injection into the NC under sufficiently larger negative EC potentials. For example, this condition has been realized in SEC experiments on undoped CdSe/CdS NCs, in which direct injection of electrons in the NC conduction band was achieved at V_{EC} corresponding to half the NC band-gap energy ($f \sim 1$),[161,162] consistently with the midgap position of the Fermi level in intrinsic semiconductors. The possibility of this process along with the Cu^{2+}-to-Cu^{1+} conversion will be discussed in more quantitative terms in the next section where I conduct modeling of the effect of the EC potential on the PL intensity. On the other hand, since the applied EC potentials are of the order of a few Volts, I exclude exciton dissociation by electric field[359,360] as a potential cause of the observed PL drop.

I next investigate the effect of a positive EC potential on the two NC systems. In Figure 6.4e, I report the complete set of PL spectra of CIS NCs under positive EC potential up to V_{EC} = +1 V and, to highlight the effect of lowering the Fermi level, in Figure 6.4f I show the integrated PL intensity as a function of the cyclic stepwise scan of the positive EC potential. Between V_{EC} = 0 V and V_{EC} = +0.25 V, I observe no measurable modulation of the PL intensity for both samples. Upon increasing the potential to V_{EC} = +1 V, the PL intensity drops by ~20% for the core-only CIS NCs and is nearly constant (<1% drop) for the CIS/ZnS systems (note the different y-scales for core-only and core/shell NCs). This behavior is a continuation of the trend observed for the negative V_{EC} and it is consistent with the progressive activation of intragap traps under oxidative potentials that deplete the CIS NCs of photogenerated electrons to a larger degree than in shelled CIS/ZnS NCs. Accordingly, the early time PL dynamics of CIS NCs becomes faster upon raising the positive potential to V_{EC} = 1 V. In contrast, the PL dynamics of CIS/ZnS NCs is essentially unaffected by the positive EC potential. As in the case of the negative potential, the PL intensity of both types of samples fully recovers when the EC potential is brought back to V_{EC} = 0 V, indicating no permanent oxidation of the NC surfaces.

6.4 - Model for Analyzing the Spectro-electrochemical Responses

To rationalize the SEC data, I use a model that links the total PL efficiency to the occupancy of intragap electron traps that can be activated (passivated) by lowering (raising) the Fermi level through the application of an EC potential. The scheme of the decay channels determining Φ_{PL} is depicted in the top panel of Figure 6.5a, where electron trapping (rate k_{ET}) takes place much faster than radiative capture of photogenerated electrons by intragap hole-like states

(rate k_{Rad}); the latter process competes with a nonradiative thermal recombination process (rate k_{NRad}) as discussed in temperature-controlled PL measurements in Figure 6.3.

Because hole trapping plays a minor role in the emission process in our NCs, as it is inconsequential for dots with ground state Cu^{2+} sites and is arguably slower than hole capture by emissive centres in dots with prevailing Cu^{+} defects, I neglect this process in our SEC model. To account for the effect of the EC potential on the occupancy of surface traps, I assume that the traps are distributed in energy across the NC ensemble forming a "trap band" with width N_0. I

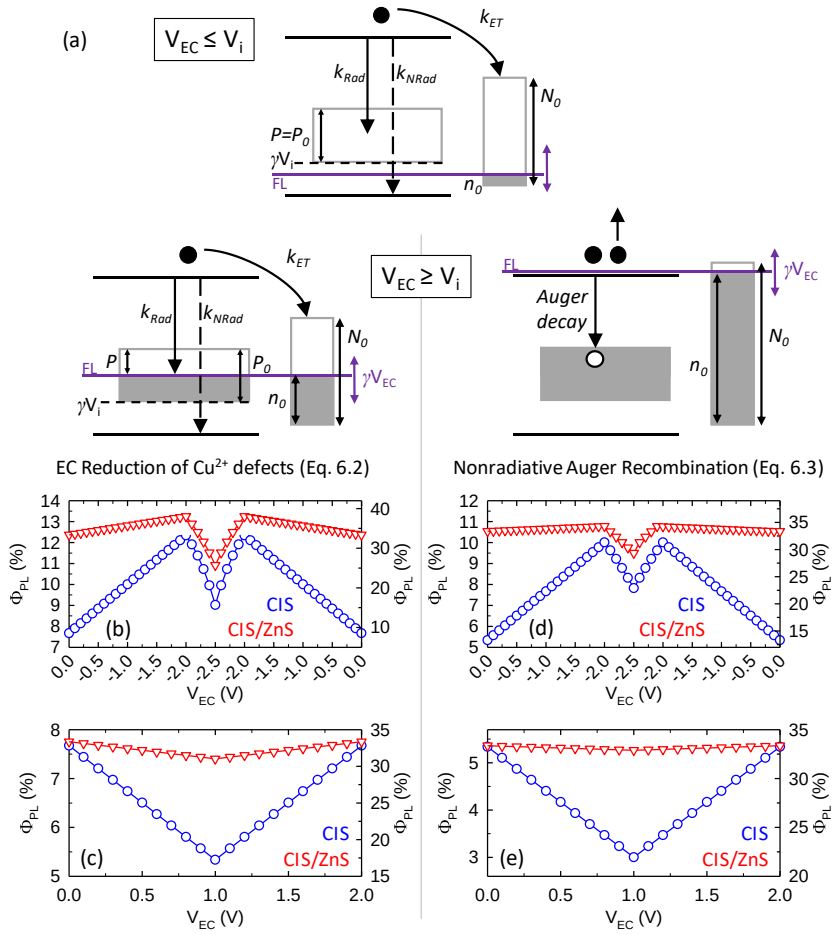

Figure 6.5 (a) Diagram illustrating the model used to describe the effect of the EC potential on the PL quantum yield of CIS and CIS/ZnS NCs via filling/emptying of carrier traps at the NC surface (right side of the NC). The Fermi level (FL) is depicted as purple line. For negative EC potentials larger than −2 V, two scenarios are possible depending on the attenuation factor between the applied potential and the shift of the FL. For high attenuations (γ = 5, lower left panel) leading to moderate shift of the NC FL, direct electron injection results in EC conversion of Cu^{2+} defects into less emissive Cu^{+} centres. For negligible attenuation factor (γ = 1, lower right panel), the FL reaches the NC conduction band leading to direct injection of electrons in the NC quantized states. Activation of nonradiative Auger recombination through the negative trion pathway lowers the PL efficiency. The calculated trends following the different routes of the PL intensity for CIS (blue circles, left y-axes) and CIS/ZnS NCs (red triangles, right y-axes) normalized to their value at V_{EC} = 0 V for varying negative and positive EC potentials are shown in (b) and (c), respectively.

also assume that the NCs are characterized by a common Fermi level, which determines the trap occupancy (n_0 per individual NC) in the absence of photoexcitation. The rate of electron trapping is determined by the fractions of "dark" (F_D) and "bright" (F_B) NCs that are connected to V_{EC} by $F_D = (N_0 - n_0 + \gamma V_{EC})/N_0$ and $F_B = 1 - F_D$, where γ is the attenuation factor expressed in units of [V^{-1}] between the applied V_{EC} and the resulting shift of the Fermi level. The model further considers the availability of intragap states for radiative decay of photogenerated electrons, which, consistently with the broad emission line width of CIS NCs[215,314] are described through an "acceptor band". Within the scenario of direct electron injection in intragap defects leading to EC $Cu^{2+} \rightarrow Cu^{+}$ reduction that would imply a strongly attenuated V_{EC} (lower left panel in Figure 6.5a), the width of such acceptor band, P, is assumed constant ($P = P_0$) for any V_{EC} below the injection potential V_i, which corresponds to the situation in which the Fermi level reaches the lowest-energy Cu^{2+} state under negative bias. For larger negative V_{EC}, electrons are injected directly into the NC intragap states, progressively reducing their number according to $P = P_0 - \gamma\beta(V_{EC} - V_i)$, where the term β expresses the injection efficiency of electrons in the NCs across the dielectric barrier imposed by the organic ligand shell.

Given these considerations, the total PL quantum yield can be expressed as

$$\Phi_{PL}(V_{EC}) = \frac{P}{P_0} * \left[F_B \frac{k_{Rad}}{k_{Rad} + k_{NRad}} + F_D \frac{k_{Rad}}{k_{Rad} + k_{NRad} + k_{ET}}\right] \qquad (6.2)$$

On the other hand, for negligible attenuation factors, the FL would reach the NC conduction band leading to direct injection of electrons in the NC quantized states (lower right panel in Figure 6.5a). In this case, the dimming of the PL intensity at high negative potentials is explained by the activation of efficient nonradiative Auger recombination ($\Phi_{AR} \sim 1$)[358] without invoking direct reduction of hole-like Cu^{2+} defects to less emissive Cu^{+}. Within this model, the total PL quantum yield can be expressed as

$$\Phi_{PL}(V_{EC}) = \varphi * \left[F_B \frac{k_{Rad}}{k_{Rad} + k_{NRad}} + F_D \frac{k_{Rad}}{k_{Rad} + k_{NRad} + k_{ET}}\right] \qquad (6.3)$$

where the term φ is assumed to be unity for $V_{EC} < V_i$, and $\varphi = 1 - \gamma\beta(V_{EC} - V_i)\Phi_{AR}$ for $V_{EC} \geq V_i$, which describes the progressive reduction of the population of photoexcited NCs in the ensemble due to the activation of efficient Auger recombination outpacing both radiative decay and electron trapping and thus affecting F_D and F_B equally. It is worth noting that Eq. 6.2 and 6.3 are equivalent for $V_{EC} < V_i$ and both describe the PL tuning by passivation/activation of surface traps. On the other hand, for $V_{EC} \geq V_i$ the two equations describe the possible quenching mechanisms in two distinct ways.

To illustrate the model, I use both Eq. 6.2 and 6.3 to calculate the evolution of Φ_{PL} as a function of the EC potential of both CIS and CIS/ZnS NCs using the experimental k_{RAD} and k_{NRAD} and a set of parameters chosen for matching the experimental Φ_{PL}-values of both systems at $V_{EC} = 0$ V (5% and 35%, respectively, Table 6.1). The results of the simulations under both negative and positive V_{EC} are reported in Figure 6.5b,c. Our semiquantitative model, which does not consider voltage-dependent interface polarization or capacitive effects in the multilayer ITO/ZnO/NCs structure leading to nonlinearity in the PL response versus V_{EC}, reproduces the main

Parameters used to reproduce the SEC data

	Cu^{2+}/Cu^{+} EC Reduction (Eq. (6.2))		Auger Recombination (Eq. (6.3))	
	CIS	CIS/ZnS	CIS	CIS/ZnS
k_R [ns^{-1}]	$2.7*10^{-3}$	$2.7*10^{-3}$	$2.7*10^{-3}$	$2.7*10^{-3}$
k_{ET} [ns^{-1}]	150	150	150	150
k_{NR} [ns^{-1}]	$3*10^{-3}$	$3*10^{-3}$	$3*10^{-3}$	$3*10^{-3}$
p_0	4	4	4	4
N_0	100	120	20	120
n_0	15	80	2	70
γ [V^{-1}]	5	5	1	1
β	0.6	0.4	0.6	0.3

Table 6.1 Complete set of parameters used to reproduce the experimental SEC data reported in Figure 6.4, panels c and f, with Eq. (6.2) and Eq. (6.3). I highlight that almost the same trends can be obtained with other sets of parameters. Therefore, the parameters shown must be considered indicative and not univocal and serve the purpose of showing that the observed experimental response can be reproduced with the proposed models.

experimental trends for both samples by taking into consideration that electron trapping is more effective in core-only CIS NCs than in core/shell CIS/ZnS NCs due to the larger number of available surface electron traps in the absence of the wideband-gap shell. According to both equations, upon applying a negative V_{EC}, the progressive filling of surface states with electrons increases the fraction of "bright" NCs in the ensemble, leading to a two-fold enhancement of Φ_{PL} of CIS NCs, for which electron trapping dominates the exciton decay process at V_{EC} = 0 V. On the other hand, the PL efficiency of CIS/ZnS NCs is essentially unaltered by the EC potential, which is in agreement with the experimental data in Figure 6.2 and 6.4 and confirms that the wide band-gap shell renders the majority of NCs in the ensemble "bright". When $V_{EC} \geq V_i$, Φ_{PL} of both samples decreases. In the case of γ = 5 V^{-1}, corresponding to strong attenuation of the EC potential (lower left panel in Figure 6.5a and Figure 6.5b), Eq. (6.2) predicts the progressively lower availability of intragap hole-like Cu^{2+} centres upon direct electron injection, which outpaces the brightening effect due to suppressed surface electron trapping and affects "bright" and "dark" NCs subpopulations equally. Such trend further indicates that the Cu^{2+} states in each NC have nearly the same energy. On the other hand, for γ = 1 V^{-1}, corresponding to no attenuation of the EC potential (lower right panel in Figure 6.5a and Figure 6.5c), Eq. (6.3) describes the observed dimming by activation of ultrafast Auger recombination through the negative trion pathway, lowering the overall population of emitting NCs. The model also reproduces the modulation of the PL intensity at positive V_{EC}, where a progressively lowered Fermi level activates electron traps in CIS NCs to a greater degree than in the core/shell system.

6.5 - Conclusion

In summary, I combined temperature-controlled PL and SEC experiments to investigate the recombination mechanisms in ternary CIS NCs. PL experiments as a function of temperature reveal that electron trapping at surface defects is not a temperature-activated process. On the other hand, intrinsic nonradiative decay, which competes with radiative capture of the CB electron by intragap Cu-related defects, is thermally activated and can be suppressed by cooling samples down to cryogenic temperatures. This channel is independent of the quality of surface passivation and is possibly associated with internal electron accepting defects. Tuning the Fermi level by the application of an EC potential modifies the occupancy of the intragap electron traps (likely surface related), which leads to pronounced changes in the emission intensity of core-only CIS NCs. The effects of the EC potential are less pronounced in CIS/ZnS NCs due to the reduced abundance of intragap defects. Both systems show darkening at high negative EC potentials without modifications of the respective PL decay dynamics. This effect can be explained by electron injection into the NC CB leading to activation of nonradiative Auger recombination. An alternative (or additional) mechanism for PL quenching under high negative V_{EC} is EC conversion of Cu^{2+} defects into Cu^{1+} species that are less emissive due to the need for capturing a photoexcited hole from the NC valence band, which competes with fast hole trapping by non-emissive defects activated at high negative EC potentials.

Conclusions

The fundamental physical mechanisms underlying the optical properties of colloidal NCs are often elusive and the experimental results could easily induce to misleading interpretations. Thanks to the wide range of optical experiments I had the chance to perform in Prof. Francesco Meinardi's optical spectroscopy laboratory and with the collaborations settled during the years of my PhD course, I had the unique chance to thoroughly investigate the open questions presented in the previous Chapters about the photophysics of last-generation colloidal NCs.

First, I demonstrated that, in core/shell CdSe/CdS NCs, the interface between the compositional domains plays a crucial role in the exciton recombination dynamics. It is therefore a further structural parameter that can be used to finely tune the optical properties. Specifically, I showed that an abrupt compositional interface effectively decouples the core and shell states, lengthening the relaxation time of the shell holes into the lower-energy states of the core and consequently activating emission from the shell states at low excitation fluencies already ($\langle N \rangle < 1$). Furthermore, the introduction of a small potential barrier between the core and the shell state is possible by growing a shell featured by two consecutive crystal structures. The introduction of this barrier prevents localization of multiple holes into the core (dynamic Coulomb blockade effect), further improving the shell emission efficiency and suppressing the nonradiative Auger recombination in the core.

Then, my research project has focused on doped NCs, which attracted attention of the scientific community because of their unprecedented optical properties. As a first step, I demonstrated that metal clusters (i.e. small molecules made of precise and monodisperse numbers of metal atoms) can be used as seeds for the nucleation in the reaction flask of the NC synthesis. Combining the results of optical, structural and elemental experiments, I showed that exactly one metal cluster is embedded in each NC, overcoming the intrinsic polydispersity that affects common stochastic doping routes. Secondly, I proved that resonant PL is a powerful tool to investigate the formation of polarons in magnetically doped NCs. Experimental access to this quasiparticle previously relied on ambiguous interpretations of details in non-resonant PL spectra and their time-resolved decay traces. In collaboration with Dr. Scott A. Crooker, I showed that, on the contrary, resonant PL experiments provide clear and unambiguous signatures of polaron formation, also allowing a quantitative estimation of the internal magnetic field induced by the magnetic spins. Monte Carlo simulations are also shown to confirm the experimental data. Finally, I focused on the role of silver as a dopant in II-VI semiconductor NCs. Despite silver belongs to the same group of the periodic table of copper, the former is much less known and understood than the latter. Copper is naturally stable in both +1 and +2 oxidation states, whilst silver, that is featured by a larger atomic radius, is mostly +1. By mean of combined optical spectroscopy, spectro-electrochemistry and magnetic circular dichroism experiments, I demonstrated that the nonmagnetic Ag^{+} ions can be photoconverted to the paramagnetic Ag^{2+} states thus switching on the magnetic activity of the doped NCs simply shining light on them. Importantly, at cryogenic temperatures, the

paramagnetic state persists for several minutes after it has been “written” with light, opening the way to new spin-based memories using colloidal NCs.

Finally, I shed light onto the exciton recombination dynamics of ternary $CuInS_2$ NCs that have recently drew attention as they overcome the environmental and toxicity issues that usually affects II-VI semiconductor NCs due to the presence of heavy-metals such as cadmium, mercury and lead. Despite their large applicative potential, the photophysical processes underlying their optical properties barely piqued researchers’ attention. By comparing the results of temperature-dependent PL experiments and spectro-electrochemistry measurements on bare-core $CuInS_2$ NCs and core/shell $CuInS_2$/ZnS NCs, I showed that ternary NCs are affected by both an intrinsic and an extrinsic nonradiative recombination mechanism. The former is progressively suppressed by lowering the NCs’ temperature and is independent of the surface passivation. It is therefore most likely associated with internal electron accepting defects. The latter, contrarily, is induced by the surface traps and can be thus inhibited by the inorganic capping layer or by tuning the Fermi level.

Collaborations

This work is the result of several collaborations that significantly improved the quality of my project. During my PhD course, I had the chance to meet and work with researchers from several institutions spread around the world, reciprocally increasing the opportunities to boost the scientific research and offering me the chance to expand my knowledge and background. I would reserve a notable mention to Dr. Scott A. Crooker who hosted me at the High Magnetic Field National Laboratory in Los Alamos (USA) for six months. Besides the excellent results we achieved and that I presented here in Chapters 4 and 5, it's been a honor for me to work under his guidance and to learn from him.

The results shown in Chapter 2 have been achieved in collaboration with Dr. Sotirios Christodoulou and Dr. Francesco De Donato of Dr. Iwan Moreel's research group at the Istituto Italiano di Tecnologia in Genoa (Italy), who synthesized the CdSe/CdS W/W-NCs and with Dr. Wan Ki Bae of Dr. Victor Klimov's group at the Chemistry Division of Los Alamos National Laboratory (USA), who synthesized the Z/W-NCs. Pump and probe and amplified spontaneous emission experiments were carried out at the Politecnico di Milano (Italy) together with Andrea Camellini and Gianluca Sirigu of Prof. Margherita Zavelani-Rossi's research group.

The "quantized"-doping synthesis described in Chapter 3 has been developed by my colleague Dr. Beatriz Santiago-González, and the structural and elemental characterizations of the NCs were performed by Dr. Alberto Casu, Dr. Mirko Prato and Dr. Carlo Santambrogio of Dr. Liberato Manna's research group at Istituto Italiano di Tecnologia in Genoa (Italy) and by Dr. Roberto Lorenzi, Prof. Marcello Campione and Dr. Norberto Chiodini at the Università di Milano-Bicocca. My colleague Dr. Angelo Monguzzi collaborated with the optical experiments.

The Mn-doped CdSe NCs reported in Chapter 4 were synthesized by Dr. Wenyong Liu in Dr. Victor Klimov's laboratory at the Chemistry Division of Los Alamos National Laboratory (USA). Dr. William D. Rice collaborated to the resonant PL experiments at the High Magnetic Field National Laboratory in Los Alamos (USA), under the guidance of Dr. Scott A. Crooker. Monte Carlo calculations were performed by Prof. Dmitri R. Yakovlev at the Technische Universität Dortmund (Germany).

Silver-doped CdSe NCs presented in Chapter 5 were produced by my collaborator Qiumei Di in Prof. Jiatao Zhang's laboratory at the Beijing Institute of Technology (China). Pump and probe experiments were performed with Andrea Camellini of Prof. Margherita Zavelani-Rossi's research group at the Politecnico di Milano (Italy). My colleague Dr. Monica Lorenzon carried out the spectro-electrochemistry experiments, whereas I acquired the MCD data at the High Magnetic Field National Laboratory in Los Alamos (USA) under the supervision of Dr. Scott A. Crooker. Dr. Mauro Fasoli collaborated to acquire PL data at cryogenic temperatures at the Università di Milano-Bicocca.

Finally, ternary CIS NCs investigated in Chapter 6 were synthesized by Dr. Hunter McDaniel in Dr. Victor Klimov's laboratory at the Chemistry Division of Los Alamos National Laboratory

(USA). Dr. Roberto Lorenzi performed compositional X-Ray Fluorescence measurements at the Università di Milano-Bicocca and my colleague Dr. Monica Lorenzon collaborated with the spectro-electrochemistry experiments.

Besides the experiments reported in Chapter 4, that were fully coordinated by Dr. Scott A. Crooker, all the results I showed were conceived and organized by Prof. Sergio Brovelli and Prof. Francesco Meinardi, that have constantly supported my research throughout the years of my PhD course.

References

[1] Lee, J. R. I. *et al.*, *Phys. Rev. Lett.*, **2007**, 98 (*14*), 146803.
[2] Li, D. *et al.*, *Nano Res.*, **2015**, 8 (*9*), 3035-3044.
[3] Cheng, C.-T. *et al.*, *J. Mater. Chem.*, **2005**, 15 (*33*), 3409-3414.
[4] Wei, S.-H. *et al.*, *Phys. Rev. B*, **2000**, 62 (*11*), 6944-6947.
[5] Bandić, Z. Z. *et al.*, *Phys. Rev. B*, **1995**, 51 (*15*), 9806-9812.
[6] Markus, T. Z. *et al.*, *J. Phys. Chem. C*, **2009**, 113 (*32*), 14200-14206.
[7] Xing, C. *et al.*, *Int. J. Hydrog. Energy*, **2006**, 31 (*14*), 2018-2024.
[8] Murayama, M. *et al.*, *Phys. Rev. B*, **1994**, 49 (*7*), 4710-4724.
[9] Lippens, P. E. *et al.*, *Phys. Rev. B*, **1990**, 41 (*9*), 6079-6081.
[10] Wang, L.-W. *et al.*, *Phys. Rev. B*, **2004**, 69 (*15*), 153302.
[11] Meulenberg, R. W. *et al.*, *ACS Nano*, **2009**, 3 (*2*), 325-330.
[12] Gross, E. F., *Il Nuovo Cimento*, **1956**, 3 (*4*), 672-701.
[13] Yoffe, A. D., *Adv. Phys.*, **1993**, 42 (*2*), 173-262.
[14] Evans, B. L. *et al.*, *Proc. Royal Soc. A*, **1967**, 298 (*1452*), 74-96.
[15] Rossetti, R. *et al.*, *J. Chem. Phys.*, **1984**, 80 (*9*), 4464-4469.
[16] Ekimov, A. I. *et al.*, *J. Exp. Theor. Phys. Lett.*, **1981**, 34 (*6*), 345.
[17] Koch, S. W. *et al.*, *J. Cryst. Growth*, **1992**, 117 (*1*), 592-597.
[18] Ekimov, A. I. *et al.*, *J. Opt. Soc. Am. B*, **1993**, 10 100-107.
[19] Norris, D. J. *et al.*, *Phys. Rev. B*, **1996**, 53 (*24*), 16347-16354.
[20] Bawendi, M. G. *et al.*, *J. Chem. Phys.*, **1992**, 96 (*2*), 946-954.
[21] Efros, A. L., *Phys. Rev. B*, **1992**, 46 (*12*), 7448-7458.
[22] Efros, A. L. *et al.*, *Phys. Rev. B*, **1993**, 47 (*15*), 10005-10007.
[23] Nirmal, M. *et al.*, *Phys. Rev. Lett.*, **1995**, 75 (*20*), 3728-3731.
[24] Efros, A. L. *et al.*, *Phys. Rev. B*, **1996**, 54 (*7*), 4843-4856.
[25] Efros, A. L. *et al.*, *Phys. Rev. Lett.*, **1997**, 78 (*6*), 1110-1113.
[26] Kuno, M. *et al.*, *J. Chem. Phys.*, **1998**, 108 (*10*), 4242-4247.
[27] Kulakovskii, V. D. *et al.*, *Phys. Rev. Lett.*, **1999**, 82 (*8*), 1780-1783.
[28] Gupta, J. A. *et al.*, *Phys. Rev. B*, **2002**, 66 (*12*), 125307.
[29] Wang, L.-W. *et al.*, *Phys. Rev. Lett.*, **2003**, 91 (*5*), 056404.
[30] Chen, P. *et al.*, *Phys. Rev. B*, **2004**, 70 (*4*), 045311.
[31] Cragg, G. E. *et al.*, *Nano Lett.*, **2010**, 10 (*1*), 313-317.
[32] Rodina, A. V. *et al.*, *Phys. Rev. B*, **2010**, 82 (*12*), 125324.
[33] Rodina, A. *et al.*, *Nano Lett.*, **2015**, 15 (*6*), 4214-4222.
[34] Rodina, A. V. *et al.*, *Phys. Rev. B*, **2016**, 93 (*15*), 155427.
[35] Hines, M. A. *et al.*, *J. Phys. Chem.*, **1996**, 100 (*2*), 468-471.
[36] Dabbousi, B. O. *et al.*, *J. Phys. Chem. B*, **1997**, 101 (*46*), 9463-9475.
[37] Jacobsohn, M. *et al.*, *J. Phys. Chem. B*, **2000**, 104 (*1*), 1-5.
[38] Johnston-Halperin, E. *et al.*, *Phys. Rev. B*, **2001**, 63 (*20*), 205309.
[39] Kucur, E. *et al.*, *J. Chem. Phys.*, **2003**, 119 (*4*), 2333-2337.
[40] Brokmann, X. *et al.*, *New J. Phys.*, **2004**, 6 (*1*), 1-8.
[41] Cretí, A. *et al.*, *Phys. Rev. B*, **2005**, 72 (*12*), 125346.
[42] Furis, M. *et al.*, *J. Phys. Chem. B*, **2005**, 109 (*32*), 15332-15338.
[43] Furis, M. *et al.*, *Phys. Rev. B*, **2006**, 73 (*24*), 241313.
[44] Inamdar, S. N. *et al.*, *ChemPhysChem*, **2008**, 9 (*17*), 2574-2579.
[45] Htoon, H. *et al.*, *Phys. Rev. Lett.*, **2009**, 102 (*1*), 017402.
[46] Liu, L. *et al.*, *J. Am. Chem. Soc.*, **2009**, 131 (*45*), 16423-16429.
[47] Shan, W. *et al.*, *Phys. Rev. B*, **1994**, 50 (*11*), 8012-8015.

[48] Rössler, U., *Phys. Rev.*, **1969**, 184 (*3*), 733-738.
[49] Laheld, U. E. H. *et al.*, *Phys. Rev. B*, **1997**, 55 (*8*), 5184-5204.
[50] Xia, J.-B., *Phys. Rev. B*, **1989**, 40 (*12*), 8500-8507.
[51] Vahala, K. J. *et al.*, *Phys. Rev. Lett.*, **1990**, 65 (*2*), 239-242.
[52] Calcott, P. D. J. *et al.*, *J. Lumin.*, **1993**, 57 (*1*), 257-269.
[53] Nomura, S. *et al.*, *Phys. Rev. B*, **1994**, 49 (*19*), 13571-13582.
[54] Takagahara, T., *Phys. Rev. B*, **1993**, 47 (*8*), 4569-4584.
[55] Henry, C. H. *et al.*, *Phys. Rev. B*, **1970**, 1 (*4*), 1628-1634.
[56] O'Neil, M. *et al.*, *J. Phys. Chem.*, **1990**, 94 (*10*), 4356-4363.
[57] Kuno, M. *et al.*, *J. Chem. Phys.*, **1997**, 106 (*23*), 9869-9882.
[58] Htoon, H. *et al.*, *Phys. Rev. Lett.*, **2004**, 93 (*18*), 187402.
[59] Boles, M. A. *et al.*, *Nat. Mater.*, **2016**, 15 141.
[60] Galland, C. *et al.*, *Nature*, **2011**, 479 203-207.
[61] Shabaev, A. *et al.*, *Nano Lett*, **2013**, 13 (*11*), 5454-5461.
[62] Feng, D. *et al.*, *Nano Lett*, **2017**, 17 (*5*), 2844-2851.
[63] Gong, K. *et al.*, *J. Phys. Chem. C*, **2015**, 119 (*17*), 9637-9645.
[64] Kobayashi, Y. *et al.*, *J. Phys. Chem. Lett.*, **2011**, 2 (*9*), 1051-1055.
[65] Efros, A. L. *et al.*, *Solid State Commun.*, **1989**, 72 (*7*), 645-649.
[66] Park, Y.-S. *et al.*, *ACS Nano*, **2014**, 8 (*7*), 7288-7296.
[67] Chepic, D. I. *et al.*, *J. Lumin.*, **1990**, 47 (*3*), 113-127.
[68] Howes, P. D. *et al.*, *Science*, **2014**, 346 (*6205*).
[69] Medintz, I. L. *et al.*, *Nat. Mater.*, **2005**, 4 (*6*), 435-446.
[70] Mura, S. *et al.*, *Nat. Mater.*, **2013**, 12 991.
[71] Henglein, A. *et al.*, *Ber. Bunsen. Phys. Chem.*, **1989**, 93 (*5*), 593-600.
[72] Spanhel, L. *et al.*, *Ber. Bunsen. Phys. Chem.*, **1987**, 91 (*2*), 88-94.
[73] Weller, H. *et al.*, *Ber. Bunsen. Phys. Chem.*, **1984**, 88 (*7*), 649-656.
[74] Zhou, H. S. *et al.*, *J. Phys. Chem.*, **1993**, 97 (*4*), 895-901.
[75] Haesselbarth, A. *et al.*, *J. Phys. Chem.*, **1993**, 97 (*20*), 5333-5340.
[76] Kim, S. *et al.*, *J. Am. Chem. Soc.*, **2003**, 125 (*38*), 11466-11467.
[77] Ivanov, S. A. *et al.*, *J. Am. Chem. Soc.*, **2007**, 129 (*38*), 11708-11719.
[78] Nemchinov, A. *et al.*, *J. Phys. Chem. C*, **2008**, 112 (*25*), 9301-9307.
[79] Peng, X. *et al.*, *J. Am. Chem. Soc.*, **1997**, 119 (*30*), 7019-7029.
[80] Pietryga, J. M. *et al.*, *J. Am. Chem. Soc.*, **2008**, 130 (*14*), 4879-4885.
[81] Wu, K. *et al.*, *J. Phys. Chem. A*, **2013**, 117 (*32*), 7561-7570.
[82] Brovelli, S. *et al.*, *Nat. Commun.*, **2011**, 2 280.
[83] Eychmüller, A. *et al.*, *Chem. Phys. Lett.*, **1993**, 208 (*1*), 59-62.
[84] Chen, Y. *et al.*, *J. Am. Chem. Soc.*, **2008**, 130 (*15*), 5026-5027.
[85] Dorfs, D. *et al.*, *Z. Phys. Chem.*, **2006**, 220 (*12*), 1539.
[86] Jun, S. *et al.*, *Angew. Chem., Int. Ed.*, **2013**, 52 (*2*), 679-682.
[87] Xie, R. *et al.*, *J. Am. Chem. Soc.*, **2005**, 127 (*20*), 7480-7488.
[88] Pan, D. *et al.*, *Chem. Mater.*, **2006**, 18 (*18*), 4253-4258.
[89] Little, R. B. *et al.*, *J. Chem. Phys.*, **2001**, 114 (*4*), 1813-1822.
[90] Braun, M. *et al.*, *J. Phys. Chem. A*, **2001**, 105 (*23*), 5548-5551.
[91] Battaglia, D. *et al.*, *J. Am. Chem. Soc.*, **2005**, 127 (*31*), 10889-10897.
[92] Bae, W. K. *et al.*, *ACS Nano*, **2013**, 7 (*4*), 3411-3419.
[93] Christodoulou, S. *et al.*, *J. Mater. Chem. C*, **2014**, 2 (*17*), 3439-3447.
[94] Garcia-Santamaria, F. *et al.*, *Nano Lett.*, **2011**, 11 (*2*), 687-693.
[95] Htoon, H. *et al.*, *Nano Lett.*, **2010**, 10 (*7*), 2401-2407.
[96] Kundu, B. *et al.*, *J. Appl. Phys.*, **2016**, 119 (*10*), 104304.
[97] Malko, A. V. *et al.*, *Nano Lett.*, **2011**, 11 (*12*), 5213-5218.
[98] Nan, W. *et al.*, *J. Am. Chem. Soc.*, **2012**, 134 (*48*), 19685-19693.
[99] Nasilowski, M. *et al.*, *Nano Lett.*, **2015**, 15 (*6*), 3953-3958.

[100] Park, Y. S. *et al.*, *Phys. Rev. Lett.*, **2011**, 106 (*18*), 187401.
[101] Liu, F. *et al.*, *Phys. Rev. B*, **2013**, 88 (*3*), 035302.
[102] Siebers, B. *et al.*, *Phys. Rev. B*, **2015**, 91 (*15*), 155304.
[103] Kocevski, V. *et al.*, *Sci. Rep.*, **2015**, 5 10865.
[104] Shabaev, A. *et al.*, *Phys. Rev. B*, **2012**, 86 (*20*), 205311.
[105] Carbone, L. *et al.*, *Nano Lett.*, **2007**, 7 (*10*), 2942-2950.
[106] Di Stasio, F. *et al.*, *Small*, **2015**, 11 (*11*), 1328-1334.
[107] Lupo, M. G. *et al.*, *Nano Lett.*, **2008**, 8 (*12*), 4582-4587.
[108] Pisanello, F. *et al.*, *Phys. Status Solidi (C)*, **2010**, 7 (*11-12*), 2688-2691.
[109] Rainò, G. *et al.*, *ACS Nano*, **2011**, 5 (*5*), 4031-4036.
[110] Zavelani-Rossi, M. *et al.*, *Nano Lett.*, **2010**, 10 (*8*), 3142-3150.
[111] Christodoulou, S. *et al.*, *Nat. Commun.*, **2015**, 6 7905.
[112] Talapin, D. V. *et al.*, *Nano Lett.*, **2007**, 7 (*10*), 2951-2959.
[113] Diroll, B. T. *et al.*, *J. Phys. Chem. C*, **2013**, 117 (*45*), 23928-23937.
[114] Diroll, B. T. *et al.*, *J. Phys. Chem. Lett.*, **2014**, 5 (*1*), 85-91.
[115] Cassette, E. *et al.*, *ACS Nano*, **2012**, 6 (*8*), 6741-6750.
[116] Lorenzon, M. *et al.*, *Nat. Commun.*, **2015**, 6.
[117] Mahler, B. *et al.*, *J. Am. Chem. Soc.*, **2012**, 134 (*45*), 18591-18598.
[118] Pelton, M. *et al.*, *Nano Lett.*, **2017**, 17 (*11*), 6900-6906.
[119] Nasilowski, M. *et al.*, *Chem. Rev.*, **2016**, 116 (*18*), 10934-10982.
[120] Tessier, M. D. *et al.*, *Nano Lett.*, **2014**, 14 (*1*), 207-213.
[121] Li, Q. *et al.*, *ACS Nano*, **2016**, 10 (*3*), 3843-3851.
[122] Prudnikau, A. *et al.*, *J. Am. Chem. Soc.*, **2013**, 135 (*39*), 14476-14479.
[123] Borys, N. J. *et al.*, *Science*, **2010**, 330 (*6009*), 1371-1374.
[124] Choi, C. L. *et al.*, *Nano Lett.*, **2009**, 9 (*10*), 3544-3549.
[125] Kim, M. R. *et al.*, *ACS Nano*, **2012**, 6 (*12*), 11088-11096.
[126] Wong, J. I. *et al.*, *ACS Nano*, **2014**, 8 (*3*), 2873-2879.
[127] Scotognella, F. *et al.*, *J. Phys. Chem. C*, **2011**, 115 (*18*), 9005-9011.
[128] Deka, S. *et al.*, *Nano Lett.*, **2010**, 10 (*9*), 3770-3776.
[129] Climente, J. I. *et al.*, *Small*, **2012**, 8 (*5*), 754-759.
[130] Galland, C. *et al.*, *Nano Lett.*, **2013**, 13 (*1*), 321-328.
[131] Kang, K. I. *et al.*, *Phys. Rev. B*, **1992**, 45 (*7*), 3465-3468.
[132] Titova, L. V. *et al.*, *Appl. Phys. Lett.*, **2006**, 89 (*5*), 053119.
[133] Brovelli, S. *et al.*, *Nano Lett.*, **2013**, 14 (*2*), 486-494.
[134] Mocatta, D. *et al.*, *Science*, **2011**, 332 (*6025*), 77-81.
[135] Sahu, A. *et al.*, *Nano Lett.*, **2012**, 12 (*5*), 2587-2594.
[136] Gaj, J. A. *et al.*, *Phys. Status Solidi (B)*, **1978**, 89 (*2*), 655-662.
[137] Gaj, J. A. *et al.*, *Solid State Commun.*, **1979**, 29 (*5*), 435-438.
[138] Furdyna, J. K., *J. Appl. Phys.*, **1988**, 64 (*4*), R29-R64.
[139] Tanabe, Y. *et al.*, *J. Phys. Soc. Jpn.*, **1954**, 9 (*5*), 753-766.
[140] Pisanic, T. R., 2nd *et al.*, *Analyst*, **2014**, 139 (*12*), 2968-2981.
[141] Wang, Y. *et al.*, *ACS Appl. Mater. Interfaces*, **2013**, 5 (*8*), 2786-2799.
[142] Wegner, K. D. *et al.*, *Chem Soc Rev*, **2015**, 44 (*14*), 4792-4834.
[143] Cunha-Reis, C. *et al.*, *J Tissue Eng Regen Med*, **2013**, 7 (*1*), 39-50.
[144] Chen, G. *et al.*, *Chem Soc Rev*, **2015**, 44 (*6*), 1680-1713.
[145] Kim, J.-H. *et al.*, *Chem. Mater.*, **2014**, 27 (*1*), 197-204.
[146] Stolle, C. J. *et al.*, *J. Phys. Chem. Lett.*, **2014**, 5 (*2*), 304-309.
[147] Meinardi, F. *et al.*, *Nat. Nanotechnol.*, **2015**, 10 (*10*), 878-885.
[148] Gaetke, L. M. *et al.*, *Arch. Toxicol.*, **2014**, 88 (*11*), 1929-1938.
[149] *Commission Regulation (EU) 2016/217 of 16 February 2016 Amending Annex XVII to Regulation (EC) No. 1907/2006 of the European Parliament and of the Council concerning the Registration,*

Evaluation, Authorisation and Restriction of Chemicals (REACH) as regards cadmium. Vol. L 40 (2016).
[150] *Commission Regulation (EU) 2015/628 of 22 April 2015 Amending Annex XVII to Regulation (EC) No. 1907/2006 of the European Parliament and of the Council on the Registration, Evaluation, Authorisation and Restriction of Chemicals ('REACH') as Regards Lead and its Compounds* Vol. L 104 (2015).
[151] *Regulation (EU) 2017/852 of the European Parliament and of the Council of 17 May 2017 on Mercury, and repealing Regulation (EC) No. 1102/2008*. Vol. L 137 (2017).
[152] Lin, Q. *et al.*, *ACS Nano*, **2015**, 9 (*1*), 539-547.
[153] Soni, U. *et al.*, *ACS Nano*, **2014**, 8 (*1*), 113-123.
[154] Liu, S. *et al.*, *ChemPhysChem*, **2015**, 16 (*8*), 1663-1669.
[155] Dias, E. A. *et al.*, *J. Phys. Chem. C*, **2008**, 112 (*37*), 14229-14232.
[156] Nizamoglu, S. *et al.*, *Appl. Phys. Lett.*, **2008**, 92 (*11*), 113110.
[157] Sapra, S. *et al.*, *J. Phys. Chem. B*, **2005**, 109 (*5*), 1663-1668.
[158] Teitelboim, A. *et al.*, *ACS Nano*, **2015**, 10 (*1*), 446-452.
[159] Zhao, H. *et al.*, *Nanoscale*, **2016**.
[160] Zhao, H. *et al.*, *Small*, **2015**, 11 (*43*), 5741-5746.
[161] Brovelli, S. *et al.*, *Nano Lett.*, **2014**, 14 (*7*), 3855-3863.
[162] Lorenzon, M. *et al.*, *Nano Lett.*, **2017**, 17 (*2*), 1071-1081.
[163] Bruni, F. *et al.*, *Adv. Funct. Mater.*, **2017**, 27 (*12*), 1605533.
[164] Garcia-Santamaria, F. *et al.*, *Nano Lett.*, **2009**, 9 (*10*), 3482-3488.
[165] Meinardi, F. *et al.*, *Nat. Photonics*, **2014**, 8 (*5*), 392-399.
[166] Yang, Y. A. *et al.*, *Angew. Chem.*, **2005**, 117 (*41*), 6870-6873.
[167] Viswanatha, R. *et al.*, *Chem. Asian J.*, **2009**, 4 (*6*), 904-909.
[168] Sitt, A. *et al.*, *Nano Lett.*, **2011**, 11 (*5*), 2054-2060.
[169] Chen, O. *et al.*, *Nat. Mater.*, **2013**, 12 (*5*), 445-451.
[170] Cirloganu, C. M. *et al.*, *Nat. Commun.*, **2014**, 5 4148.
[171] Liao, C. *et al.*, *Photonics Res.*, **2015**, 3 (*5*), 200.
[172] Bae, W. K. *et al.*, *Nat. Commun.*, **2013**, 4 2661.
[173] Park, Y.-S. *et al.*, *Nano Lett.*, **2014**, 14 (*2*), 396-402.
[174] Klimov, V. I., *Annu. Rev. Phys. Chem.*, **2007**, 58 (*1*), 635-673.
[175] Klimov, V. I. *et al.*, *Nature*, **2007**, 447 441-446.
[176] Galland, C. *et al.*, *Nat. Commun.*, **2012**, 3 908.
[177] Javaux, C. *et al.*, *Nat. Nanotechnol.*, **2013**, 8 206-212.
[178] Klimov, V. I., *Annu. Rev. Condens. Matter Phys.*, **2014**, 5 (*1*), 285-316.
[179] Pradhan, N. *et al.*, *J. Am. Chem. Soc.*, **2005**, 127 (*50*), 17586-17587.
[180] Shao, P. *et al.*, *J. Mater. Chem.*, **2011**, 21 (*1*), 151-156.
[181] Chen, D. *et al.*, *J. Am. Chem. Soc.*, **2009**, 131 (*26*), 9333-9339.
[182] Jawaid, A. M. *et al.*, *ACS Nano*, **2013**, 7 (*4*), 3190-3197.
[183] Hanif, K. M. *et al.*, *J. Am. Chem. Soc.*, **2002**, 124 (*38*), 11495-11502.
[184] Perera, S. D. *et al.*, *J. Mater. Chem. C*, **2015**, 3 (*5*), 1044-1055.
[185] Radovanovic, P. V. *et al.*, *J. Am. Chem. Soc.*, **2001**, 123 (*49*), 12207-12214.
[186] Mehra, S. *et al.*, *Chem. Mater.*, **2016**, 28 (*10*), 3454-3461.
[187] Kang, M. S. *et al.*, *Adv. Mater.*, **2013**, 25 (*5*), 725-731.
[188] Eilers, J. *et al.*, *J. Phys. Chem. Lett.*, **2012**, 3 (*12*), 1663-1667.
[189] Liu, J. *et al.*, *Adv. Mater.*, **2015**, 27 (*17*), 2753-2761.
[190] Vlaskin, V. A. *et al.*, *J. Am. Chem. Soc.*, **2013**, 135 (*38*), 14380-14389.
[191] Barrows, C. J. *et al.*, *ACS Nano*, **2016**, 10 (*1*), 910-918.
[192] Yang, J. *et al.*, *J. Am. Chem. Soc.*, **2015**, 137 (*40*), 12776-12779.
[193] Saha, A. *et al.*, *J. Phys. Chem. Lett.*, **2016**, 2420-2428.
[194] Viswanatha, R. *et al.*, *Nano Lett.*, **2011**, 11 (*11*), 4753-4758.
[195] Beaulac, R. *et al.*, *Science*, **2009**, 325 (*5943*), 973-976.

[196] Fainblat, R. *et al.*, *Nano Lett.*, **2016**, 16 (*10*), 6371–6377.
[197] Bozyigit, D. *et al.*, *Nat. Commun.*, **2015**, 6.
[198] Nagpal, P. *et al.*, *Nat. Commun.*, **2011**, 2 486.
[199] Bussian, D. A. *et al.*, *Nat. Mater.*, **2009**, 8 (*1*), 35-40.
[200] Dance, I. G. *et al.*, *J. Am. Chem. Soc.*, **1984**, 106 (*21*), 6285-6295.
[201] Lees, E. E. *et al.*, *ACS Nano*, **2009**, 3 (*5*), 1121-1128.
[202] Zhang, L. *et al.*, *Nano Today*, **2014**, 9 (*1*), 132-157.
[203] Choi, S. *et al.*, *Chem. Soc. Rev.*, **2012**, 41 (*5*), 1867-1891.
[204] Chen, W. *et al. Functional Nanometer-Sized Clusters of Transition Metals: Synthesis, Properties and Applications*. (RSC, 2014).
[205] Qin, W. *et al.*, *Angew. Chem., Int. Ed.*, **2014**, 53 (*28*), 7316-7319.
[206] Corma, A. *et al.*, *Nat. Chem.*, **2013**, 5 (*9*), 775-781.
[207] Stamplecoskie, K. G. *et al.*, *J. Am. Chem. Soc.*, **2014**, 136 (*31*), 11093-11099.
[208] Gonzalez, B. S. *et al.*, *Nanoscale*, **2012**, 4 (*24*), 7632-7635.
[209] Wei, W. *et al.*, *J. Am. Chem. Soc.*, **2011**, 133 (*7*), 2060-2063.
[210] Muhammed, M. A. H. *et al.*, *ACS Nano*, **2012**, 6 (*10*), 8950-8961.
[211] Jin, R., *Nanoscale*, **2015**, 7 (*5*), 1549-1565.
[212] Udayabhaskararao, T. *et al.*, *Angew. Chem., Int. Ed.*, **2012**, 51 (*9*), 2155-2159.
[213] Ganguly, M. *et al.*, *RSC Adv.*, **2016**, 6 (*21*), 17683-17703.
[214] Lesnyak, V. *et al.*, *Chem. Soc. Rev.*, **2013**, 42 (*7*), 2905-2929.
[215] Brovelli, S. *et al.*, *Nano Lett.*, **2012**, 12 (*8*), 4372-4379.
[216] Meulenberg, R. W. *et al.*, *Nano Lett.*, **2004**, 4 (*11*), 2277-2285.
[217] Pandey, A. *et al.*, *Nat. Nanotechnol.*, **2012**, 7 (*12*), 792-797.
[218] Srivastava, B. B. *et al.*, *J. Am. Chem. Soc.*, **2011**, 133 (*4*), 1007-1015.
[219] Knowles, K. E. *et al.*, *Chem. Rev.*, **2016**.
[220] Jia, X. *et al.*, *Chem. Commun.*, **2014**, 50 (*2*), 237-239.
[221] Yergey, J. A., *Int. J. Mass Spectr. Ion Phys.*, **1983**, 52 (*2*), 337-349.
[222] Srivastava, B. B. *et al.*, *J. Am. Chem. Soc.*, **2010**, 133 (*4*), 1007-1015.
[223] Kovalenko, M. V. *et al.*, *Acs Nano*, **2015**, 9 (*2*), 1012-1057.
[224] Zhang, F. *et al.*, *J. Mater. Chem.*, **2012**, 22 (*41*), 22250-22257.
[225] Sowa, H., *Solid State Sciences*, **2005**, 7 (*1*), 73-78.
[226] Wu, P. *et al.*, *Chem. Soc. Rev.*, **2013**, 42 (*12*), 5489-5521.
[227] Xuan, T. *et al.*, *Chem. Commun.*, **2013**, 49 (*79*), 9045-9047.
[228] Wei, H. H.-Y. *et al.*, *Nano Lett.*, **2012**, 12 (*9*), 4465-4471.
[229] Yang, J. *et al.*, *J. Colloid Interface Sci.*, **2013**, 394 55-62.
[230] Grandhi, G. K. *et al.*, *ACS Nano*, **2012**, 6 (*11*), 9751-9763.
[231] Sargent, E. H., *Nat. Photonics*, **2012**, 6 133-135.
[232] Kavokin, K. V. *et al.*, *Phys. Rev. B*, **1999**, 60 (*24*), 16499-16505.
[233] Dietl, T. *et al.*, *Phys. Rev. Lett.*, **1995**, 74 (*3*), 474-477.
[234] Kusrayev, Y. G. *et al.*, *Phys. Rev. B*, **2008**, 77 (*8*), 085205.
[235] Fiederling, R. *et al.*, *Phys. Rev. B*, **1998**, 58 (*8*), 4785-4792.
[236] Oka, Y. *et al.*, *J. Lumin.*, **1999**, 83-84 83-89.
[237] Takeyama, S. *et al.*, *Phys. Rev. B*, **1995**, 51 (*8*), 4858-4864.
[238] Mackh, G. *et al.*, *Phys. Rev. B*, **1994**, 50 (*19*), 14069-14076.
[239] Mackh, G. *et al.*, *Phys. Rev. B*, **1994**, 49 (*15*), 10248-10258.
[240] Yakovlev, D. R. *et al.*, *Solid State Commun.*, **1992**, 82 (*1*), 29-32.
[241] Itoh, T. *et al.*, *J. Lumin.*, **1987**, 38 (*1*), 266-268.
[242] Zayhowski, J. J. *et al.*, *Solid State Commun.*, **1985**, 55 (*11*), 941-945.
[243] Abolfath, R. M. *et al.*, *Phys. Rev. Lett.*, **2007**, 98 (*20*), 207203.
[244] Bacher, G. *et al.*, *Phys. Rev. Lett.*, **2002**, 89 (*12*), 127201.
[245] Besombes, L. *et al.*, *Phys. Rev. Lett.*, **2004**, 93 (*20*), 207403.
[246] Dorozhkin, P. S. *et al.*, *Phys. Rev. B*, **2003**, 68 (*19*), 195313.

[247] Kłopotowski, Ł. *et al.*, *Phys. Rev. B*, **2011**, 83 (*8*), 081306.
[248] Mackowski, S. *et al.*, *Appl. Phys. Lett.*, **2004**, 84 (*17*), 3337-3339.
[249] Maksimov, A. A. *et al.*, *Phys. Rev. B*, **2000**, 62 (*12*), R7767-R7770.
[250] Sellers, I. R. *et al.*, *Phys. Rev. B*, **2010**, 82 (*19*), 195320.
[251] Seufert, J. *et al.*, *Phys. Rev. Lett.*, **2001**, 88 (*2*), 027402.
[252] Trojnar, A. H. *et al.*, *Phys. Rev. Lett.*, **2011**, 107 (*20*), 207403.
[253] Wojnar, P. *et al.*, *Phys. Rev. B*, **2007**, 75 (*15*), 155301.
[254] Nelson, H. D. *et al.*, *ACS Nano*, **2015**, 9 (*11*), 11177-11191.
[255] Rice, W. D. *et al.*, *Nat. Nanotechnol.*, **2016**, 11 (*2*), 137-142.
[256] Yu, J. H. *et al.*, *Nat. Mater.*, **2010**, 9 (*1*), 47-53.
[257] Merkulov, I. A. *et al.*, *Phys. Rev. Lett.*, **1999**, 83 (*7*), 1431-1434.
[258] Norris, D. J. *et al.*, *Nano Lett.*, **2001**, 1 (*1*), 3-7.
[259] Beaulac, R. *et al.*, *Adv. Funct. Mater.*, **2008**, 18 (*24*), 3873-3891.
[260] Fainblat, R. *et al.*, *Nano Lett.*, **2012**, 12 (*10*), 5311-5317.
[261] Rice, W. D. *et al.*, *Nano Lett.*, **2017**.
[262] Muckel, F. *et al.*, *Nano Lett*, **2017**.
[263] Krustok, J. *et al.*, *J. Phys. Chem. Solids*, **1990**, 51 (*9*), 1013-1018.
[264] Krustok, J., *J. Phys. Chem. Solids*, **1992**, 53 (*8*), 1027-1030.
[265] Peka, P. *et al.*, *Physica B*, **1994**, 193 (*1*), 57-65.
[266] Stringfellow G. B. *et al.*, *Phys. Rev.*, **1968**, 171 (*3*), 903–915.
[267] Nelson, H. D. *et al.*, *J. Am. Chem. Soc.*, **2017**, 139 (*18*), 6411-6421.
[268] Kompch, A. *et al.*, *J. Phys. Chem. C*, **2015**, 119 (*32*), 18762-18772.
[269] Grochala, W. *et al.*, *Angew. Chem., Int. Ed.*, **2001**, 40 (*15*), 2742-2781.
[270] Dean, P. J. *et al.*, *Phys. Rev. B*, **1982**, 26 (*4*), 2016-2035.
[271] Holtz, P. O. *et al.*, *Phys. Rev. B*, **1985**, 32 (*2*), 986-996.
[272] Nedeoglo, N. D. *et al.*, *J. Phys. Condens. Matter*, **2006**, 18 (*34*), 8113.
[273] McMillan, J. A., *Chem. Rev.*, **1962**, 62 (*1*), 65-80.
[274] Burdett, J. K. *et al.*, *Inorg. Chem.*, **1992**, 31 (*10*), 1758-1762.
[275] Vydyanath, H. R. *et al.*, *J. Phys. Chem. Solids*, **1975**, 36 (*6*), 509-520.
[276] Jana, S. *et al.*, *Small*, **2013**, 9 (*22*), 3753-3758.
[277] Pietryga, J. M. *et al.*, *Chem. Rev.*, **2016**, 116 (*18*), 10513-10622.
[278] Pinchetti, V. *et al.*, *Nano Lett.*, **2017**, 17 (*7*), 4508-4517.
[279] Lorenzon, M. *et al.*, *Nano Lett.*, **2017**, 17 (*6*), 3844-3853.
[280] Padilha, L. A. *et al.*, *ACS nano*, **2011**, 5 (*6*), 5045-5055.
[281] Schulz, H. J., *J. Cryst. Growth*, **1982**, 59 (*1*), 65-80.
[282] Schulz, H. J., *Mater. Chem. Phys.*, **1987**, 16 (*5*), 373-384.
[283] Stern, N. P. *et al.*, *Phys. Rev. B*, **2005**, 72 (*16*), 161303.
[284] Archer, P. I. *et al.*, *Nano Lett.*, **2007**, 7 (*4*), 1037-1043.
[285] Poolton, N. R. J. *et al.*, *J. Cryst. Growth*, **1985**, 72 (*1*), 336-341.
[286] Zhong, H. *et al.*, *Chem. Mater.*, **2008**, 20 (*20*), 6434-6443.
[287] Allen, P. M. *et al.*, *J. Am. Chem. Soc.*, **2008**, 130 (*29*), 9240-9241.
[288] Singh, A. *et al.*, *Chem. Mater.*, **2015**, 27 (*5*), 1517-1523.
[289] Booth, M. *et al.*, *Chem. Mater.*, **2012**, 24 (*11*), 2064-2070.
[290] Kolny-Olesiak, J. *et al.*, *ACS Appl. Mater. Interfaces*, **2013**, 5 (*23*), 12221-12237.
[291] Berends, A. C. *et al.*, *J. Phys. Chem. Lett.*, **2016**, 7 (*17*), 3503-3509.
[292] Li, L. *et al.*, *J. Am. Chem. Soc.*, **2011**, 133 (*5*), 1176-1179.
[293] Yarema, O. *et al.*, *Chem. Mater.*, **2013**, 25 (*18*), 3753-3757.
[294] Zhong, H. *et al.*, *ACS Nano*, **2010**, 4 (*9*), 5253-5262.
[295] Jana, A. *et al.*, *Chem. Mater.*, **2016**, 28 (*4*), 1107-1120.
[296] Speranskaya, E. S. *et al.*, *Langmuir*, **2014**, 30 (*25*), 7567-7575.
[297] Deng, D. *et al.*, *Chem. Mater.*, **2012**, 24 (*15*), 3029-3037.
[298] Yu, K. *et al.*, *ACS Appl. Mater. Interfaces*, **2013**, 5 (*8*), 2870-2880.

[299] Pons, T. *et al.*, *ACS Nano*, **2010**, 4 (*5*), 2531-2538.
[300] Song, W.-S. *et al.*, *Chem. Mater.*, **2012**, 24 (*10*), 1961-1967.
[301] Sun, C. *et al.*, *Appl. Phys. Lett.*, **2014**, 104 (*26*), 261106.
[302] Halpert, J. E. *et al.*, *ACS Nano*, **2015**, 9 (*6*), 5857-5867.
[303] Li, W. *et al.*, *J. Mater. Chem. A*, **2015**, 3 (*4*), 1649-1655.
[304] McDaniel, H. *et al.*, *Nat. Commun.*, **2013**, 4 2887.
[305] McDaniel, H. *et al.*, *J. Phys. Chem. Lett.*, **2013**, 4 (*3*), 355-361.
[306] Panthani, M. G. *et al.*, *J. Am. Chem. Soc.*, **2008**, 130 (*49*), 16770-16777.
[307] Li, L. *et al.*, *J. Am. Chem. Soc.*, **2010**, 132 (*1*), 22-23.
[308] Arici, E. *et al.*, *Adv. Funct. Mater.*, **2003**, 13 (*2*), 165-171.
[309] Brandt, R. E. *et al.*, *MRS Commun.*, **2015**, 5 (*02*), 265-275.
[310] Hu, X. *et al.*, *Opt. Express*, **2015**, 23 (*15*), A858-867.
[311] Knowles, K. E. *et al.*, *Chem. Commun.*, **2015**.
[312] Bradshaw, L. R. *et al.*, *Nano Lett.*, **2015**, 15 (*2*), 1315-1323.
[313] Meinardi, F. *et al.*, *Nat. Photonics*, **2017**, 11 (*3*), 177-185.
[314] Whitham, P. J. *et al.*, *J. Phys. Chem. C*, **2016**, 120 (*30*), 17136-17142.
[315] Zang, H. *et al.*, *Nano Lett.*, **2017**, 17 (*3*), 1787-1795.
[316] Rice, W. D. *et al.*, *J. Phys. Chem. Lett.*, **2014**, 5 (*23*), 4105-4109.
[317] Shabaev, A. *et al.*, *Phys. Rev. B*, **2015**, 92 (*3*), 035431.
[318] Knowles, K. E. *et al.*, *Chem. Rev.*, **2016**, 116 10820−10851.
[319] Castro, S. L. *et al.*, *J. Phys. Chem. B*, **2004**, 108 (*33*), 12429-12435.
[320] Kim, Y.-K. *et al.*, *J. Mater. Chem.*, **2012**, 22 (*4*), 1516-1520.
[321] Leach, A. D. P. *et al.*, *J. Phys. Chem. C*, **2016**, 120 (*9*), 5207-5212.
[322] Shi, A. *et al.*, *J. Lumin.*, **2012**, 132 (*7*), 1819-1823.
[323] Sun, J. *et al.*, *Phys. Chem. Chem. Phys.*, **2015**, 17 (*18*), 11981-11989.
[324] Tran, T. K. C. *et al.*, *Adv. Nat. Sci.: Nanosci. Nanotech.*, **2010**, 1 (*2*), 025007.
[325] Zhong, H. *et al.*, *J. Phys. Chem. Lett.*, **2012**, 3 (*21*), 3167-3175.
[326] Chen, B. *et al.*, *Adv. Funct. Mater.*, **2012**, 22 (*10*), 2081-2088.
[327] Uehara, M. *et al.*, *J. Chem. Phys.*, **2008**, 129 (*13*), 134709.
[328] Jara, D. H. *et al.*, *J. Phys. Chem. Lett.*, **2016**, 7 (*8*), 1452-1459.
[329] Corrado, C. *et al.*, *Nanoscale*, **2010**, 2 (*7*), 1213-1221.
[330] Erwin, S. C. *et al.*, *Nature*, **2005**, 436 (*7047*), 91-94.
[331] Stouwdam, J. W. *et al.*, *Adv. Mater.*, **2009**, 21 (*28*), 2916-2920.
[332] Zhang, W. *et al.*, *Chem. Mater.*, **2014**, 26 (*2*), 1204-1212.
[333] Broser, I. *et al.*, *J. Electrochem. Soc.*, **1961**, 108 (*6*), 545-548.
[334] Stringfellow, G. B. *et al.*, *Phys. Rev.*, **1968**, 171 (*3*), 903-915.
[335] Grandhi, G. K. *et al.*, *J. Phys. Chem. Lett.*, **2013**, 4 (*3*), 409-415.
[336] Santiago-Gonzalez, B. *et al.*, *ACS Nano*, **2017**, 11 (*6*), 6233-6242.
[337] Knowles, K. E. *et al.*, *J. Am. Chem. Soc.*, **2015**, 137 (*40*), 13138-13147.
[338] Jaffe, J. E. *et al.*, *Phys. Rev. B*, **1983**, 28 (*10*), 5822-5847.
[339] Jaffe, J. E. *et al.*, *Phys. Rev. B*, **1983**, 27 (*8*), 5176-5179.
[340] Jaffe, J. E. *et al.*, *Phys. Rev. B*, **1984**, 29 (*4*), 1882-1906.
[341] McDaniel, H. *et al.*, *J. Phys. Chem. C*, **2014**, 118 (*30*), 16987-16994.
[342] De Trizio, L. *et al.*, *Chem. Mater.*, **2012**, 24 (*12*), 2400-2406.
[343] Witt, E. *et al.*, *Chem. Eur. J.*, **2013**, 19 (*30*), 9746-9753.
[344] Zhang, S. B. *et al.*, *Phys. Rev. B*, **1998**, 57 (*16*), 9642-9656.
[345] Tang, X. *et al.*, *Chem Commun*, **2011**, 47 (*18*), 5217-5219.
[346] Kraatz, I. T. *et al.*, *J. Phys. Chem. C*, **2014**, 118 (*41*), 24102-24109.
[347] Liu, W. *et al.*, *J. Lumin.*, **2015**, 162 191-196.
[348] Jha, P. P. *et al.*, *ACS Nano*, **2009**, 3 (*4*), 1011-1015.
[349] Xie, R. *et al.*, *J. Am. Chem. Soc.*, **2009**, 131 (*15*), 5691-5697.
[350] Wuister, S. F. *et al.*, *J. Phys. Chem. B*, **2004**, 108 (*45*), 17393-17397.

[351] Xu, Y. *et al.*, *Am. Mineral.*, **2000**, 85 (*3-4*), 543-556.
[352] Johnson, B. *et al.*, *J. Appl. Phys.*, **2009**, 106 (*7*), 073712.
[353] Jasieniak, J. *et al.*, *ACS Nano*, **2011**, 5 (*7*), 5888-5902.
[354] Chung, H. *et al.*, *J. Phys. Chem. C*, **2015**, 119 (*13*), 7517-7524.
[355] Jha, P. P. *et al.*, *J. Phys. Chem. C*, **2010**, 114 (*49*), 21138-21141.
[356] Jin, S. *et al.*, *ACS Nano*, **2010**, 4 (*3*), 1545-1552.
[357] Dewald, J. F., *J. Phys. Chem. Solids*, **1960**, 14 155-161.
[358] Makarov, N. S. *et al.*, *J. Phys. Chem. Lett.*, **2014**, 5 (*1*), 111-118.
[359] Bozyigit, D. *et al.*, *Adv. Funct. Mater.*, **2013**, 23 (*24*), 3024-3029.
[360] Rowland, C. E. *et al.*, *Opt. Mater. Express*, **2017**, 7 (*6*), 1871-1881.